The characterisation of mullite-related phases by hydrothermal synthesis

Thesis

UNRESTRICTED

The Characterisation of Mullite-Related Phases by Hydrothermal Synthesis

Submitted for the degree of Doctor of Philosophy in the discipline of Chemistry

Submission Date: October 23 1995

Resubmission Date: January 2 1996

Mark William Booth MSc. BSc (Hons)

Date of submission: 23 October 1995
Date of award: 20 December 1995

Abstract

The aluminosilicate called mullite has been prepared by hydrothermal processing from aluminium- and silicon- acetates. The phase evolution of the products and the mechanism of formation of mullite from its precursors has been examined by x-ray powder diffraction, magic-angle spinning NMR spectroscopy, FTIR spectroscopy and electron microscopy. The product obtained from co-processing aluminium- and silicon- acetates was found to be a biphasic material with strong interfacial interactions between pseudoboehmite and amorphous silica-gel type phases. This interfacial interaction resulted in mullite being formed after calcination at 1250°C, which is a lower temperature than would normally be expected for the formation of mullite. Lattice parameter measurements of mullite calcined up to 1400°C suggested that a metastable state may be formed at the lower temperature. The effect of adding acid to the reagent mixture was examined and found to have no effect on the chemistry of the phase evolution of the products.

The synthesis of iron-doped mullite has also been examined by x-ray powder diffraction, Mössbauer spectroscopy, EXAFS and electron microscopy. The iron-containing phases in dried intermediate materials exhibited superparamagnetism. Upon calcination iron-doped mullite formed at 1150°C with an iron content up to 14 mol%. EXAFS showed the iron to occupy octahedral sites in the mullite structure.

The synthesis of magnesium-aluminium spinel has been examined using a similar methodology. The interfacial interaction between the initial precursors was found to be stronger than that observed in the aluminosilicate system. This increase in interfacial interaction is associated with the lower temperature required to form spinel (400°C).

Table of Contents

Chapter 1
Introduction

1.1. AIMS

The aims of the work presented in this thesis are to:

1) Synthesise mullite and metal-doped mullite by calcination of sols formed by a hydrothermal processing technique

2) Investigate the phase evolution of mullite and metal-doped mullite prepared by this method.

1.2. BACKGROUND AND LITERATURE SURVEY

1.2.1. Mullite - composition and structure

Mullite is an aluminosilicate and is so named because it was first discovered naturally on the Isle of Mull.[1] It was first synthesised in 1865 by passing SiF_4 over a mixture of alumina and silica at a "bright red heat".[2]

a) The composition of mullite.

The composition of mullite varies according to the value of x in the formulation.

$$Al_2^{oct}(Al_{2+2x}^{tet}Si_{2-2x}^{tet})O_{10-x} \qquad (1)$$

(where x denotes the number of oxygen-atom vacancies per average unit cell)

When x is low (<0.04), a silica rich composition exists and mullite adopts the sillimanite structure (Figure 1(a)), which is discussed later. The other extremity of the composition range where x is high (ca. 1) is ι-alumina, details of which are sparse.[3]

These compositional variations are made possible by oxygen loss, which occurs throughout the structure as tetravalent silicon is replaced by trivalent aluminium. The holes which are formed were initially thought to be randomly distributed,[4] but it has since been demonstrated that certain situations are avoided, i.e. 2 holes adjacent to one another.[5] Due to these oxygen losses there is no one crystal system that can describe mullite. It is hence termed incommensurate.

The value of x which determines the mean Al : Si ratio is x=0.4 and $2Al_2O_3.SiO_2$ is a representation of this form of mullite. It is often referred to as 2/1 mullite and it has an aluminium content of 66 mol%. Naturally occurring mullite always forms 3/2 mullite, described by the representation $3Al_2O_3.2SiO_2$ It has an aluminium content of 60 mol% and x=0.25. It is possible to synthesise 2/1 mullite but further heating often results in its transformation to the 3/2 form.[6]

b) The structure of mullite.

The compositional limits of mullite result in its structure having similarities with those of sillimanite at one extreme and ι-alumina at the other.

Sillimanite (Figure 1(a)) is characterised by having columns of edge-sharing AlO_6 octahedra which form chains running parallel to the c-axis. These octahedral columns are cross linked by tetrahedrally co-ordinated silicon-and-aluminium. These tetrahedra form double chains and run parallel to the c-axis. Figure 1(a) shows a single layer of these vertex-sharing tetrahedra.

The similarity between mullite and sillimanite can be seen in Figure 1 and mullite can also be described in terms of chains of edge-sharing AlO_6 octahedra. It has been observed that the oxygen vacancies arising from replacement of Al^{3+} by Si^{4+} only occur at O_c sites (Figure 1(a)). The vacation of one of these sites results in the Al atom having only 3-fold co-ordination and hence the structure rearranges to give the Al atom 4-fold co-ordination in a new T^* site (Figure 1(b)). This in turn leads to the displacement of the adjacent oxygen atoms forming O_c^* sites. The order of magnitude of the O_c displacement is ca. 0.1 Angstroms.[7]

There has been some discussion over the occupancy of the T^* sites. Initially Al was assumed to occupy these sites, but more recent models have been less definitive. One model looking at the average structure of mullite (x=0.4) proposed by Angel and Prewitt showed that is was possible that a small amount of silicon may be present on T^* sites.

The structural association of mullite with ι-alumina has stemmed from reports of silica-free compounds with mullite-type structures made by Foster.[8]

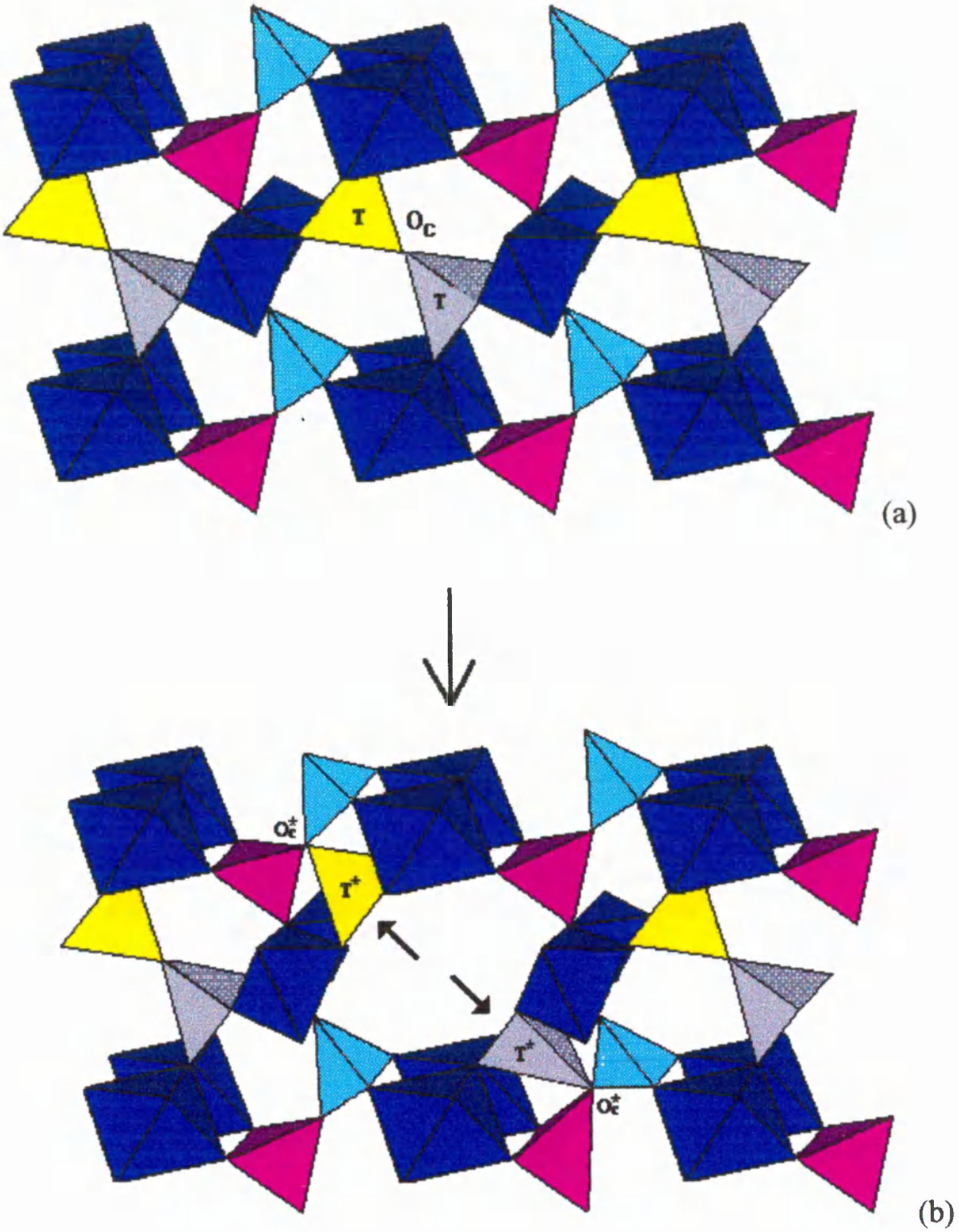

Fig. 1 The transformation undergone by sillimanite (a) to mullite (b)

It has been postulated that since a tetrahedral site, containing only aluminium, is created every time an oxygen vacancy occurs, a solid solution should exist from 3/2 mullite to ι-alumina. Mullite has been formed with aluminium contents as high as 83 mol% and studies of the lattice parameters have shown that as the aluminium content increases, the *a* lattice parameter increases while the *b* lattice parameter decreases. The lattice parameters have been shown to change from a situation where b > a to a > b at about 79 mol%, x=0.67.[9] The x-ray powder diffraction pattern recorded from mullite with these unit cell parameters exhibits intensity inversions between certain neighbouring peaks, namely the 120/120 230/320, 240/420 and 041/401. This phase however is thermally unstable and heating above 1050^{0}C shows a gradual change in lattice parameters back to those of conventional mullite. The full solid solution range has never been observed. A structural comparison of mullite to ι-alumina is difficult as the structure of the latter has not been satisfactorily resolved, as it is metastable and readily converts to α–alumina.

1.2.2. Properties and applications of mullite

Mullite has never been considered for high strength applications at room temperature because its low fracture toughness limits its strength to 200-500 MPa. However, mullite can retain its strength at temperatures up to 1500^{0}C.[10] This strength retention is dependent on the purity of the mullite phase and the absence of any glassy phase. Hence, the method of preparation is very important.

Mullite has also been shown to have very good creep resistance. The first definitive study took mullite formed at 1500^{0}C and showed that there was no plastic deformation at stress levels up to 900 MPa.[11] If, however mullite does contain an amorphous boundary, the creep resistance has been observed to decrease by two orders of magnitude.[12] Pure mullite also exhibits good thermal shock properties and hence is suitable for kiln furniture and refractories.

The electronic packaging industry is one of the key technologies that will make advances in the computer industry possible. Mullite is now being used in the electronic packaging industry as it has significantly better properties than alumina which has been widely used for many years. Packaging involves the interconnecting, powering, protecting and cooling

of semiconductor circuits. The efficiency of the transmission of signal through these packages is measured by the transmission signal delay time, T_d:

$$T_d = \sqrt{\frac{E_r}{c}} \qquad (2)$$

where E_r is the dielectric constant of the material and c is the speed of light.[13] The low dielectric constant of mullite (ε=6.7) results in about a 17% lower signal transmission delay time than alumina (ε=9.8).

Another important property of a substrate in this field is the ability to solder the substrate to the chip. The fatigue life of the solder is dependent on the difference between the thermal coefficient of the ceramic and the thermal coefficient of silicon. The smaller the difference the better. Mullite substrates show a smaller difference than alumina, and mullite-based glass-ceramics show an even further improvement, and hence have emerged as possible choices for high performance packaging applications.[14]

Mullite also has potential for use as a mid-range infrared window. Investigations into the ultraviolet and near infrared regions have shown mullite to have too low a transmittance even after hot isotactic pressing.[15] (Hot isotactic pressing is a technique whereby a powder sample is compressed simultaneously in three directions at raised temperature. This results in regular particle size and good densification, but is very expensive.) The potential of mullite in this area is in chemically harsh, hot, or mechanically stressful environments where it competes well with other materials such as spinel or sapphire. Mullite of high purity and high density is required for this work and the methods of preparation have tended towards liquid phase reactions.[16,17] The subsequent transmittance of mullite in the infrared region is about 98% at 4000 cm^{-1} and falls gradually down to 2000 cm^{-1}. Beyond this value the transmittance is again too low to be suitable for industrial application. There is however a peak observed by some workers at 2200 cm^{-1} which is undesirable.[18] It has been suggested that the peak may be due to nanometre-sized amorphous inclusions. The size of the peak may be used as a method of quality control.

In conclusion, mullite is emerging as a good candidate for many industrial applications, not because it has the best qualities of any known material, but because it combines its good electronic and optical properties with its ability to be used in stressful environments.

1.2.3. Preparation of mullite

a) Overview

The potential importance of mullite for commercial applications has caused great interest and hence there have been many attempts by many different routes to prepare mullite. The conventional method of synthesising mullite was to take stoichiometric quantities of aluminium oxide and silicon oxide, grind them together, and fire the mixture at temperatures >1600^{0}C.

$$2SiO_2 + 3Al_2O_3 \xrightarrow{\Delta} 3Al_2O_3.2SiO_2 \qquad (3)$$

There are certain disadvantages with this route. Firstly, the temperature of formation is excessively high for an industrial process. Secondly, it leads to an inhomogeneity of crystallite size, as the particles have not been intimately mixed, and hence the final product does not show good performance. Thirdly, incomplete reaction is more likely to occur, hence long sintering times are required.

The firing temperature can be lowered to 1470^{0}C by using 0.3-0.5 μm α–Al_2O_3 and <2 μm quartz particles.[19]

There are three distinct new approaches which have been adopted to try and overcome these problems. Firstly thermally transforming a mineral, secondly, using one processing technique (usually sol-gel synthesis) and altering the chemical environment of the metal in the starting materials; the predominant types of starting materials being metal acetates, metal alkoxides, metal polymerics and metal salts. The final approach is to vary the processing techniques employed. The main techniques are; hydrothermal synthesis, co-precipitation, spray drying and chemical vapour deposition.

These three approaches will now be examined in turn.

b) Transformation of a mineral

There are several minerals which, on calcination, form mullite. These are kaolinite, kyanite, sillimanite, andalusite, staurolite and topaz. These transformations were presumably popular because of the lack of processing required and the fact that the temperature of formation of mullite was lower than in the conventional method. The mineral that transforms to mullite at the lowest temperature is kaolinite.

Transformation of kaolinite ($SiO_2 \cdot Al_2O_3 \cdot 2H_2O$)

In 1959 the following reaction sequence was proposed by Brindley and Nakahira.[20]

$$2SiO_2.Al_2O_3.2H_2O \rightarrow 2SiO_2.Al_2O_3 \rightarrow \tfrac{1}{2}(3SiO_2.2Al_2O_3)+\tfrac{1}{2}SiO_2$$

$$\rightarrow SiO_2.Al_2O_3+SiO_2 \rightarrow \tfrac{1}{3}(2SiO_2.3Al_2O_3)+\tfrac{1}{3}SiO_2 \qquad (4)$$

The kaolinite loses water to become metakaolinite then transforms to become a spinel-type phase. It then forms 'transitional mullite' which loses silica to become mullite.

More recently, density studies, together with infrared spectroscopy and MASNMR investigations have pointed to a different reaction sequence after the formation of metakaolinite ($2SiO_2Al_2O_3$). It is now believed to proceed via $\gamma - Al_2O_3$ and go on to form amorphous alumina, amorphous silica and mullite.[21] A recent review has commented that using this method, single phase mullite has not been observed by x-ray powder diffraction.[22]

Transformation of staurolite ($Fe_4^{2+}Al_{18}Si_8O_{46}(OH)_2$)

Staurolite is an iron-containing mineral and can be though of as being made up of alternating layers of kyanite (Al_2SiO_5) and ($AlOOH \cdot 2FeO$) parallel to the (010) plane. On dry heating the following reaction occurs:[23]

$$Fe_4^{2+}Al_{18}Si_8O_{46}(OH)_2 \rightarrow 3(3Al_2O_3 \cdot 2SiO_2)+4FeO+2SiO_2+H_2O\uparrow \qquad (5)$$

The formation of mullite is accompanied by the presence of by-products which highlights a major problem with this synthetic route.

c) Sol-gel synthesis and the effect of varying the nature of the starting materials

This synthetic route is so named because the sequence of events is:

$$Solution \longrightarrow Sol \longrightarrow Gel$$

where a sol is defined as a suspension of a colloid, and a gel is defined as a material formed by the coagulation of a colloidal liquid.[24] A sol is significantly different from a precipitate because the colloidal particles are so small that the strongest forces acting upon them are Brownian motion and surface charges. Hence, sols do not separate out under the influence of gravity. The gel is formed by removing water from the sol and its consistency can range from jelly-like to solid.

The advantages of using this preparative route are:

- Controlled stoichiometry of reactants and products.
- High purity of product
- High homogeneity of product
- Low temperature preparations
- Direct moulding of product
- Non-elaborate equipment

This route is as yet the most industrially attractive as in 1990 it was the only method used for making mullite on a scale exceeding 500 kg/month.[25]

There are several different approaches which have been used. Some form sols which are then transformed into gels, while others form gels using hydrolysis of alkoxides. The most important methods are outlined in the following sections.

Mixing of two sols

When mixing two sols the pH has been shown to be an important factor. This is because the silica sol stability is dependent upon pH, whereas the alumina sol shows little change in stability from pH 2 to pH 11. Beyond this pH both sols dissolve and hence no longer exist as sols at all. The silica sol has two areas of stability; the first is around pH 2 and the second is between pH 9 and pH 10. One worker mixed silica and alumina sols at an acidic

pH and found that mullite formation began after calcining the gel formed at 1275°C and densification continued up to 1550°C.[26] This route is an improvement over the solid state route in that although it is still dependent upon diffusion, the particle size is smaller, and the mixing of the two components is better.

Mixing a silica sol with an aluminium salt

This method is believed to be a further improvement over mixing two sols in that it is believed that the salt either coats or at least precipitates on the surface of the sol particles leading to a closer interaction than observed in the previous method.

Two workers using similar methods have built up a useful framework for understanding the processes involved.[27,28] Aluminium sulphate is dissolved in distilled water and into this solution is added a silica sol, (prepared from fumed silica in distilled water) while being vigorously mixed. The mixture is then dried above 100°C for several days. It is then heated at about 1000°C in order to break down the sulphate. X-ray powder diffraction shows a spinel phase which has a surprisingly high surface area of 188 m^2/g. The compound is then milled in heptane using alumina balls. Calcination at 1200°C yields mullite. Full theoretical density is reached only by compacting the non-mullite powder and firing at temperatures >1500°C. This is due to the fact that the formation of mullite hinders subsequent densification. Hence to achieve dense mullite at low temperatures densification has to occur before the formation of mullite.

Another worker used the same starting materials but worked at the alkaline stability region of a silica sol. Having mixed the two reagents together liquid nitrogen was sprayed into the mixture, which was then freeze dried.[29] This procedure gave an amorphous free flowing powder which did not form mullite until calcined at 1400°C.

Mixing an aluminium sol with a silica suspension

This method is believed to lead to increased densification by coating an alumina particle with silica. It is however, somewhat harder to achieve. One attempt suspended alumina particles in ethanol and mixed them with an ethanol solution containing tetraethoxysilane (TEOS). Addition of ammonia hydrolysed this solution and caused the silica to precipitate

on the surface of the alumina particles.[30] Sintered compacts achieved almost maximum density at 1300°C, but mullite was not formed until 1500°C and was not single phasic even after calcination at 1600°C.

Mixtures of alkoxides

When alkoxides are used in mullite synthesis, the alkoxide needs to be hydrolysed by the addition of water, or water together with acid or base, which acts as a catalyst. The hydrolysis rate of the silicon alkoxide is much slower than that of the aluminium alkoxide, and hence this route does not necessarily produce a double alkoxide. Hence addition of a catalyst, or pre-treatment of the silicon alkoxide before mixing, has been performed to try and equalise this difference.

One set of workers mixed solutions of TEOS ($Si(OC_2H_5)_4$) and $Al(O^iPr)_3$ and hydrolysed them by the slow addition of water containing butanol. This lead to mullite formation above 1150°C, and the phase evolution went through a spinel phase.[31]

Another set of workers compared the use of TMOS ($Si(OCH_3)_4$) with TEOS as the silicon source using HNO_3 as an acidic catalyst. Both routes showed a biphasic compound containing poorly crystalline mullite phase after calcination at 950°C. Single phasic mullite was not observed until calcination at 1200°C.[32]

One other attempt pre-treated the silicon alkoxide dissolved in ethanol, water and HCl by refluxing at 70°C for 50 h, before mixing with the aluminium alkoxide. This again formed a spinel phase and formed mullite at temperatures exceeding 1100°C.

Mixture of an aluminium salt and a silicon alkoxide

A model has been proposed for two types of particle formation.[32] The first type is represented as a coated particle and is formed using a basic catalyst, an excess of H_2O, long ageing time of solution, low solubility of the aluminium salt and rapid evaporation of the solvent.

The second type is represented as a homogeneous particle of mixed molecularity and is formed in an acidic pH using an adequate amount of water for hydrolysis, needs a short ageing time, high solubility of the aluminium salt and slow evaporation of the solvent.

The first type forms a spinel phase at around 1000°C which then goes on to form mullite, while the second type has been reported to form mullite directly from the amorphous state at 1000°C.

d) Other methods of synthesis

Hydrothermal processing

A general definition of hydrothermal synthesis is "the chemical interaction between hydrolysable precursor materials and water, either directly or catalytically, under hyperatmospheric pressure at temperatures above the boiling point of water, to produce, in general, oxides."[33]

However, despite this minor limitation on the type of material which may be produced, the benefits which this method of synthesis have shown in some systems make it highly suitable for current synthesis procedures and its potential is such that it is likely to be used increasingly in the synthesis of advanced ceramics. The technicalities and instrumentation of this technique will be discussed in the next chapter.

In particular this method allows control over the stoichiometry of the system as any volatile components are likely to condense inside the autoclave, maintaining the initial stoichiometry of the mixture. The relatively high processing temperature of the reaction means that a wider choice of starting materials is available as quite stable precursors can be broken down. Once the precursors have broken down a higher rate of reaction, again caused by the high temperature of the system, can often result.

The starting materials used in this work are acetates because they are readily available and decompose to give products which do not affect the reaction adversely. Basic aluminium di-acetate $Al(OH)(CH_3COO)_2$, which is complex in that it does form a triacetate but it is difficult to prepare. When the tri-acetate is left in air it decomposes to give the bi-acetate initially and eventually the mono-acetate.[34] The bi-acetate has the form of a white solid which is insoluble in cold water and has a decomposition temperature of ca. 250°C at atmospheric pressure which is lowered by heating under hydrothermal conditions. Silicon tetra-acetate $Si(CH_3COO)_4$ has the form of colourless hygroscopic crystals which decompose in cold water. Silicon tetra-acetate also sublimes at 110°C and decomposes at

ca. 160°C upon heating. Magnesium acetate tetrahydrate $Mg(CH_3COO)_2 \cdot 4H_2O$ is colourless and deliquescent and is quite soluble in cold water. Iron(II) acetate tetrahydrate $Fe(CH_3COO)_2 \cdot 4H_2O$ has the form of light green needles which are very soluble in water. Iron(III) basic acetate, $Fe(OH)(CH_3COO)_2$ has the form of a brown/red powder and is insoluble in cold water but soluble in acid. From the above descriptions it is clear that acetates do not present many of the of the problems described with other starting materials in other methods of syntheses. However they are only suited to hydrothermal synthesis because of the raised temperatures and pressures used in this technique. This is one of several advantages which hydrothermal synthesis has over a standard sol-gel route; others will be looked at in the next chapter.

Co-precipitation

Co-precipitation involves adding a precipitant, which is usually ammonia solution, to a solution containing both silicon and aluminium, which then precipitate out. However, the yield of this precipitation is often rather low. Workers using two salts have formed the homogeneous particle of mixed molecularity described earlier (page 11), but problems have been encountered because in one case the stability of the salts, especially silicon chloride leads to uncertainty of the chemical composition of the precipitate formed. Other silicon sources such as sodium silicate have been tried but, despite thorough washing, the precipitates formed by this route often contain considerable amounts of the alkali metal salt.

Spray pyrolysis

This technique uses droplets formed from a solution which is sprayed onto a furnace heated at temperatures between 350°C and 650°C. The various reactions that would normally occur over some period of time by calcining in a furnace, such as thermal decomposition and evaporation of solvents all occur instantaneously.[35] The particle size distribution appears to range from the micrometer to the sub micrometer scale, which is not ideal. The reagents used tend to be a silicon alkoxide and an aluminium salt. This again involves the problems of getting the correct ratio of water to alkoxide for hydrolysis

and often considerable preparation times pre-treating the silicon alkoxide. The choice of aluminium salt, and the choice of either an acidic or basic catalyst is also important.

Chemical vapour deposition

This process is unique in that it produces mullite from the gaseous phase rather than the liquid or solid phase. Chlorides were evaporated separately and carried to the mixing zone using a nitrogen gas flow. In the mixing zone they were rapidly heated by a hydrogen/oxygen flame at an estimated temperature of 1900°C. The exit temperature was 900°C and the estimated reaction time was 65 ms. The particle size was 40-70 nm and phase analysis showed the presence of spinel phase and small amounts of mullite. Subsequent calcination at 1000°C caused extensive mullite formation, but complete mullite formation was not observed until calcination at 1500°C.

1.2.4. Spinel - Composition and Structure

There are well over one hundred compounds with the general spinel structure, AB_2O_4, of which $MgAl_2O_4$ is the parent. $MgAl_2O_4$ has a crystal structure that shows similarities and differences to those of both MgO and $\alpha-Al_2O_3$; MgO and spinel have a cubic close packed array of oxide ions, in contrast to $\alpha-Al_2O_3$ which has a distorted hexagonal close packed array of oxide ions. Conversely the Al^{3+} ions occupy octahedral sites in both $\alpha-Al_2O_3$ and spinel, while the Mg^{2+} ions are octahedral in MgO but tetrahedral in $MgAl_2O_4$.

1.2.5. Spinel - Preparative methods

The main preparative methods used for the preparation of spinel have been assessed[36] and relates the procedures to their industrial application. A more detailed study, which concentrates largely on the solid-state reaction is given by West.[37]

a) Solid state reaction

The conventional method of synthesising spinel has involved the solid state reaction according to Equation 6.

$$MgO + Al_2O_3 \rightarrow MgAl_2O_4 \qquad (6)$$

The reaction occurs slowly at temperatures above ca. 1200°C and in order for the reaction to proceed to completion, calcination at 1500°C for extended periods of time is required. The resulting powder has large particle sizes, exhibits poor homogeneity and is quite impure. It is one of the two main commercial processes for manufacturing spinel.

b) Co-precipitation

Chemical precipitation from hydroxides dissolved in acidic aqueous solution as well as nitrates, chlorides and oxalates have been used to prepare magnesium-aluminium coprecipitates which form spinel of high purity and small particle size after calcination at ca. 600°C. There are problems with this method however as parameters such as pH, mixing rates, temperature and concentration all have to be controlled to produce satisfactory results. This method also tends to form agglomerates.

c) Sol-gel

This method involves the hydrolysis of alkoxides, which in the case of magnesium-aluminium spinel react to form a double alkoxide. The formation of this double alkoxide is advantageous as it retains the exact stoichiometry between the metals. If the double alkoxide is formed by reaction of magnesium methoxide and aluminium *sec* butoxide in alcohol, then evaporation in the presence of water and heating at 620°C reportedly results in spinel formation.[38] In industry this process is still in the research and development stage. The costs are moderate to high, but it gives very good homogeneity and excellent purity. The temperature of calcination has also been reduced considerably compared to conventional methods. The main disadvantage apart from the cost is that agglomeration tends to occur.

d) Hydrothermal synthesis

The advantages of this technique are discussed Section 1.2.3.(d) and Chapter 2 Section 2.1.2. In the industrial formation of spinels this method is only at the demonstration stage although it is claimed that at temperatures up to 374°C and pressures up to 15 MPa spinel can be formed directly with no subsequent calcination stage.[37] The conditions under which spinel can be formed under autogenous pressure at 220°C is discussed in Chapter 6. Any

development in this area could help to bring down the industrial cost, quoted as moderate,[36] even at elevated pressures.

e) Other methods

Freeze drying is another method that has been used to prepare spinel. This process consists of two steps. The first is to spray fine droplets of solution into liquid nitrogen and secondly to sublime the solvent in the absence of liquid phase.[39] The resulting powder is extremely pure, has very small particle size and has high homogeneity. The process however is expensive and may not be suitable for large scale production. It is at present at the demonstration stage in industry.

1.3. REFERENCES

[1] N. L. Bowen, J. W. Greig & E. G. Zeiss *Journal of the Washington Academy of Sciences,* 1924 **14** 183

[2] H. S. Deville & H. Caron *Ann. Chem. Phys.* 1865 **114**

[3] W. E. Cameron *Am. Mineral.* 1977 **62** 747

[4] T. Epicier, M. A. O'Keefe & G. Thomas *Acta. Cryst.* 1990 A**46** 948

[5] B. D. Butler, T. R. Welberry & R. L. Withers *Phys. Chem. Minerals* 1993 **20** 323

[6] R. J. Angel & C. T Prewitt *Am. Mineral* 1986. **71** 1476

[7] R. J. Angel, R. K. McMullan & C. T. Prewitt *Am. Mineral.* 1991 **76** 332

[8] P. A. Foster *J. Electrochem. Soc.* 1959 **106** 971

[9] H. Schneider, R. X. Fischer and D. Voll *J. Am. Ceram. Soc* 1993 **76** 1879

[10] T. Mah & K. S. Mazdiyasni *J. Am. Ceram. Soc.* 1983 **66** 699

[11] P. C. Dokko, J. A. Pask & K. S. Mazdiyasni *J. Am. Ceram. Soc.* 1977 **60** 150

[12] R. D. Nixon, S. Chevacharoenkul, R. F. Davis & T. N. Tiegs *Ceramic Transactions* 1990 **6** 579

[13] E. A. Giess, J. M. Roldan, P. J. Bailey & E. Goo *Ceramic Transactions* 1990 **15** 167

[14] R. R. Tummala *J. Am. Ceram. Soc.* 1991 **74**895

[15] H. Schneider, M. Schmücker, K. Ikeda and W. A. Kaysser *J. Am. Ceram. Soc.* 1993 **76** 2912

[16] S. Prochazka & F. J. Klug *J. Am. Ceram. Soc.* 1983 **66** 874

[17] N. Shinohara, D. M. Dabbs & I. A. Aksay *Infrared Opt. Transm. Mater. Proc.* 1986 **683** 19

[18] I. A. Aksay, D. M. Dabbs & M. Sarikaya *J. Am. Ceram. Soc.* 1991 **74** 2343

[19] K. Hamano, T. Sato, & Z. Nakagawa *Yogyo Kyokaishi* 1986 **94** 818

[20] G. W. Brindley & M. Nakahira *J. Am. Ceram. Soc.* 1959 **42** 311

[21] I. W. M. Brown, K. J. D. MacKenzie, M. E. Bowden & R. H. Meinhold *J. Am. Ceram. Soc.* 1985 **68** 298

[22] J. A. Pask & A. P. Tomsia *J. Am. Ceram. Soc.* 1991 **74** 2367

[23] J. Ganguly *J. Petrol.* 1972 **13** 355

[24] The Shorter Oxford English Dictionary 3rd Ed 1990 Oxford University Press

[25] S. Somiya and Y. Hirata *Ceram. Bull.* 1991 **701624**

[26] F. Orgaz *Proc. Third Euro-Ceramics Conf.* Ed. P. Duran and J. F. Fernandez Published by Faenza Editrice Iberica S. L., Spain 1993 **3** 377

[27] F. Kara and J. A. Little *J. Mat. Sci.* 1993 **28** 1323

[28] M. Mizuno, M. Schiraishi and H. Saito *Ceramic Transactions* 1990 **6** 413

[29] T. A. Wheat, E. M. H. Sallam and A. C. D Chaklader *Ceram. Int.* 1979 **5** 42

[30] M. D. Sacks, N. Bozkurt and G. W. Schieffle *J. Am. Ceram. Soc.* 1991 **74** 2428

[31] S. Prochazka and F. J. Klug *J. Am. Ceram. Soc.* 1983 **66** 874

[32] U. Selvaraj, S. Komarnesi and R. Roy *J. Solid State Chem.* 1993 **106** 73

[33] C. B. Ponton *Proc. Third Euro-Ceramics Conf.* Ed. P. Duran and J. F. Fernandez Published by Faenza Editrice Iberica S. L., Spain 1993 **1** 189

[34] V.N. Maksimov, K.N.Semenenko, T.N. Naumova and A.V. Novoselova *Russ. J. Inorg. Chem.* 1960 **5** 267

[35] J. G. M. deLau *Am. Ceram. Soc. Bull.* 1970 **49** 572

[36] P. Cousin and R. A. Ross 1990 *Mat. Sci. Eng.* **A130** 119

[37] A. R. West 1984 *Solid State Chemistry and its Applications* Wiley Chichester

[38] H. Dishlich 1971 *Angew. Chem. Int. Edn.* **10** 367

[39] D. M. Roy and S. O. Oyefesobi *J. Am. Ceram. Soc. Discuss Notes* 1977 **60** 178

Chapter 2
Theory of Techniques

2.1. HYDROTHERMAL PROCESSING

Hydrothermal synthesis has been described on page 12 as "the chemical interaction between hydrolysable precursor materials and water, either directly or catalytically, under hyperatmospheric pressure at temperatures above the boiling point of water to produce, in general, oxides."

In order to process chemicals at hyperatmospheric pressure at temperatures above the boiling point of water special apparatus is needed.

2.1.1. Autoclave design and development

Some early attempts to hydrothermally process reagents showed a significant degree of inventiveness. De Sénarmont in 1851 placed the reagents in sealed glass ampoules, which were half filled with water, in a welded gun barrel, which had been partially filled with water, and heated the system to a dull red glow.[1] Significant advances were introduced when Moray designed an autoclave in 1914. It consisted of a closed system made of steel which was then placed into an oven and heated at 400°C. The autoclave could withstand pressures up to 400 bar.[2] The autoclave was lined with a noble metal so that reactants could be placed in the reaction chamber directly, or be placed into a glass ampoule which was sealed and then placed into the autoclave. A further improvement was introduced by Tuttle in 1949 with the cold-seal bomb.[3,4] This autoclave consisted of a metal chamber which was sealed by a threaded nut and cone. The seal was located outside the furnace which enabled much higher temperatures and pressures to be obtained.

For standard work the arrangements of Moray and Tuttle remain satisfactory. Other developments in autoclave design have allowed more sophisticated syntheses to be performed. The acquisition of higher temperatures requires the outside of an autoclave based on the Tuttle design to be cooled and a pressuriser used to obtain the desired pressure for the reaction. This arrangement can be used up to 1400°C and 10 kbar. Hydrothermal syntheses under conditions of up to 2000°C and 150 kbar using a graphite heater can be performed using the Belt Technique[5] which can withstand such extreme

processing conditions by having a small reaction chamber surrounded by anvils which are tipped with tungsten carbide and supported by hard steel rings.

The choice of materials with which to line the autoclave is an important factor. The steel walls of the autoclave are usually unsuitable because of the corrosive nature of many solutions and the danger of contamination of the reactants. The range of suitable lining materials is limited because relatively little is known about the corrosion behaviour of many materials under hydrothermal conditions. Hence graphite, titanium, glass, quartz glass or borosilicate glass is often used. Quartz glass in particular can be used up to 500°C as a liner or 1000°C as an ampoule. These materials are resistant to corrosion from most acids and bases as well as toxic materials such as antimony, arsenic and tellurium. A specially treated potentially pore free Teflon, made by an isotactical pressing process, has been used, both as a lining material, and as an autoclave seal. The Teflon is of low porosity, has equal heat expansion properties and resists corrosion even by hydrogen fluoride. The pressure-temperature range over which it can be used is somewhat limited with maxima of 275°C and 350 bar.

The autoclave used in the work reported here is shown in Figure 2. The reaction chamber is made from a special CrNiMostainless steel and is placed inside a heating mantle (not shown). The lining used is a Teflon beaker and the reaction mixture is stirred using a magnetic stirrer. The NiCr / Ni thermocouple passes through the middle of the hollow stirrer and has a detachable Teflon cover. This enables the temperature of the reaction to be monitored very accurately. The autoclave has two valves, one of which is a gas feed, allowing reactions to be performed under inert atmospheres, and the other enables sampling of the reaction mixture during the course of the reaction. The seal is also made from Teflon and the top is secured to the base using two large semicircular metal rings, which are held together using two long-threaded steel bolts. The upper limit of the heating mantle is 300°C which makes it ideal for use with a Teflon liner which has an upper temperature limit of 250°C.

Water is the usual medium for hydrothermal synthesis because its properties as a good solvent at room temperature are enhanced at elevated temperatures.

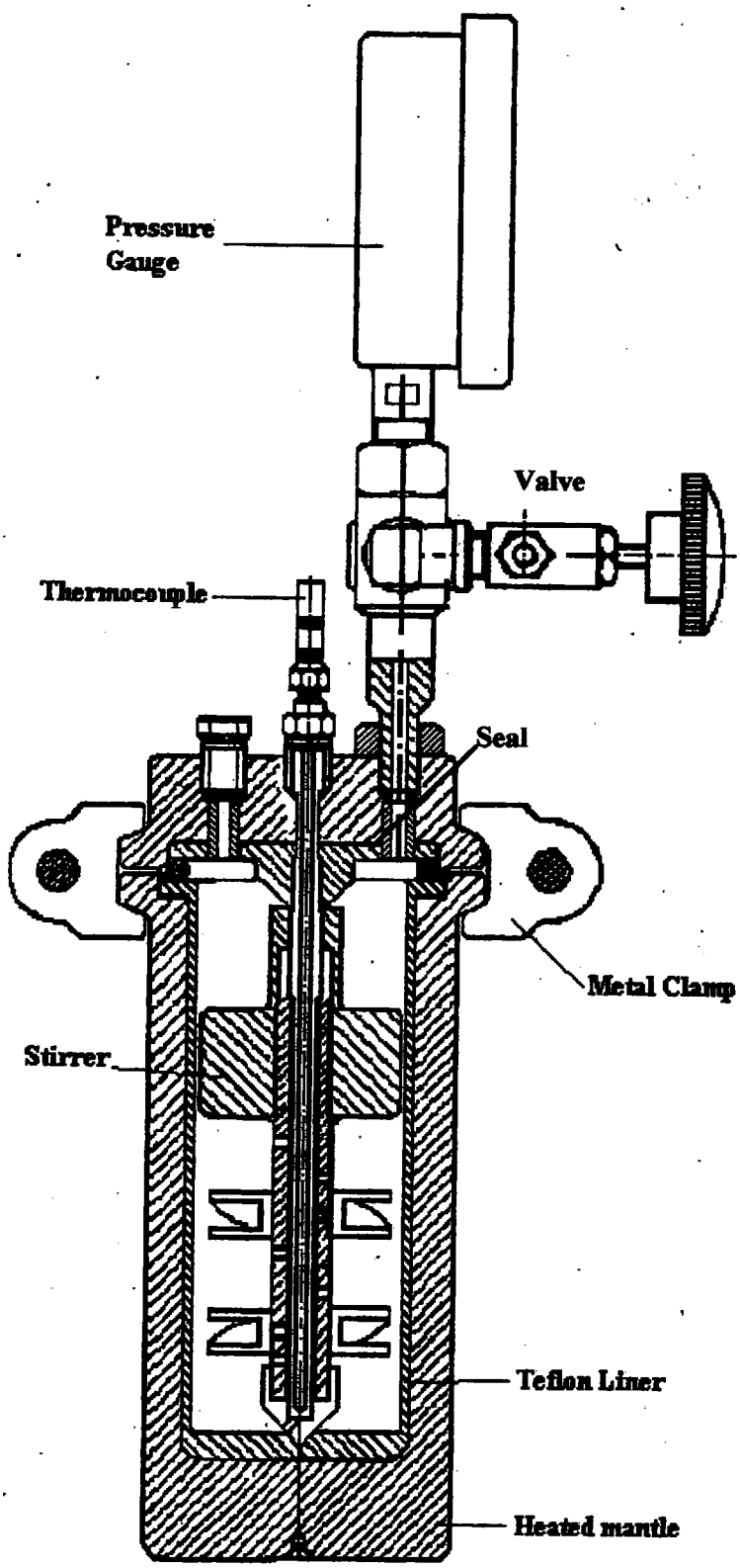

Figure 2. A Schematic diagram of an autoclave

One advantage of processing at high temperatures is that the viscosity of water decreases with increasing temperature and is 10% of its standard value at 500°C and 100 bar. This enhances the mobility of molecules and ions. Another advantage is that at high temperatures and pressures water dissociates to a greater extent assisting in the break down of more stable starting materials, such as acetates.

Other solvents have been used in cases where the solubility of one of the reactants is too low or the product reacts with water. Formic acid can be used to create a reducing atmosphere when it decomposes to CO_2 and H_2. Ammonia which can be considered to be a polar solvent under hydrothermal conditions has also been used to synthesise such materials as water-free hydroxides and NaCl.[6]

2.1.2. Advantages of hydrothermal processing in synthesis

Two advantages of hydrothermal processing discussed in chapter 1 were:-

1) Careful control of the stoichiometry of the reaction mixture

2) The ability to break down more stable reagents, widening the choice of reagents

These factors have lead to hydrothermal synthesis being used to make materials with complex compositions. Another factor is controlled grain size. For example in the manufacture of multilayer capacitors, perovskite structures containing up to eight dopants and a grain size of ca. 1-4 μm have been prepared using hydrothermal synthesis. Other attempts to make these materials by co-precipitation techniques at 100°C failed to produce a solid solution. The product needed a subsequent calcination step, and milling to achieve a similar composition. Milling to a particle size of ca. 1-4 μm is technically difficult, and therefore expensive, and tends to contaminate the product.[7]

Hydrothermal synthesis often forms products directly without a subsequent calcination and milling stage being necessary. Where calcination is necessary, the materials form soft agglomerates that can be broken down by less extensive and less contaminating milling. The products also exhibit greater reactivity towards sintering and hence form the desired materials at lower temperatures. This has been shown in the production of the commercially important perovskite, lead zirconate titanate (PZT). Conventionally this

material is prepared by ball milling the component oxides together and then calcining. The resultant powder is then ball milled again to break up agglomerates, dried and calcined at between 1250°C and 1300°C. This process has the disadvantage that one of the component oxides, PbO, is quite volatile at these temperatures. Hence, the hydrothermal route lowers the production cost and increases the efficiency of production. Hydrothermal processing produces a solid solution of metal doped PZT, which when cold isotactically pressed into disks, exhibited a density of 55% of the theoretical density. Subsequent calcination at 950°C produced a density of 98% of the theoretical density. Hence the hydrothermal method produces the material, at the desired density, at a temperature 300°C lower than the conventional method.

Hydrothermal synthesis has also been used to make compounds containing transition metals in oxidation states which are difficult to obtain. An example is the industrially important ferromagnetic chromium(IV) oxide, used in magnetic tapes. Hexavalent chromium oxide is hydrothermally processed with an excess of trivalent chromium oxide at 350°C and 440 bar and forms the desired product in one step and in a very pure form, as the only by-product is oxygen, which acts to stabilise the chromium(IV) oxide under these conditions. Hydrothermal synthesis is also used in industry to grow crystals. When the solubility of a material in water is so low as to prevent its growth a good procedure is to raise the temperature. The pressures required to maintain solvent density (and hence efficacy) at elevated temperature are rather high. Hence mineralisers are also added to the growth solution to increase the solubility of the material at relatively modest pressure-temperature conditions. The usual configuration for crystal growth is a cylindrical high pressure autoclave. Solute is placed in the bottom of the autoclave which is then filled up to a predetermined level, with either water, or water plus mineraliser. Suitably oriented single crystal seeds are suspended in the upper half of the autoclave. The autoclave is then closed and placed in a furnace designed to heat the solute to a higher temperature than the seed crystals. The solvent evaporates and moves by convection into the area containing the seed crystals. This area is cooler, causing the evaporated solvent to become supersaturated and hence initiate growth. This method is particularly useful as it is particularly amenable to scale up for industrial processes and because of the high purity of the crystals produced.

The first serious application of the hydrothermal growth technique was for the growth of single-crystal quartz for oscillators.[8] The technique has also been used to grow industrially important materials such as corundum, the laser compound $Y_3Fe_5O_{12}$ and related garnets as well as being used as a crystallisation step in the formation of zeolites. Hydrothermal synthesis can also be used in the manufacture of artificial gems such as sapphire and emerald.

2.2. X-RAY POWDER DIFFRACTION

2.2.1. Overview

Powders have a distinct advantage in that they are much easier to produce than single crystals. The increasing computerisation of x-ray powder diffraction has reduced the time to examine samples and hence ensured the future of x-ray powder diffraction as a routine technique in the analysis of crystalline solid-state materials. The computerisation of subsidiary quantitative techniques such as mathematical peak fitting, indexing and Rietveld analysis, is starting to allow information to be obtainable from powder x-ray diffraction which was previously obtainable only from single crystal work.

There are many good accounts given of the theory of x-ray powder diffraction, in particular those of Klug and Alexander,[9] Azàroff,[10] and Cullity,[11] have been referred to. The fundamental features of the techniques are described in the following sections.

2.2.2. Theory of diffraction

The technique of x-ray diffraction was developed in 1912 by W. H. and W. L. Bragg. When a beam of x-rays is incident upon a crystal, which consists of sets of planes of atoms, the electric field of the x-rays and the individual electric fields of the atoms interact. The phase difference between x-rays being reflected from different planes of the crystal is affected by the distance between the planes, *d*, and also the angle of incidence between the x-rays and the plane of atoms, θ (Figure 3(a)). The wave normals connect points of identical phase for the incident and diffracted waves. For total constructive interference to occur, the distance $(A + B)$ must equal a whole number of wavelengths, i.e.

$n\lambda$. Using geometry: $\sin\theta = A/d = B/d$. Rearrangement of this gives $(A+B) = 2d\sin\theta$. Eliminating $(A+B)$ gives the Bragg Law:-

$$n\lambda = 2d\sin\theta \tag{6}$$

X-rays which are suitable for diffraction experiments have wavelengths between 0.5Å and 2.5Å. The x-rays used in the work reported here were copper Kα x-rays which have a wavelength of 1.54Å.

If the angle θ is changed slightly the cosine of the phase difference between reflected x-rays is very small, hence there is a considerable amount of constructive interference and so the peak will have some intensity at this different angle and appear broad. This is the case in a thin crystal or a small particle. In a thick crystal however, there will be many more planes at many different angles, and one will be at such an angle as to cause exact destructive interference with this small change in θ, causing zero intensity to be observed. Hence, for thick crystals or large crystalline particles, sharp peaks are observed. The Equation which represents the relationship between particle size and peak width is called the Scherrer Equation and it can be derived from the Bragg Law:-

$$\beta = \frac{K\lambda}{T\cos\theta} \tag{7}$$

where β is the width at half height of a reflection (in radians), K is a crystal shape constant approximately equal to unity and T is the thickness of the coherent diffracting domain along a direction, normal to the diffracting plane, *hkl* measured in Å.

In x-ray powder diffraction a finely powdered specimen is placed in a beam of monochromatic x-rays. The diffracted radiation from the specimen forms a series of cones of diffracted beams; each cone being generated from a set of differently spaced lattice planes (Figure 3(b)).

The term, structure factor, represented by the symbol, F, is used to portray the amplitude of scattering from a unit cell in the direction θ.

$$F_{hkl} = \sum_{1}^{N} f_n e^{2\pi i(hu+kv+lw)} \tag{8}$$

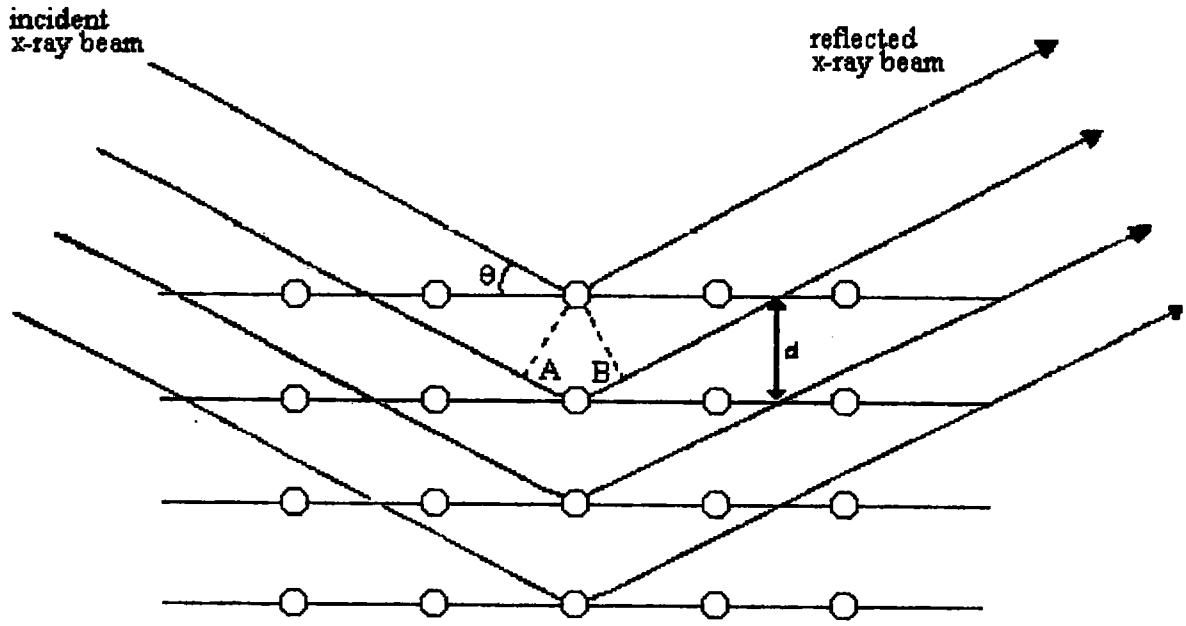

(a)

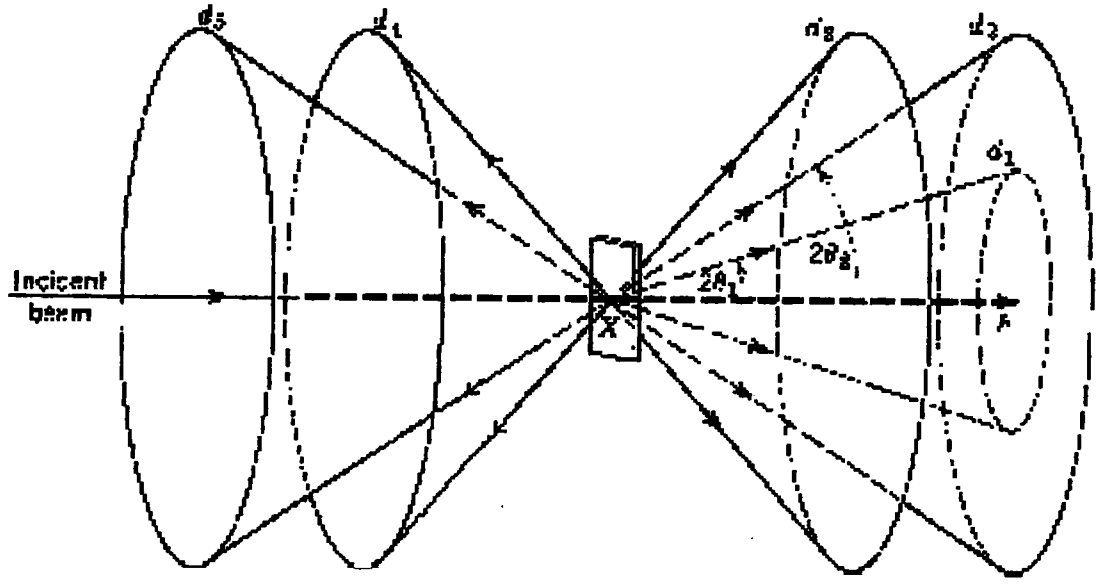

(b)

Figure 3. The Bragg law for parallel planes (a) and diffraction of x-rays from a powder sample (b)

where N is the number of atoms in the unit cell, u, v, and w, are the atomic co-ordinates of the atoms in the unit cell, i is the complex number, z-1, and f_n is the atomic structure of all atoms.

$$fn = \frac{\textit{amplitude of a wave scattered by an atom}}{\textit{amplitude of a wave scattered by one electron}} \quad (9)$$

F_{hkl} is generally a complex entity. The absolute value |F| can be expressed as:

$$|F| = \frac{\textit{amplitude of a wave scattered by all the atoms of a unit cell}}{\textit{amplitude of a wave scattered by one electron}} \quad (10)$$

The total intensity of the diffracted beam is dependent on $|F|^2$ as well as other factors and is given by I:

$$I = |F|^2 \, pL_p \left(\frac{1+\cos^2 2\theta}{\sin^2 \theta \cos\theta}\right) e^{-2m} \quad (11)$$

where p = multiplicity factor, e^{-2m} temperature factor and L_p = Lorentz-polarisation factor. The multiplicity factor arises because different sets of planes have the same interplanar spacing and therefore diffract at the same Bragg angle. The temperature factor is due to thermal vibrations of the atoms about their equilibrium positions in the space lattice, such that they can best be described as a triaxial ellipsoid. As the temperature increases, these vibrations increase, resulting in the position of the atom becoming less well defined and the reflecting planes necessary for diffraction are hence distorted. The Lorentz-polarisation factor accounts for the effect of the scattering power of the electron and the number of crystals correctly aligned for diffraction. It arises unless a crystal-monochromated primary beam is used.

2.2.3. Experimental methods

The x-rays are produced in a x-ray tube, normally by a tungsten filament, they are then accelerated through a voltage of ca. 40 KV and focused onto a metal target, (usually copper) which produces x-rays of a characteristic wavelength. The emitted x-rays pass through a beryllium window, towards the sample. Divergent x-rays are removed by a

collimating slit before hitting the sample and the reflected x-rays then pass through a collimating slit, an optional 12 μm thick Ni filter (to remove $K\beta$ radiation), a detector slit and finally a monochromator, before reaching the scintillation counter. The sample is held in a plastic container with a ribbed base to hinder ordering of particles (which could lead to a non-random distribution of particles) and then mounted in a spring loaded magnetic sample holder. The sample rotation speed and the range of 2θ to be examined are controlled by a computer.

The detector system rotates around the specimen with an angular velocity of twice that of the specimen. This results in the detector being at an angle of 2θ to the incident radiation while the sample is at an angle, θ (Figure 4). A typical diffractometer is shown in Figure 5. A scintillation counter was used rather than a proportional counter as it does not require a pre-amplifier. This is due to detection being a two stage process. In the first stage the x-ray photon is absorbed and then remitted at a longer wavelength in the form of blue light. This is achieved using a scintillator, which is typically sodium iodide doped with thallium and produces light photons with wavelengths of ca. 4100Å. The second stage converts the light into voltage using a photomultiplier and the electrons produced are then focused through a chain of ten more photosurfaces each at a higher potential than the one before, which gives the signal a higher gain. Using a scintillation counter also gives a quantum yield for copper radiation of 95% compared to 75% with a proportional counter, and it also has a longer life span. The resulting pattern is recorded onto a computer and a search can be performed against the JCPDS standard database[12], to identify the nature of the material under examination.

2.3. LATTICE PARAMETER MEASUREMENTS

A least squares treatment is one of the best methods for the precise determination of lattice parameters as it reduces random errors by picking the best line of fit through a series of experimental points. Systematic errors may also be eliminated by the selection of a suitable extrapolation function. Typically the extrapolation function used is:

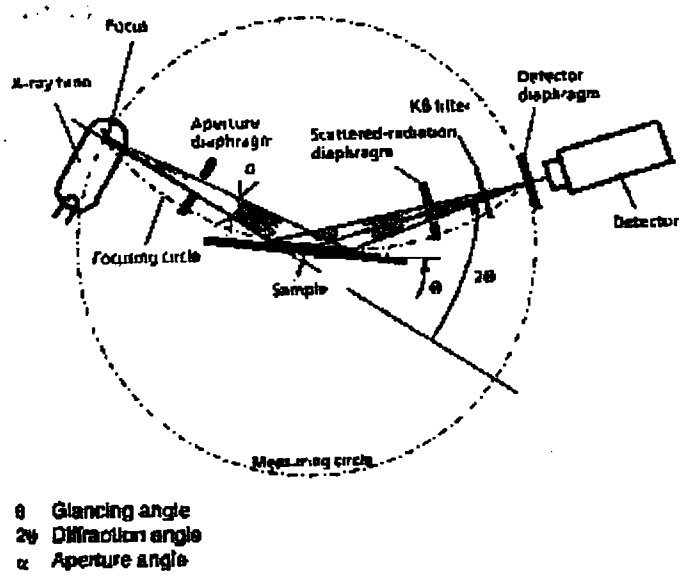

Figure 4. The x-ray beam path

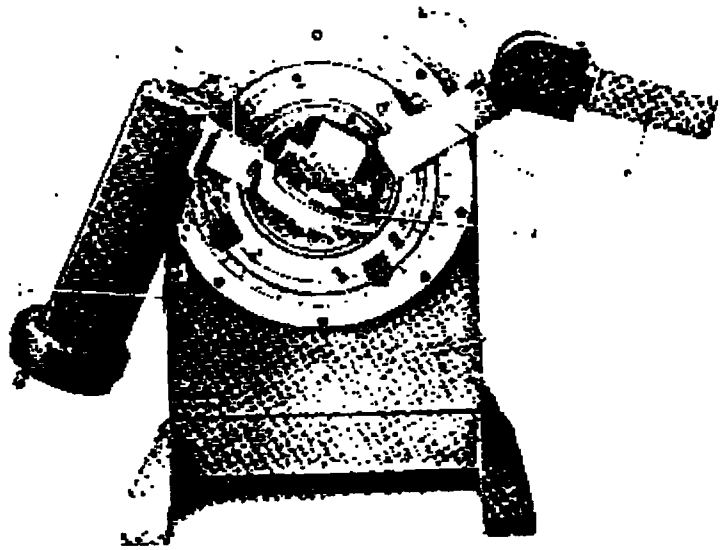

Figure 5. A typical x-ray diffractometer

$$\frac{\Delta d}{d} = K\cos^2\theta \qquad (12)$$

where d is the interplanar distance and θ is the angle of incidence between the x-rays and the plane of atoms (Figure 3a, page 26). Instead of using the least-squares method to find the best straight line on a plot of a against $\cos^2\theta$ Cohen applied the method to the observed $\sin^2\theta$ values directly.[13] Hence this method is superior even to graphical methods as it eliminates any human error in making measurements from a graph.

Squaring the Bragg Law and taking logarithms of each side gives:

$$\ln\sin^2\theta = \ln(\lambda^2/4) - 2\ln d \qquad (13)$$

Differentiation then gives:

$$\frac{\Delta\sin^2\theta}{\sin^2\theta} = -\frac{2\Delta d}{d} \qquad (14)$$

Combining Equations 12 and 14 gives:

$$\Delta\sin^2\theta = D\sin^2 2\theta \qquad (15)$$

Equation 15 means that the total effect of the systemic errors in the observed value of $\sin^2\theta$ can be represented by the amount $D\sin^2 2\theta$.

Now, by definition, the error function in $\sin^2\theta$ is the difference between the observed value of $\sin^2\theta$ and the true value of $\sin^2\theta$. This can be represented as:

$$\Delta\sin^2\theta = \sin^2\theta(\text{observed}) - \sin^2\theta(\text{true}) \qquad (16)$$

An expression representing the true value of $\sin^2\theta$ is well documented for each crystal system and substituting this expression into Equation 16 enables a set of normal Equations to be produced. Simultaneously solving this set of normal Equations allows the unknown quantities to be determined. The lattice parameters can then be readily determined. For cubic and hexagonal systems there are examples given in the literature (see references on page 24). For the orthorhombic system the Equations have to be derived, and are of a complexity which usually makes them excessively cumbersome.

In this work computerisation enabled the equations associated with the orthorhombic system to be solved routinely (Appendix A).

2.4. MÖSSBAUER SPECTROSCOPY

There are several accounts of the theory and practice of Mössbauer spectroscopy, of which the most thorough is by Greenwood and Gibb,[14] and a very useful summary is given by Berry.[15] The fundamental points are described in the following sections.

2.4.1. The Mössbauer effect

Mössbauer spectroscopy involves the resonant absorption and emission of γ–rays by nuclei. The source of γ–rays usually consists of a solid matrix in which a radioactive substrate is embedded. The radioactive isotope decays into the Mössbauer isotope in an excited state, which subsequently relaxes and emits a γ-ray. For a Mössbauer transition, the energy of the γ-ray must not be modified by nuclear recoil. This can be ensured by incorporation of the Mössbauer nuclei in a crystal lattice. Provided the energy of nuclear recoil associated with absorption and emission of γ-rays is small compared to the lowest quantized lattice vibration, recoil-free nuclear transitions suitable for a Mössbauer experiment can take place.

The γ-rays are of very precisely defined energy, and the energy of the transition between the excited and ground states of the Mössbauer nucleus is usually slightly different in the source and absorber. The energy of the incident γ-rays therefore rarely corresponds to the energy of the transition of the absorber Mössbauer atom. The γ-ray energy is therefore modified using the Doppler effect, by vibrating the source so that a range of γ-ray energies is produced. The γ-ray energies are usually presented in terms of the velocity of the source in mm/s. The experimental arrangement along with the nuclear processes that occur for the Mössbauer atoms in the same cubic environment in the source and absorber are presented schematically in Figure 6.

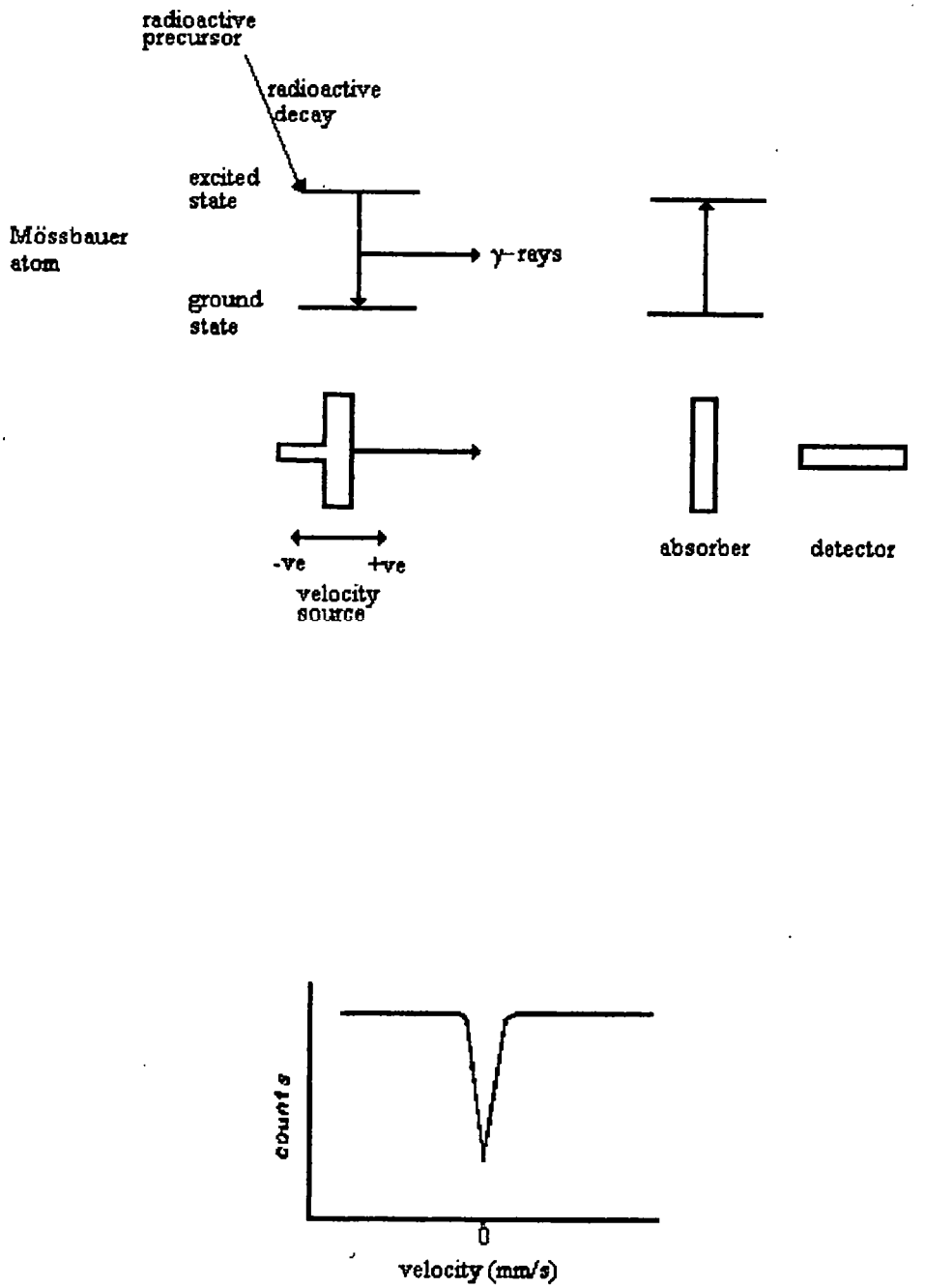

Figure 6. A schematic representation of a Mössbauer experiment, and a spectrum recorded with source and absorber nuclei in the same cubic environments.

2.4.2. Measurements from spectra and their significance

The environment of the nucleus influences the nuclear energy levels which in turn results in the Mössbauer spectrum recorded exhibiting hyperfine interactions. These hyperfine interactions are; the chemical isomer shift, the magnetic hyperfine splitting and the quadrupole splitting and are discussed below.

(a) Chemical isomer shift

The origin of the chemical isomer shift may be understood by first considering a nucleus stripped of all its electrons. In this nucleus the energy of the transition between the ground and excited states may be represented by E, Figure 7(a). If the same nucleus is surrounded by electrons a coulombic attraction between the nuclear and electronic charges will occur, and the nuclear energy levels will be modified. If the size of the nucleus in the excited and ground state was the same, then the interaction of these states with the electrons would also be the same. The energy levels will therefore be changed by the same degree, and the energy of the transition will also be E, (Figure 7(b)). However, if the size of the ground and excited states differ, as is usually the case, the energies of the excited and ground states will be modified to a different extent, and the energy of the transition will no longer be E, but some new value E' (Figure 7(c)).

The nuclear energy levels will also depend on the electronic environment. Thus if the absorber and source nuclei are in different electronic environments, their nuclear energy levels will be modified to differing extents (Figure 8(a)). The Mössbauer spectrum therefore exhibits an absorption whose energy is shifted from that corresponding to the energy of the transition in the source (Figure 8(b)). This shift, δ, is called the chemical isomer shift which is sometimes abbreviated to isomer shift. The chemical isomer shift is not however an absolute quantity, and to compare chemical isomer shift data from other absorbers, the chemical isomer shifts are expressed relative to a standard absorber that is specific to the particular isotope in use.

The chemical isomer shift can be related to the electronic environment of the absorber nucleus by:

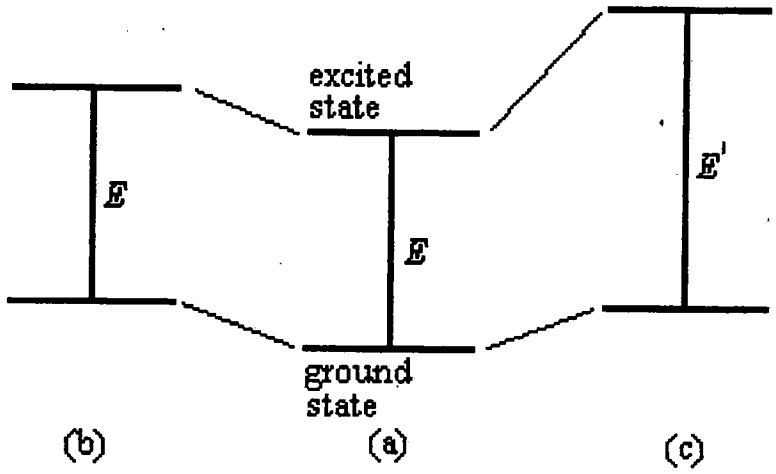

Figure 7. Nuclear energy level of (a) a bare nucleus, and a nucleus in an atom for which the nuclear excited state and ground states are (b) the same size, and (c) different sizes.

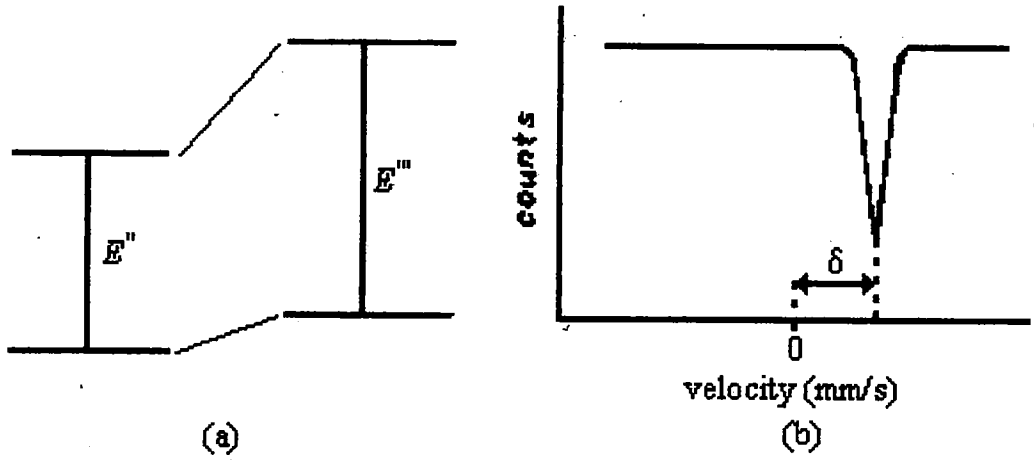

Figure 8. Nuclear energy levels of source and absorber atoms in different environments (a), and the resulting Mössbauer spectrum (b).

$$\delta = \text{constant}\frac{\Delta R}{R}(\Psi_s^2(o)_A - \Psi_s^2(o)_S) \qquad (17)$$

where $\Delta R/R$ is $(R_e-R_g)/R_g$, and R_e and R_g are the radii of the nucleus in the excited and ground states respectively. $\Psi_s^2(o)_A$ and $\Psi_s^2(o)_S$ are the s-electron densities at the absorber and source nuclei respectively.

The value of $\Psi_s^2(o)$ depends primarily on the population of the s-orbitals but is also influenced by electrons occupying other types of orbital, since these shield the interaction of the nucleus with the s-electrons.

For a particular source $\Psi_s^2(o)_S$ will be constant so that changes in chemical isomer shift reflect changes in $\Psi_s^2(o)_A$. Thus the chemical isomer shift gives information about the electronic environment of the nucleus and can therefore be used as a probe of oxidation state. The sign of $\Delta R/R$ for ^{57}Fe is negative, so increasing s-electron density at the nucleus results in smaller isomer shifts.

(b) Quadrupole splitting

Any nucleus with a spin, I, greater than 1/2 has an asymmetric charge distribution which may be represented by a nuclear quadrupole moment. This can interact with an asymmetric electric field represented by an electric field gradient, resulting in the partial or complete splitting of nuclear levels. Since more than one nuclear transition can then occur, a multi-line Mössbauer spectrum will be observed. The selection rule for nuclear transitions is $\Delta m = 0 \pm 1$. For ^{57}Fe the excited and ground states have spins of 3/2 and 1/2 respectively, so for this isotope the presence of an electric field gradient gives rise to a two line spectrum, whose quadrupole splitting is Δ (Figure 9).

Contributions to an electric field gradient may arise from the arrangement of charge external to the Mössbauer atom, i.e. the lattice, or the arrangement of valence electrons of the Mössbauer atom. The valence electron term may itself be considered to consist of two contributions related to non-bonding electrons, and electrons involved in bond formation.

(c) Magnetic splitting

Since a nucleus of spin $I \neq 0$ has a magnetic moment, it can interact with a magnetic field, and the nuclear levels can be split.

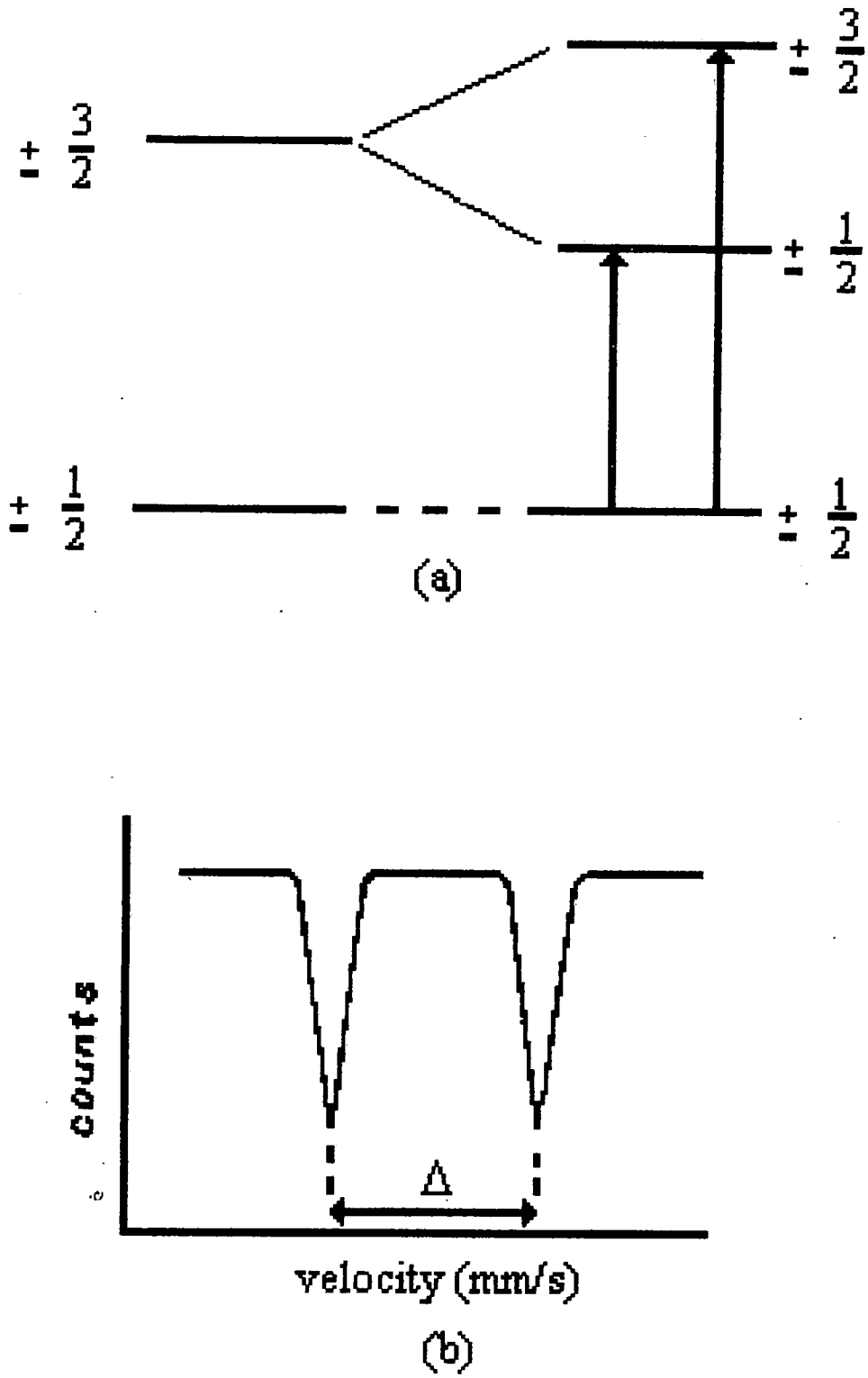

Figure 9. Splitting of nuclear energy levels for ^{57}Fe, by the presence of an electric field gradient (a), and the resulting Mössbauer spectrum (b).

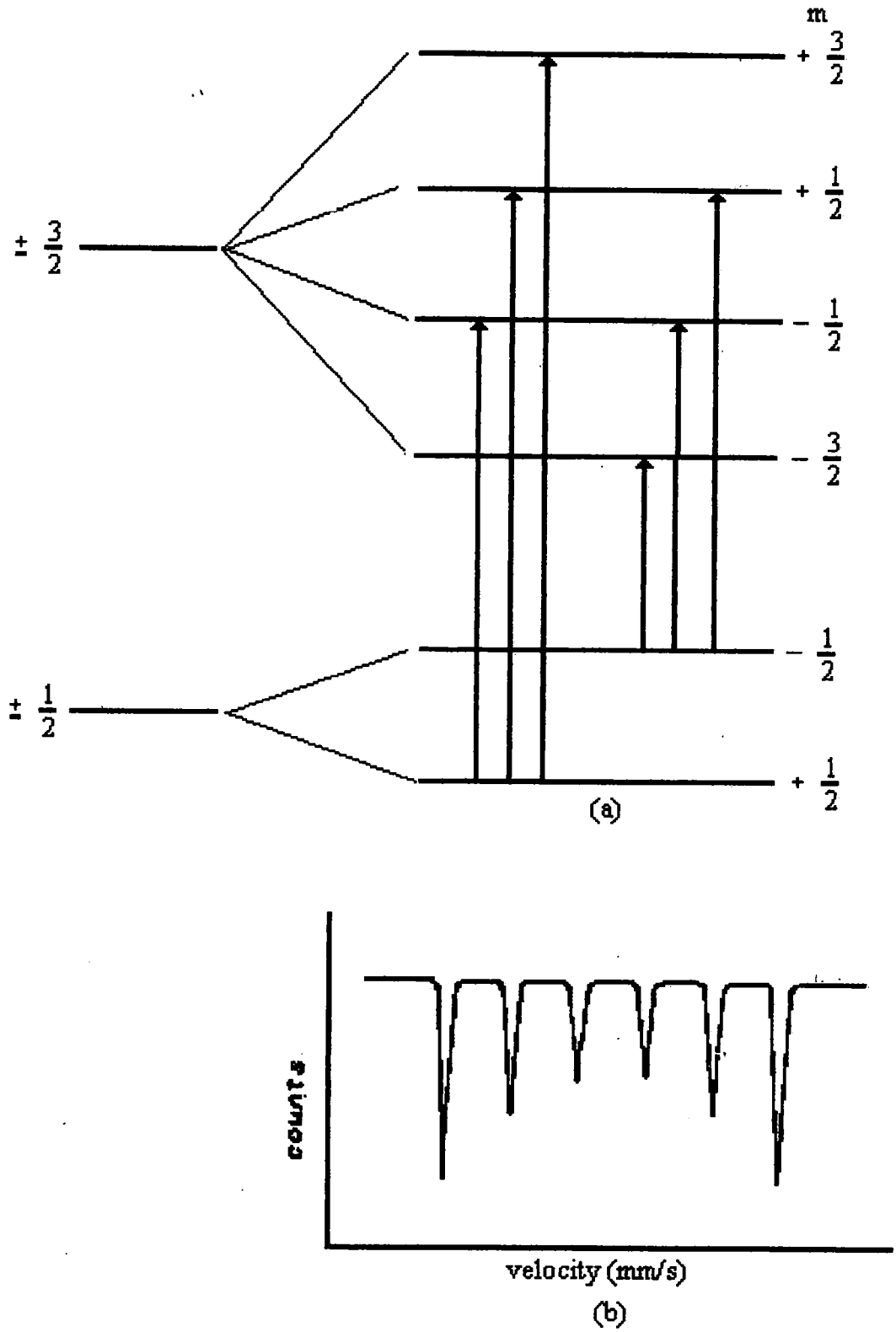

Figure 10. Splitting of nuclear energy levels of a ^{57}Fe nucleus by an applied magnetic field (a), and the resulting Mössbauer spectrum (b).

The most common mechanism by which the nucleus experiences a magnetic field is the polarisation of s-electrons, which results in an imbalance of s-electron spin density at the nucleus.

This polarisation usually occurs by the interaction of s-electrons with unpaired electrons associated with the Mössbauer atom. The interaction of the nucleus and the magnetic field splits the nuclear states into 2I+1 sub-states. Since the selection rule for nuclear transitions is $\Delta m = 0 \pm 1$, and ^{57}Fe has an excited and ground state of spin, I, of 3/2 and 1/2 respectively, magnetic hyperfine splittings result in six line Mössbauer spectra for this isotope, (Figure 10).

2.4.3. The effect of small particles

The type of magnetic ordering in a structure can have a temperature dependence. A good example of this is α-Fe_2O_3 which is antiferromagnetic at low temperature (<260K), undergoes a transition above the Morin temperature to become weakly ferrimagnetic and finally becomes paramagnetic above the Néel temperature of 960K. The Mössbauer spectra show six-lines above and below the Morin transition and show two lines above the Néel temperature. These effects are observed for samples with particle sizes above 18 nm. Studies on small particle α-Fe_2O_3 supported on high area silica have shown that complications arise for particle sizes below 18 nm[16,17]. For particle sizes <10 nm the Mössbauer spectrum shows two lines, corresponding to a paramagnetic state, while for particle sizes between 10 nm and 18 nm an eight line spectrum is observed, which is a combination of the ferrimagnetic six line spectrum and the paramagnetic two line spectrum. The ratio of the paramagnetic state to the ferrimagnetic state decreases with increasing particle size in this region. As paramagnetism is being observed well below the Néel temperature it is referred to as superparamagnetism. The cause of this effect is that in an assembly of particles, each with a volume, v, there is a finite probability proportional to $e^{(-2Kv/kT)}$, (where k is the Boltzman constant,) that the magnetisation vector will spontaneously change its direction. The relaxation time, τ_o, which indicates how rapidly this transition occurs, may be written as:

$$\tau_0 = \left(\frac{1}{af}\right)e^{(-2Kv/kT)} \quad (18)$$

where a is a geometric factor and f is a frequency factor. Clearly as the volume of the particle decreases, so does the relaxation time and when $\tau_0 << \tau_{obs}$ the particles will show superparamagnetic behaviour. In this scenario $\tau_{obs} = 2.5 \times 10^{-8}$s.

2.5. MAGIC ANGLE SPINNING NUCLEAR MAGNETIC RESONANCE (MASNMR)

The fundamentals of NMR spectroscopy are discussed below with particular emphasis on the solid state. The main source of reference is by Harris,[18] with additional references to Mortimer,[19] and Ebsworth *et al.*[20]

2.5.1. Theory of NMR

NMR has developed since the first experiments which were performed in 1945, and the first commercial spectrometer available in 1953, to become one of the most important forms of spectroscopy available to scientists. The scope of this technique is reaching into many solid-state applications because of the increasing number of nuclei available for investigation and the continuing development of magic-angle spinning n.m.r.

The phenomenon of nuclear magnetic resonance is restricted to those isotopes whose nuclei possess the property of nuclear spin. In quantum-mechanical terms it is the property of spin that is responsible for the magnetic behaviour. It is characterised by a nuclear spin quantum number, I. Nuclear spin cannot be predicted, but it can be measured experimentally and there are three relationships which have been established:

(a) Nuclei with odd mass number have half-integral nuclear spin.

(b) Nuclei with even mass numbers, but an odd charge number, have integral nuclear spin.

(c) Nuclei with an even mass number and an even charge number have zero spin.

When I is non-zero the nucleus exhibits a nuclear magnetic moment, μ given by the Equation:

$$\mu = \gamma\hbar[I(I+1)]^{1/2} \quad (19)$$

where γ is the magnetogyric ratio. The magnetogyric ratio is a constant characteristic of the particular isotope and can be positive or negative.

The nuclear magnetic moment is a vector quantity described by the magnetic quantum number, m_I, and it may only adopt orientations that have components μ_z along the z-axis of a set of regular Cartesian coordinates:

$$\mu_z = \gamma \hbar m_I \tag{20}$$

In the absence of a magnetic field, the spin states corresponding to the different values of m_I are degenerate, but in the presence of a magnetic field, B_0, there is an interaction between the field and the magnetic nucleus which lifts the degeneracy of the spin states. In classical terms the energy of this interaction, E, is:

$$E = -\mu_z B_0 \tag{21}$$

The allowed magnetic energy levels in the quantum mechanical case are found by combining Equations 20 and 21 to give:

$$E = -\gamma \hbar m_I B_0 \tag{22}$$

In this situation there are (2I+1) non-degenerate energy levels each separated by $|\gamma \hbar B|$. Transitions can be induced between these levels when electromagnetic radiation of the correct frequency, ν, is applied. This gives the resonance condition for a single nucleus:

$$\nu = \left| \frac{\gamma}{2\pi} \right| B_0 \tag{23}$$

This can be rewritten as

$$|\gamma| = \frac{2\pi\nu}{B_0} \tag{24}$$

The quantity $2\pi\nu$ is an angular frequency, which has the units, rad s^{-1}. The units of γ are thus rad s^{-1} T^{-1} and have been tabulated.

All nuclei that have the property of spin possess a magnetic dipole moment. Those nuclei which have spin I> 1/2 also possess a nuclear electric quadrupole moment, which is caused

by the lack of a uniform distribution of positive charge within the nucleus. These nuclei are known as quadrupolar nuclei and may be pictured as spheres of charge which are distorted with respect to the quantisation axis. This distortion results in a flattened (oblate) or elongated (prolate) charge nucleus. Quadrupolar nuclei however also have much broader lineshapes and therefore are sometimes effectively unobservable. Hence NMR studies of nuclides with I>1/2 are not as extensive as those for I=1/2.

a) The suitability of nuclei for n.m.r. spectroscopy

An approximate guide to the suitability of a nucleus for NMR is given by its receptivity. The receptivity, D_x of an isotope X of element Z, is given by the Equation:

$$\Delta n = \Delta n_e\left(1-\frac{1}{e^{(\frac{\Delta E}{kT})}}\right)D_x = C_x\left|\gamma x^3\right|I_x(I_x+1) \qquad (25)$$

where C_x is the natural abundance of the isotope. Receptivity provides a way of comparing the expected NMR signal strength from an isotope at a fixed magnetic field with that of another isotope providing that the same total amount of element is present in each case. As ^1H and ^{13}C represent the most-studied of NMR nuclides it is usual to quote a relative receptivity with respect to one or other of these species.

b) Population of energy levels

In an NMR sample containing nuclei of spin I=1/2 at thermal equilibrium in a large magnetic field, the nuclei will be distributed between two allowed magnctic energy levels according to the Boltzman law:

$$\frac{N_+}{N_-} = e^{\left(\frac{\Delta E}{kT}\right)} \qquad (26)$$

where T is the temperature in Kelvin, k is the Boltzman constant and N_+ and N_- are the number of nuclei in the lower energy and higher energy levels respectively. Quantum mechanics shows that irradiation at the correct frequency will cause transitions from either the high or the low energy levels, such that for individual nuclear spins, the probability per unit time of a transition from m_I=-1/2 to m_I=1/2 is equal to the probability of the reverse

transition. The excess population in the lower energy level is very small, and hence NMR is a relatively insensitive technique compared to other forms of spectroscopy.

c) Spin-lattice relaxation

The probability of a transition occurring spontaneously in the spin system described is negligible. Hence after an input of radio-frequency energy it would seem possible that the energy level populations could become equal as nuclei are excited and transfer from the lower energy level to the higher energy level. If the energy level populations did become equal there would be no net absorption of energy and the spectrum would be significantly weakened, resulting in a phenomenon called saturation.

In reality this does not occur because of spin-lattice relaxation. In the liquid state, the local magnetic field created at a particular nucleus by the magnetic dipole moments of surrounding nuclei will fluctuate as the nuclei undergo random motion. Some of these fluctuations will, by chance, contain contributions at the resonance frequency and will be able to stimulate transitions between energy levels. The general chaotic motion in the vicinity of a nucleus acts as an acceptor of energy and allows nuclei to return to the ground state. Thus spin-lattice relaxation allows nuclei to transfer magnetic energy to their surroundings and so eliminate a thermal disequilibrium by moving from an excited state to a ground state.

Spin-lattice relaxation is an exponential process and can be represented by the Equation:

$$\Delta n = \Delta n_e\left(1-\frac{1}{e^{\left(\frac{t}{T_1}\right)}}\right) \qquad (27)$$

where Δn_e represents the thermal equilibrium population difference, Δn is the population difference at time t and T_1 is a time constant known as the spin-lattice relaxation time. The value of T_1 reflects the efficiency with which the spin system can lose magnetic energy to its surroundings.

Spin-lattice relaxation is not the only relaxation process known. Another relaxation process called spin-spin relaxation occurs and is a factor influencing the width of an n.m.r. line. In the process of spin-spin relaxation an excited spin state exchanges energy with an

adjacent spin-active nucleus. The spin-spin relaxation time is known as T_2 and the longer the value of T_2, the narrower the n.m.r. line. In liquid and solution samples $T_1 \geq T_2$.

Quadrupolar nuclei interact strongly with their local electronic environment as they possess an electric quadrupole moment. The interaction of quadrupolar nuclei with fluctuating electric field gradients can provide a very efficient spin-lattice relaxation mechanism for magnetic energy levels which results in quadrupolar nuclei often having short T_1 values. The short T_1 values of quadrupolar nuclei give rise to broad n.m.r. lines, unless the nucleus concerned is an environment of high electrical symmetry, such as tetrahedral, octahedral, spherical or cubic.

d) Chemical shielding

In an external magnetic field the electron cloud surrounding an atom will be induced to circulate around the nucleus about the direction B_o This circulation of charge produces a secondary magnetic field which opposes B_o Hence the electrons 'shield' the nucleus from the full influence of B_o. The magnitude of the effective field, B, at the nucleus is given by:

$$B = B_o(1-\sigma) \tag{28}$$

where σ is a dimensionless number called the (chemical) shielding constant. The shielding constant is usually quoted in parts per million (ppm.), and for free atoms it represents the total shielding. For molecules the situation is more complex, as the presence of other nuclei hinders the rotation of the electron cloud at the nucleus of interest. The result is that the shielding constant σ_i for a nucleus i in a molecule depends on its chemical environment. The Equation for resonance frequency allowing for a chemical shielding term can be expressed as a generalised form of Equation 23:

$$\nu_i = \left|\frac{\gamma}{2\pi}\right| B_o(1-\sigma) \tag{29}$$

For a given nucleus, differences in the resonance frequency are referred to as chemical shifts.

e) Spin-spin coupling

Spin-spin coupling is the indirect coupling of nuclei with one another via the electrons of intervening chemical bonds. For example, the ^{13}C n.m.r. spectrum of 99% enriched ^{13}C $CHCl_3$ consists of a doublet which arises from an interaction between the ^{13}C nuclear spin and the two spin states of ^{1}H. The applied field is slightly augmented by the field due to one of the spin states of ^{1}H and slightly diminished by the opposite spin state. This is an example of heteronuclear spin-spin coupling. The magnitude of a spin-spin coupling is determined by the spin-spin coupling constant, *J*, which is often referred to as the 'coupling constant' and is dependent on the chemical environment. Coupling can occur over a number of chemical bonds and coupling constants are classified according to the number of intervening bonds by attaching a superscript prefix to the symbol J. Thus direct coupling is indicated by ^{1}J, geminal coupling by ^{2}J and vicinal coupling is indicated by ^{3}J. Coupling constants can be useful sources of chemical information, but it is often desirable to remove spin-spin coupling effects. The removal of spin-spin coupling effects is referred to as decoupling, which in the case of heteronuclear decoupling is usually achieved by broad-band decoupling. Broad-band decoupling is a technique which works by subjecting the sample to strong irradiation with frequencies covering the whole of the ^{1}H resonance range.

2.5.2. Magic angle spinning

In general there are three major problems to overcome in measuring high resolution NMR spectra for solids.

The first problem is that direct magnetic dipolar interactions between nuclei contribute to the observed NMR spectrum. This occurs because an NMR resonance can extend over a number of kHz and it is usually featureless because a given magnetic dipole will interact with all other magnetic dipoles in the local environment. In solution spectra this is averaged out by rapid molecular motion.

The second problem is that because of the lack of molecular mobility in solids, nuclear spin-lattice relaxation times can often be very long and this gives rise to practical problems in obtaining a spectrum with a good signal/noise ratio.

The third problem is that the magnitude of a chemical shielding constant is related to the orientation of the molecular force with respect to the applied field. If it was possible to take a single molecule and measure its shielding constant, σ, the value of σ would be found to vary as the orientation of the molecule was changed with respect to the field. For polycrystalline or amorphous samples, the molecules, or molecular groups, will be oriented in all possible directions and so there will be a spread of chemical shifts, resulting in broad resonance lines. This chemical shielding anisotropy often gives rise to line-widths up to several kHz. In solution spectra, the effects of chemical shielding anisotropy are averaged out by rapid molecular motion.

A number of techniques have been developed to overcome the problems mentioned:

High-power decoupling techniques remove magnetic dipolar broadening (Figure 12(a) compared to Figure 12(b)). In the case of ^{13}C or ^{29}Si, for which only heteronuclear couplings are important, spectra with resolution comparable to solutions can be obtained.

The problem of low-sensitivity due to long spin-lattice relaxation times is alleviated by cross-polarisation, which is usually applied simultaneously with decoupling. For dilute nuclei with spin 1/2, in the presence of abundant spins, magnetisation from the abundant spin, γ_a, usually (^1H) can be transferred to the dilute spin, γ_d, giving an intensity gain of γ_a/γ_d, by making the value of T_1 irrelevant for the dilute spin. Moreover, the cross-polarisation can be performed many (usually 10 to 20) times in one pulse sequence.

Finally, to remove chemical shielding anisotropy, magic angle spinning (MAS) is used. This method works by simulating the rapid isotropic molecular tumbling which occurs naturally in non-viscous solutions. The chemical shielding anisotropy effect which causes NMR line broadening in solids involves the geometric factor $(3\cos^2\theta - 1)$, where θ is the angle between the internuclear vector quantity, **r**, and the applied magnetic field. The average of $(3\cos^2\theta - 1)$ about the conical path of **r** (Figure 11) when rotated about a fixed axis subtending an angle β to the applied magnetic field is given by:

$$(3\cos^2\theta - 1) = \tfrac{1}{2}(3\cos^2\beta - 1)(3\cos^2\chi - 1) \qquad (30)$$

The parameter χ is fixed for a rigid solid although it takes all values if the material is a powder. The $(3\cos^2\beta - 1)$ term therefore acts a scaling factor. The angle β can be

controlled by the experimenter, and when β = 54.7°, $(3\cos^2\beta - 1)=0$. The chemcal shielding anisotropy is therefore eliminated, giving much higher resolution.

When performing magic-angle spinning n.m.r. spectroscopy, considerations other than the placement angle of the sample are the packing of the sample and the rotation of the sample. The sample must be in a compressed cylindrical form and it must be rotated very rapidly about its own axis. The rotation about the sample axis must be larger than the static bandwidth expressed in Hz in order for the chemical shielding anisotropy and dipolar interactions to be averaged. The highest rotation rate possible mechanically is 10-12 kHz which is sufficient for some nuclei such as ^{13}C or ^{29}Si, but for many it is not fast enough, which limits the general applicability of the technique. In the cases where the maximum rotation rate of 12 kHz is insufficient each single resonance in a spectrum is replaced by a central line and a series of spinning sidebands. The spinning sidebands are dependent on the form and magnitude of the chemical shielding interactions. The central line is not necessarily the most intense, but side and centre bands can usually be distinguished by repeating the experiment using several different spinning speeds.

2.5.3. Interpretation of spectra

In this work the ^{29}Si MASNMR spectra are interpreted in terms of the structure of the silicate groups using the Q^n notation.[21] In this notation, Q represents a silicon atom tetrahedrally coordinated to four oxygen atoms and the superscript *n* indicates the number of other Q units attached to it. Thus Q^0 denotes the monomeric orthosilicate anion SiO_4^{4-}, Q^1 end-groups of chains, Q^2 middle groups in chains or cycles, Q^3 chain-branching sites and Q^4 three-dimensionally crosslinked groups. The degree of protonation is ignored in this description. The coordination via oxygen bridges of a Q^n unit to mAlO$_4$ tetrahedra is described by the notation $Q^n(m\text{Al})$.

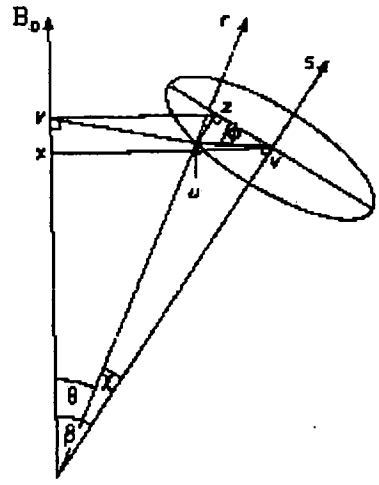

Figure 11. A schematic diagram of the spinning of a polycrystalline sample, about an axis inclined at angle β to the field B_0 produced by a solenoid magnet.

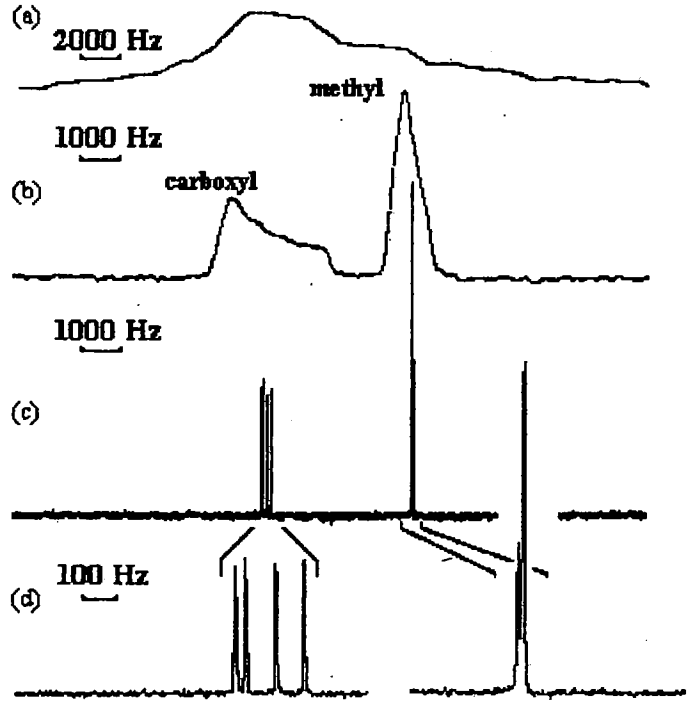

Figure 12. ^{13}C spectrum of $2Ca(CH_3CO_2)_2.H_2O$ at 22.6 MHz recorded under the following conditions (a) static, (b) static with high-power proton decoupling, (c) with decoupling and MAS and (d) expansion of (c) to show fine structure.

2.6. REFERENCES

[1] H. de Sénarmont *Ann. Chim. Phys.* 1851 **32** 129

[2] G. W. Morey *J. Am. Ceram. Soc* 1914 **36** 215

[3] J. S. Huebner in *Research Techniques for High Pressure and High Temperature,* Ed. G. C. Ulmer 1971 Springer-Verlag New York 123

[4] O. F. Tuttle *Geol. Soc. Am. Bull.* 1949 **60** 1727

[5] J. C. Joubert and J. Chenavas *Treatise on Solid-State Chemistry: Vol. 5 Changes of State.* Ed. N. B. Hannay 1975 Plenum Press, New York 463

[6] H. Jacobs and D. Schmidt *Curr. Top. Mater. Sci.* 1982 **8** 381

[7] W. J. Dawson *Ceram. Bull.* 1988 **67** 1673

[8] R.A Laudise and J. W. Nielsen in *Solid State Physics; Advances in Research and Applications Volume 12* Ed. F. Seitz and D. Turnbull 1961 Academic Press New York

[9] H. P. Klug and L. E. Alexander *X-Ray Diffraction Procedures* 1967 J. Wiley & Sons New York

[10] L. V. Azàroff, R. Kaplow, N. Kato, R. J. Weis, A. J. C. Wilson and R. A. Young *X-Ray Diffraction* 1974 McGraw-Hill, Inc., U.S.A.

[11] B. D. Cullity *Elements of X-ray Diffraction* 1978 Addison Wesley Publishing Co., New York

[12] International Centre for Diffraction Data PDF-2 Database on CD-ROM

[13] M. U. Cohen *Rev. Sci. Instruments* 1935 **6** 68

[14] N. N Greenwood and T. C. Gibb 1971 *Mössbauer Spectroscopy* Chapman & Hall, London.

[15] F. J. Berry 1990 in *Physical Methods in Chemistry* B. W. Rossiter and J. F. Hamilton, J. Wiley and Sons, London.

[16] W. Kundig, H. Bommel, G. Constabaris and R. H. Lindquist *Phys. Rev.* 1966 **142** 327

[17] F. J. Berry in *Advances in Inorganic Chemistry and Radiochemistry* 1978 **21** 255

[18] R. K Harris, 1983 *Nuclear Magnetic Resonance Spectroscopy* Pitman, London.

[19] M. Mortimer 1989 in *S343 Inorganic Chemistry Blocks 5* The Open University, Milton Keynes.

[20] E. A. V. Ebsworth, D. W. H. Rankin and S. Craddock 1987 *Structural methods in Inorganic Chemistry* Blackwell, London.

[21] G. Engelhardt and D. Michel 1987 *High Resolution Solid-State NMR of Silicates and Zeolites*, Wiley, Chichester.

Chapter 3
Experimental

3.1. SYNTHESIS OF MATERIALS

3.1.1. Hydrothermal processing of aluminium-, silicon-, magnesium- and iron- acetates

Metal acetate (10g) was mixed with water (100 ml) and stirred. The resulting suspension was transferred to the Teflon liner of the autoclave and hydrothermally processed at 220°C for 3 hours at autogenous pressure. The resulting sol was transferred to a beaker and dried using a hotplate with an overhead infrared lamp in a fume cupboard. The dried material was ground in an agate pestle and mortar and divided into small portions. These portions were calcined in an alumina crucible in air for either 3 or 6 hours at a range of temperatures between 300°C and 1400°C using a ramp rate of 3°C/min during both the heating and cooling of the samples.

The size of the portions was determined on the basis of the weight losses which were observed during the calcination of a trial sample. It was found that in order to produce enough sample to analyse thoroughly at each calcination temperature the following scheme should be used. For calcination temperatures <500°C the sample size should be ca. 0.5g. For calcination temperatures between 500°C and 1000°C the sample size should be ca. 0.75g and for calcination temperatures >1000°C the sample size should be ca. 1g.

3.1.2. Mullite.

a) Commercial mullite

A sample of mullite powder was obtained from Baikalox plc.

b) Mullite prepared by conventional methods

Stoichiometric quantities of silica and corundum were ground together in an agate pestle and mortar and calcined at 1500°C for 6 hours in air.

c) Hydrothermal synthesis of mullite

Stoichiometric quantities of aluminium and silicon- acetate were mixed with water (350 ml) and stirred. The resulting suspension was transferred to the Teflon liner of the

autoclave and hydrothermally processed at 220°C for 3 hours at autogenous pressure. The resulting sol was then dried and calcined using the procedure described in Section 3.1.1.

3.1.3. Hydrothermal processing of aluminium- and silicon- acetates in the presence of HCl

Metal acetate (10g) was mixed with water (100 ml) and stirred. The pH of the resulting suspension was modified to a value of 3.3* using 0.1M HCl before being transferred to the Teflon liner of the autoclave and hydrothermally processed at 220°C for 3 hours at autogenous pressure. The resulting sol was then dried and calcined using the procedure described in Section 3.1.1.

3.1.4. Hydrothermal synthesis of mullite in the presence of HCl

Stoichiometric quantities of aluminium- and silicon- acetate were mixed with water (350 ml) and stirred. The pH of the resulting suspension was modified to a value of 3.3 using 0.1M HCl, before being transferred to the Teflon liner of the autoclave and hydrothermally processed at 220°C for 3 hours at autogenous pressure. The resulting sol was then dried and calcined using the procedure described in Section 3.1.1.

3.1.5. Hydrothermal processing of silicon acetate at varying pH

Silicon acetate (2.5g) was mixed with water (300 ml) and stirred. The pH of the suspension was measured using a pH meter calibrated with buffers at pH 7 and 4. The pH was modified to pH 1 using conc. HCl. The suspension was then transferred to the Teflon liner of the autoclave and hydrothermally processed at 220°C for 3 hours at autogenous pressure. The resulting sol was then dried and calcined using the procedure described in Section 3.1.1.

---

* A value of pH 3.3 was used in all preparative work where acidification was incorporated so that the results obtained from the work could be compared to the work performed in reference 72 (p102)

This procedure was repeated using differing quantities of conc. HCl or 5M NaOH to produce suspensions at pH 2, pH 3 and pH 7.

3.1.6. Hydrothermal co-processing of iron- acetate with either aluminium- or silicon- acetate.

In the following experiment the iron : aluminium ratio used was 14 mol% and the iron : silicon ratio was 43 mol%.

Metal acetate and the appropriate amount of iron(II) acetate were mixed with water (350 ml) and stirred. The resulting suspension was transferred to the Teflon liner of the autoclave and hydrothermally processed at 220°C for 3 hours at autogenous pressure. The resulting sol was then dried and calcined using the procedure described in Section 3.1.1.

3.1.7. Iron-doped mullite

In the following experiments the percentages of iron added are mol% with respect to aluminium.

a) Hydrothermal synthesis of mullite with 7%, 14% and 21% iron(III) acetate

Stoichiometric quantities of aluminium and silicon- acetate together with the appropriate amount of iron(III) acetate were mixed with water (350 ml) and stirred. The resulting suspension was transferred to the Teflon liner of the autoclave and hydrothermally processed at 220°C for 3 hours at autogenous pressure. The resulting sol was then dried and calcined using the procedure described in Section 3.1.1.

b) Hydrothermal synthesis of mullite with 14% iron(II) acetate

Stoichiometric quantities of aluminium and silicon- acetate together with the appropriate amount of iron(II) acetate were mixed with water (350 ml) and stirred. The suspension that was formed was transferred to the Teflon liner of the autoclave and hydrothermally processed at 220°C for 3 hours at autogenous pressure. The resulting sol was then dried and calcined using the procedure described in Section 3.1.1.

3.1.9. Preparation of spinel

a) Hydrothermal synthesis of spinel using aluminium- and magnesium- acetates

Stoichiometric quantities of aluminium- and silicon acetate, were mixed with water (350 ml) and stirred. The resulting suspension was transferred to the Teflon liner of the autoclave and hydrothermally processed at 220°C for 3 hours at autogenous pressure. The resulting sol was then dried and calcined using the procedure described in Section 3.1.1.

b) Hydrothermal synthesis of spinel using aluminium- and magnesium- acetates

Stoichiometric quantities of aluminium- and silicon acetate, were mixed with water (350 ml) and stirred. The pH of the suspension that was formed was modified to a value of 3.3 using 0.1M HCl before being transferred to the Teflon liner of the autoclave and hydrothermally processed at 220°C for 3 hours at autogenous pressure. The resulting sol was then dried and calcined using the procedure described in Section 3.1.1.

3.2. WASHING OF SAMPLES IN ACID

Mullite powder (3g) was mixed with ca. 5M HCl (ca. 30 ml) and heated under reflux for 3 days using a heating mantle. On cooling the resulting suspension was centrifuged at 2000 rpm for 10 mins. and the supernatant liquid was removed. The sample was then dried in a drying oven and analysed by x-ray powder diffraction. The procedure was then repeated.
In order to obtain a powder from the sample of commercial mullite tubing, a section was cut off using a diamond saw. The cut section was then smashed with a hammer and mechanically ground in a Glen Creston silicon carbide rotary grinder.

3.3. MICROWAVE HEATING OF HYDROTHERMALLY PROCESSED MATERIALS

3.3.1. Hydrothermally co-processed aluminium- and silicon- acetates in solid gel form heated in a domestic- or scientific- microwave oven

The sol produced from hydrothermally co-processing aluminium- and silicon- acetates was dried using the procedure described in Section 3.1.1. 0.5g of the resulting solid gel was heated in an alumina crucible in a domestic or scientific microwave oven for periods of time not exceeding 1 hr.

3.3.2. Hydrothermally co-processed aluminium- and silicon- acetates in liquid gel form heated in a domestic- or scientific- microwave oven

The sol produced from hydrothermally co-processing aluminium- and silicon- acetates was taken to partial dryness using the procedure described in Section 3.1.1. 0.5g of the resulting liquid gel was heated in an alumina crucible in a domestic or scientific microwave oven for periods of time not exceeding 1 hr.

3.3.3. Hydrothermally co-processed aluminium- and silicon- acetates in solid gel form in the presence of iron sulphate in a domestic-or scientific-microwave oven

The sol produced from hydrothermally co-processing aluminium- and silicon- acetates was dried using the procedure described in Section 3.1.1. 0.5g of the resulting solid gel was ground in an agate pestle and mortar with iron sulphate (10 wt%) and heated in an alumina crucible in a domestic or scientific microwave oven for periods of time not exceeding 1 hr.

3.3.4. Hydrothermally co-processed aluminium- and silicon- acetates in liquid gel form in the presence of iron sulphate in a domestic- or scientific-microwave oven

The sol produced from hydrothermally co-processing aluminium- and silicon- acetates was taken to partial dryness using the procedure described in Section 3.1.1. 0.5g of the resulting liquid gel was mixed with iron sulphate (10 wt%) using a glass rod and heated in an alumina crucible in a domestic or scientific microwave oven for periods of time not exceeding 1 hr.

3.4. FREEZE DRYING OF HYDROTHERMALLY PROCESSED MATERIALS

The sol produced from hydrothermally co-processing silicon- and aluminium- acetates was transferred to a 500 ml round bottom flask, frozen in an acetone/ice bath and freeze dried for ca. 48 hrs. The resulting material was calcined using the procedure described in Section 3.1.1.

3.5. RECORDING OF X-RAY DIFFRACTION PATTERNS

3.5.1 Routine measurements

Routine x ray powder diffraction patterns used typically for phase identification purposes were recorded using a 1s/°2θ scan time and a step size of 0.02°2θ.

3.5.2 Special measurements

Special x-ray powder diffraction patterns to be used to produce accurate peak positions for the calculation of lattice parameters, were recorded using a 4s/°2θ scan time and a step size of 0.01°2θ. Each pattern was recorded at least three times. In each case a freshly prepared sample from a single batch of material was used. In cases where two peaks in a pattern were not fully resolved or the peaks were somewhat broad, a peak fitting technique

was used to accurately ascertain the positions of such peaks. The PS. Voigt lineshape consistently gave the best fit in all cases. The errors on each parameter calculated varied according to the width and resolution of the peaks in the x-ray powder diffraction pattern. The errors were obtained for each batch of samples by calculating the average of the standard deviation measurements made from the multiple recordings of the samples. Examples of the calculations are given in Appendix A (p166).

3.6. INSTRUMENTATION

3.6.1. Hydrothermal processing

Hydrothermal syntheses were performed in a Berghof laboratory autoclave fitted with a 750 ml PTFE-beaker liner.

3.6.2. Microwave heating

Microwave heating was performed using a Panasonic microwave oven, Model No. NN6450B, and a scientific CEM MDS-81 microwave oven.

3.6.3. Freeze drying

The freeze dried samples were produced using an Edward's Modulyo freeze dryer at ca. 10^{-2} atm. at -60°C.

3.6.4 X-ray powder diffraction

The x-ray powder diffraction patterns were recorded with a Siemens D5000 powder x-ray diffractometer using *CuKα* radiation at ambient temperature.

3.6.5. Mössbauer spectroscopy

^{57}Fe Mössbauer spectra were recorded at 298K using a microprocessor controlled Cryophysics M-102 Mössbauer spectrometer using a ^{57}Co / Rh source. The drive velocity was calibrated with a ^{57}Co / Rh source and iron foil. All the spectra were computer fitted. The ^{57}Fe chemical isomer shifts are quoted relative to metallic iron.

3.6.6. Proton NMR

The proton NMR free induction decay curves were recorded using a Bruker CXP100 ^{1}H NMR machine tuned on polyethyleneoxide (PEO).

3.6.7. MASNMR

A Varian VXR300 spectrometer (SERC National Solid-State NMR Service) was used to obtain high resolution ^{27}Al (78.15 MHz) and ^{29}Si (59.58 MHz) MASNMR spectra at 298K. Rotor spinning frequencies were 11-12 kHz for the former and 3-4 kHz for the latter. ^{27}Al and ^{29}Si chemical shifts are quoted with respect to external $Al(H_2O)_6^{3+}$ and tetramethylsilane respectively: the high frequency positive convention is used throughout. In some cases ^{29}Si CP/MAS was used; contact times were typically 8 ms. Corrections to ^{27}Al chemical shifts due to second order quadrupole effects were not made.

Chapter 4 The Formation of Mullite by Hydrothermal Processing : Results and Discussion

4.1. THE EVOLUTION OF PHASES OBTAINED BY CALCINING HYDROTHERMALLY PROCESSED ALUMINIUM ACETATE

4.1.1. X-ray powder diffraction

X-ray powder diffraction patterns were recorded from aluminium acetate which had been hydrothermally processed, dried, ground, and calcined at 450°C and 1400°C (Figure 13) according to the procedures described in Chapter 3 Section 3.1.1. The x-ray powder diffraction pattern recorded from the sample dried under an infrared lamp (Figure 13(a)), is characteristic of pseudoboehmite.[1] This material has been described as small-crystallite boehmite of composition $\gamma-AlOOH.nH_2O$. It contains intercalated water molecules and like boehmite has an orthorhombic crystal structure. The x-ray powder diffraction pattern recorded from the samples calcined at temperatures up to 450°C were similar. The x-ray powder diffraction pattern recorded from the sample calcined at 450°C (Figure 13(b)) showed the sample to have undergone a phase transformation from pseudoboehmite to a semi-amorphous phase, which can be attributed to $\gamma-Al_2O_3$ and has a spinel type structure. Similar x-ray powder diffraction patterns were recorded after calcination at temperatures up to 1400°C. The x-ray powder diffraction pattern recorded from the sample calcined at 1400°C, (Figure 13(c)) showed a phase transformation from $\gamma-Al_2O_3$ to crystalline $\alpha-Al_2O_3$, which is commonly known as corundum and has a hexagonal crystal structure. These transitions are well known; although other intermediate transitions which have been reported were not observed in this work.[2]

4.1.2. Lattice parameters

The lattice parameters for the orthorhombic pseudoboehmite phase prepared by hydrothermally processing aluminium acetate and drying under an infrared lamp (Figure 13(a)) together with literature values are collected in Table 1. The lattice parameters were recorded using the method described in Section 3.5.2 (p.57).

The lattice parameters are smaller than those of boehmite; the largest difference being observed in the *b* parameter.

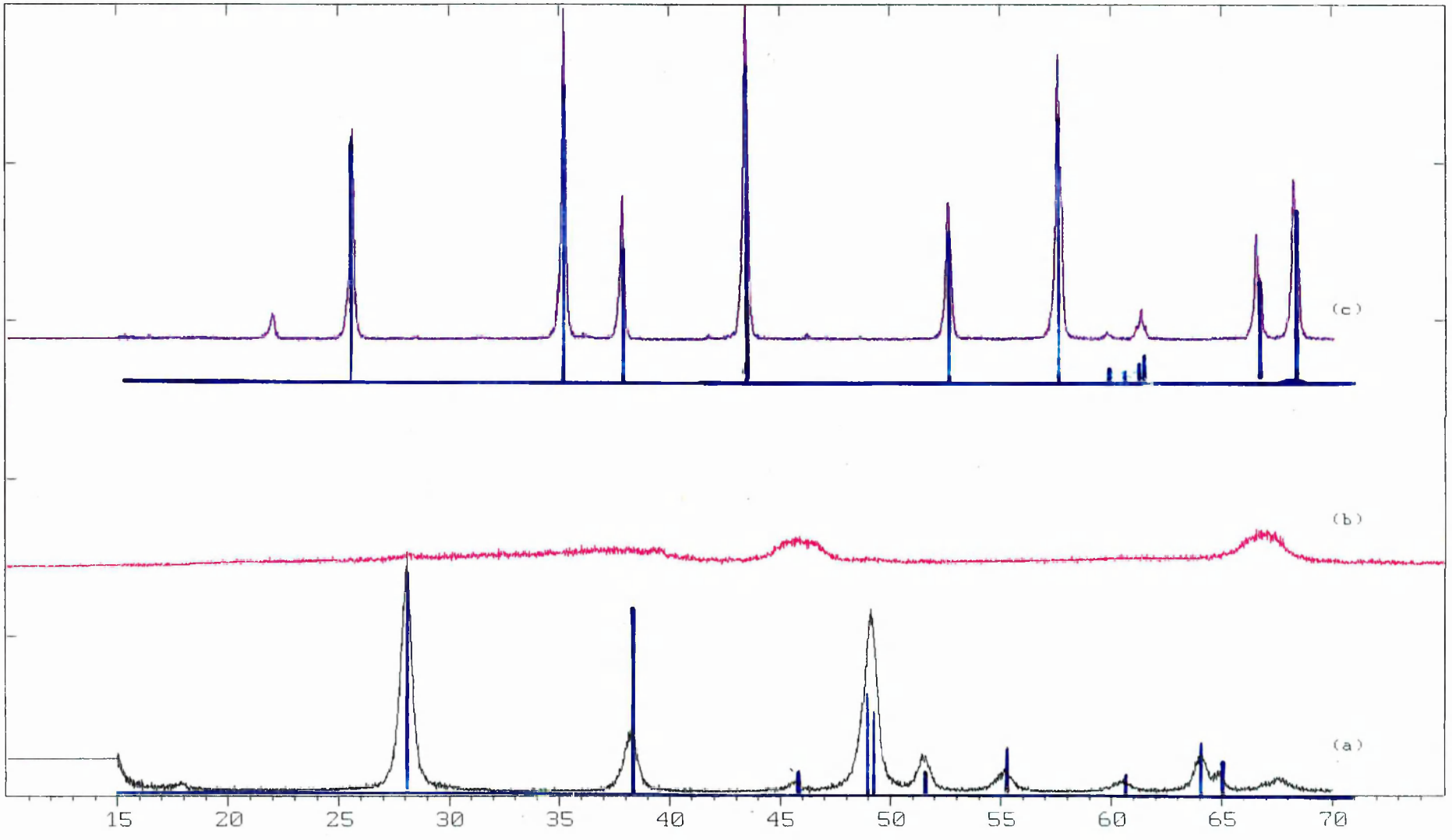

Figure 13. X-ray powder diffraction patterns recorded from hydrothermally processed aluminium acetate (a) dried under an infrared lamp (b) calcined at 450°C (c) calcined at 1400°C. The bar diagrams represent the patterns for: figure (a) boehmite, figure (c) corundum

The acquisition of lattice parameters for the $\gamma - Al_2O_3$ phase obtained by hydrothermally processing aluminium acetate, drying and calcining at 450°C was precluded by the amorphous nature of the material.

The lattice parameters for the hexagonal corundum phase obtained by hydrothermally processing aluminium acetate, drying and calcining at 1400°C are shown in Table 2. The good agreement between experimental and literature values confirms the purity of the sample.

	Lattice Parameters /Å		
Sample History	a±0.005	b±0.015	c±0.005
Pseudoboehmite prepared by drying hydrothermally processed aluminium acetate	3.680	12.176	2.860
Literature values for boehmite[3]	3.700	12.227	2.868

Table 1. Lattice parameters for $\gamma - AlOOH.nH_2O$, pseudoboehmite, formed by drying hydrothermally processed aluminium acetate.

	Lattice Parameters /Å	
Sample History	a±0.002	b±0.002
Corundum prepared by calcining hydrothermally processed aluminium acetate at 1400°C	4.759	12.992
Literature values for corundum [3]	4.758	12.991

Table 2. Lattice parameters for $\alpha - Al_2O_3$, corundum, prepared by calcining hydrothermally processed aluminium acetate at 1400°C.

4.1.3. MASNMR

The ^{27}Al MASNMR spectrum was recorded, with reference to external $Al(H_2O)_6^{3+}$, from hydrothermally processed aluminium acetate (Figure 14) showed a single near-symmetric line at 4.3 $\delta(^{27}Al)$ which is characteristic of aluminium in octahedral coordination and is consistent with the presence of pseudoboehmite as shown by x-ray powder diffraction.

4.1.4. FTIR

The FTIR spectrum (Figure 15) showed peaks which may be associated with the presence of boehmite (Table 3) and is consistent with the results obtained from x-ray powder diffraction and ^{27}Al MASNMR spectroscopy.

4.2. THE EVOLUTION OF PHASES OBTAINED BY CALCINING HYDROTHERMALLY PROCESSED SILICON ACETATE

4.2.1. X-ray powder diffraction

X-ray powder diffraction patterns were recorded from hydrothermally processed silicon acetate which had been dried and ground according to the procedure described in Chapter 3 Section 3.1.1 and then calcined at 1350°C (Figures 16(a) and 16(b)). The x-ray powder diffraction pattern recorded from the sample dried under an infrared lamp (Figure 16(a)) showed an extremely broad single peak with a maximum at 22.5° 2θ which is indicative of the amorphous nature of this material. The position of the observed peak is not inconsistent with the presence of a form of hydrated silica, [56] but evidence from other analytical techniques is required. The x-ray powder diffraction pattern recorded from hydrothermally processed silicon acetate calcined at 1350°C was characteristic of the crystalline form of silica called cristobalite [56] (Figure 16(b)).

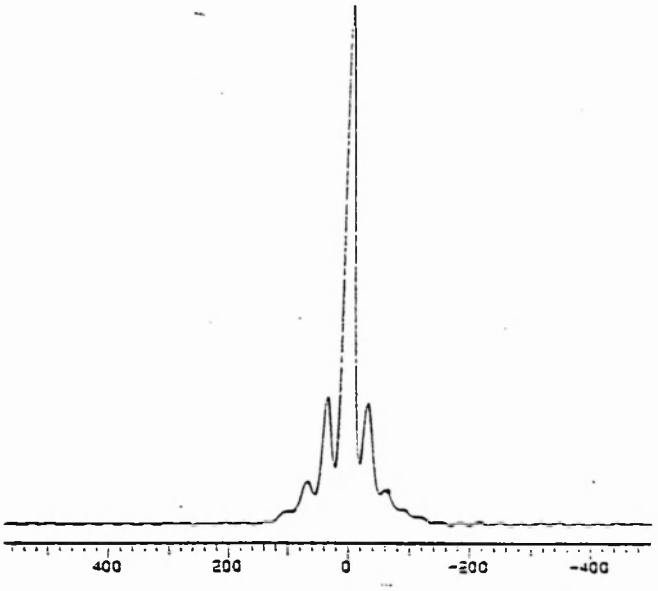

Figure 14. The ^{27}Al MASNMR spectrum recorded from hydrothermally processed aluminium acetate

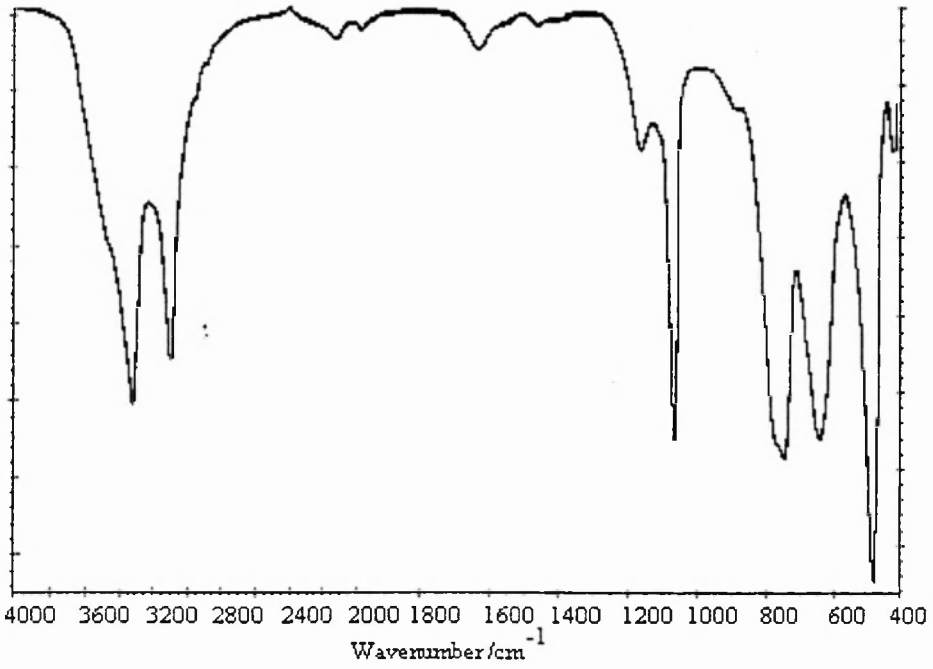

Figure 15. FTIR spectrum recorded from hydrothermally processed aluminium acetate.

PSEUDOBOEHMITE PREPARED BY HYDROTHERMAL PROCESSING /cm^{-1}	BOEHMITE $[4(AlO.OH)]^4$ /cm^{-1}
3305, sp.	3290-45, sp.
3089, sp.	3095-40, sp.
1634, w	1630, w
1159	1160-35, b, sh.
1067, s, sp.	1085-65, s
747, s	760-30, vs.}
639, s	630-05, vs.}
479,s	525-00, vs.}
410	410-00
	372-00
	325

Table 3. FTIR data recorded from pseudoboehmite prepared by hydrothermal processing

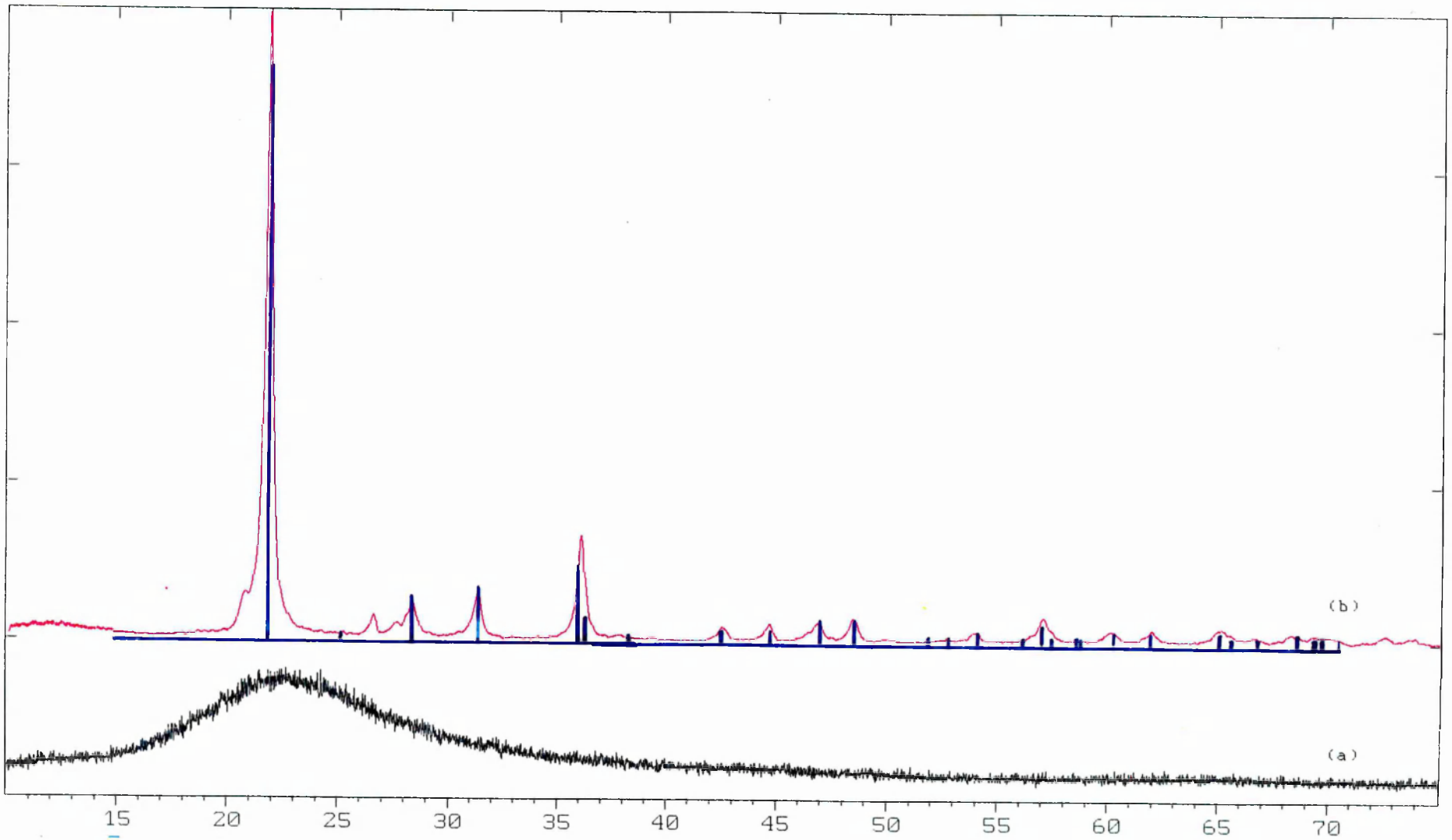

Figure 16. X-ray powder diffraction patterns recorded from hydrothermally processed silicon acetate (a) dried under an infrared lamp (b) calcined at 1350°C. The bar diagram represents the pattern for cristobalite

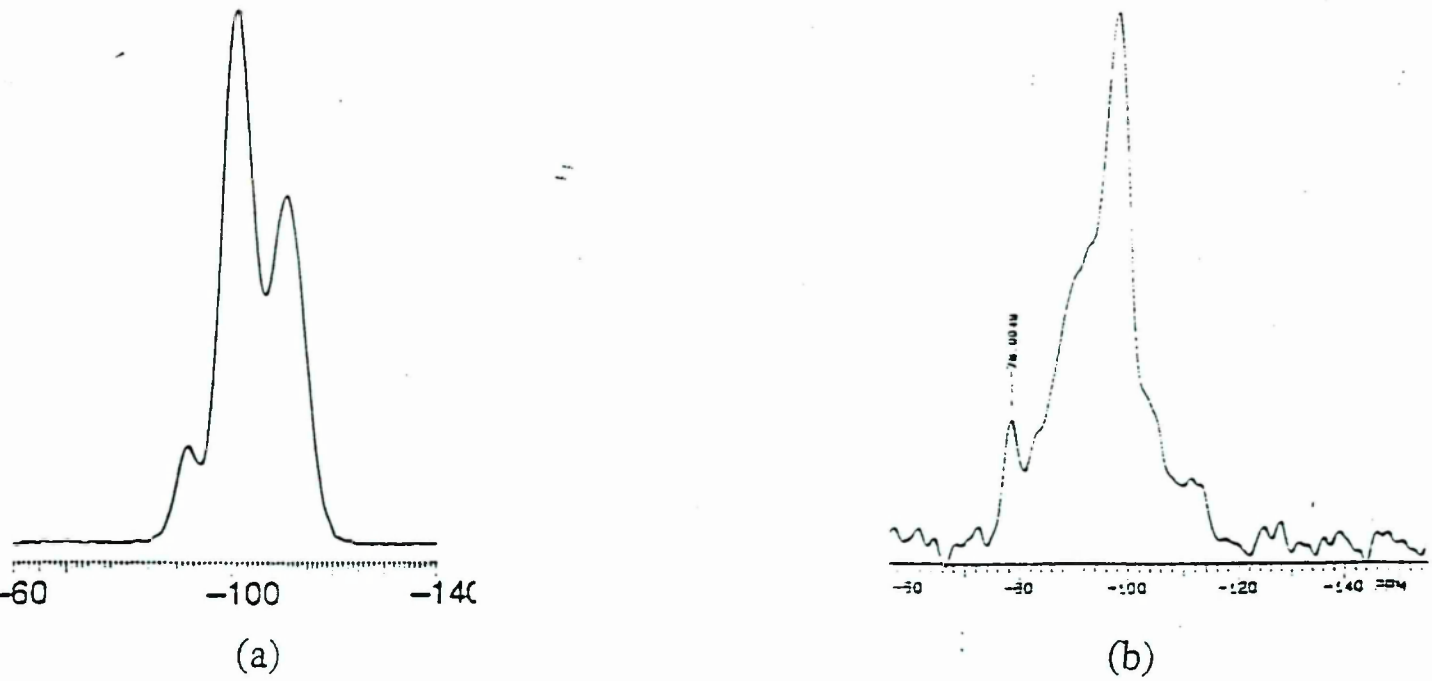

Figure 17. The ^{29}Si MASNMR Spectra recorded from (a) hydrothermally processed silicon acetate (b) hydrothermally processed aluminium- and silicon- acetates

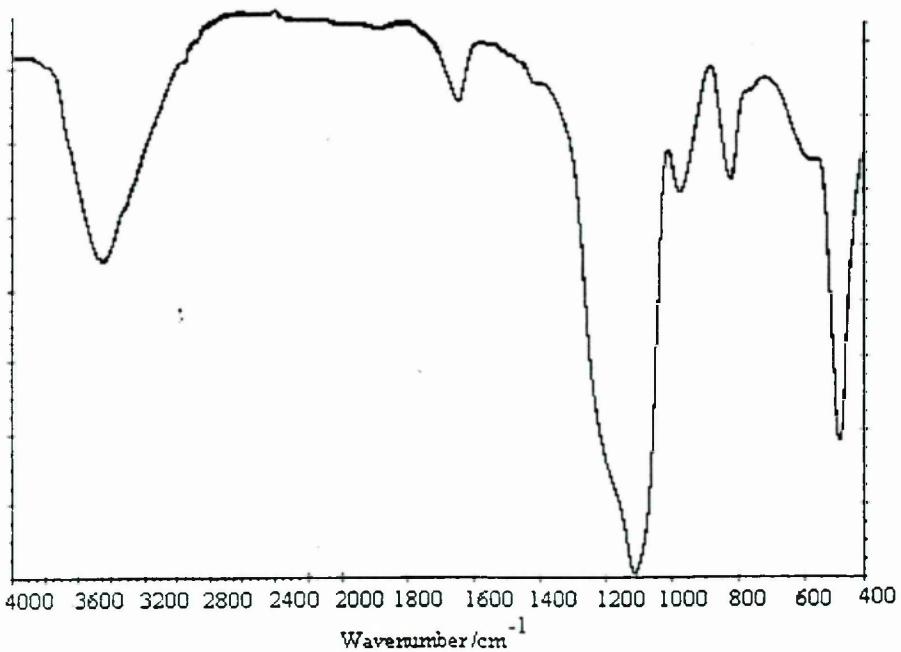

Figure 18. FTIR spectrum recorded from hydrothermally processed silicon acetate.

4.2.2. MASNMR

The ^{29}Si MASNMR spectrum recorded from hydrothermally processed silicon acetate when dried under an infrared lamp (Figure 17(a)) showed three peaks, at -92.1 δ, -101.5 δ and -111.1 δ. These peaks are typical of silanol sites of the form $(SiO)_2Si^*(OH)_2$, $(SiO)_3Si^*(OH)$ and $(SiO)_4Si^*$. These can be expressed using the Q notation described in Section 2.5.3 as Q^2, Q^3 and Q^4 respectively. The spectrum is identical to that recorded from silica gel.[5,6]

4.2.3. FTIR

The FTIR spectrum recorded from hydrothermally processed silicon acetate (Figure 18) was characteristic of a hydrated silica species $SiO_2.nH_2O$. The only classification for this species in the standard FTIR tables is opal; the data are collated in Table 3. This result endorses that obtained from ^{29}Si MASNMR spectroscopy.

4.3. THE EVOLUTION OF PHASES OBTAINED BY CALCINING HYDROTHERMALLY CO-PROCESSED ALUMINIUM- AND SILICON- ACETATES.

Two 5g samples were prepared by hydrothermally co-processing aluminium- and silicon-acetates using the methods described in Chapter 3 Section 3.1.1 One sample had been processed in the presence of HCl whilst the other sample had not. The sample prepared from non-acidified hydrothermally co-processed aluminium- and silicon- acetates was initially split into smaller sized samples. The small samples were calcined at 50°C intervals from 300°C to 1400°C. Samples taken from the material prepared from acidified hydrothermally processing aluminium- and silicon- acetates were also calcined at selected temperatures between 300°C and 1400°C.

4.3.1. X-ray powder diffraction

The x-ray powder diffraction patterns recorded from selected samples prepared under non-acidified conditions are shown in Figure 19((a)-(e)). It is apparent that the main phase transitions occur after calcination at 400°C and 1250°C.

HYDRATED SILICA PREPARED BY HYDROTHERMAL PROCESSING /cm^{-1}	OPAL $SiO_2 \cdot nH_2O$ /cm^{-1}
3432, s, b	3422, s, b
1633, w	1622, w
1385	
1190, inf.	ca 1220, inf.
1102, vs., b	1102-1090, vs., b
800	790-85, s
545	
470, s	476-70

Table 4. FTIR data recorded from hydrated silica prepared by hydrothermal processing

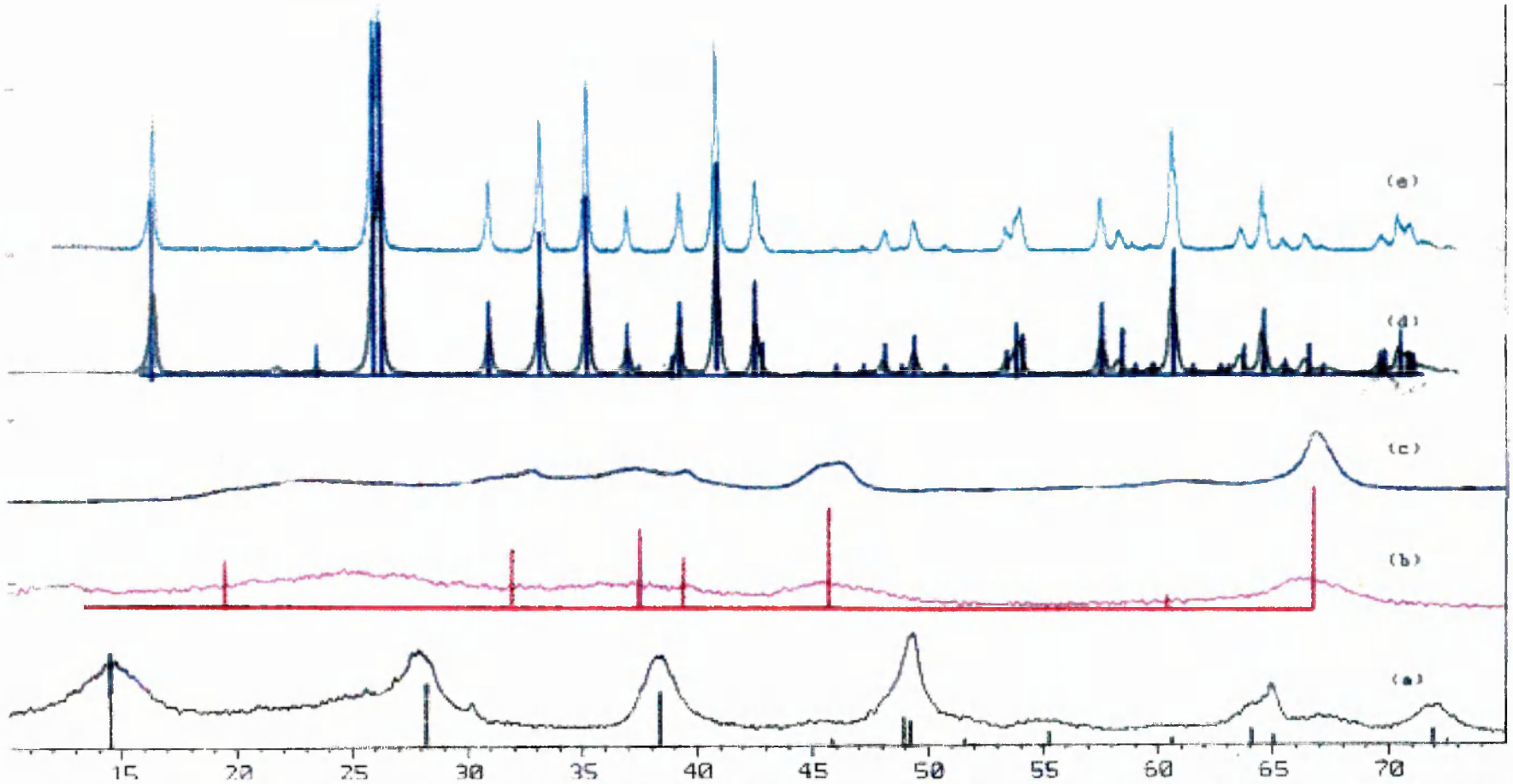

Figure 19. X-ray powder diffraction patterns recorded from hydrothermally co-processed non-acidified aluminium- and silicon- acetates (a) dried under an infrared lamp (b) calcined at 450°C (c) calcined at 1100°C (d) calcined at 1250°C (e) calcined at 1400°C. The bar diagrams represent the patterns for: figure (a) boehmite, figure (b) $\gamma - Al_2O_3$, figure (e) mullite

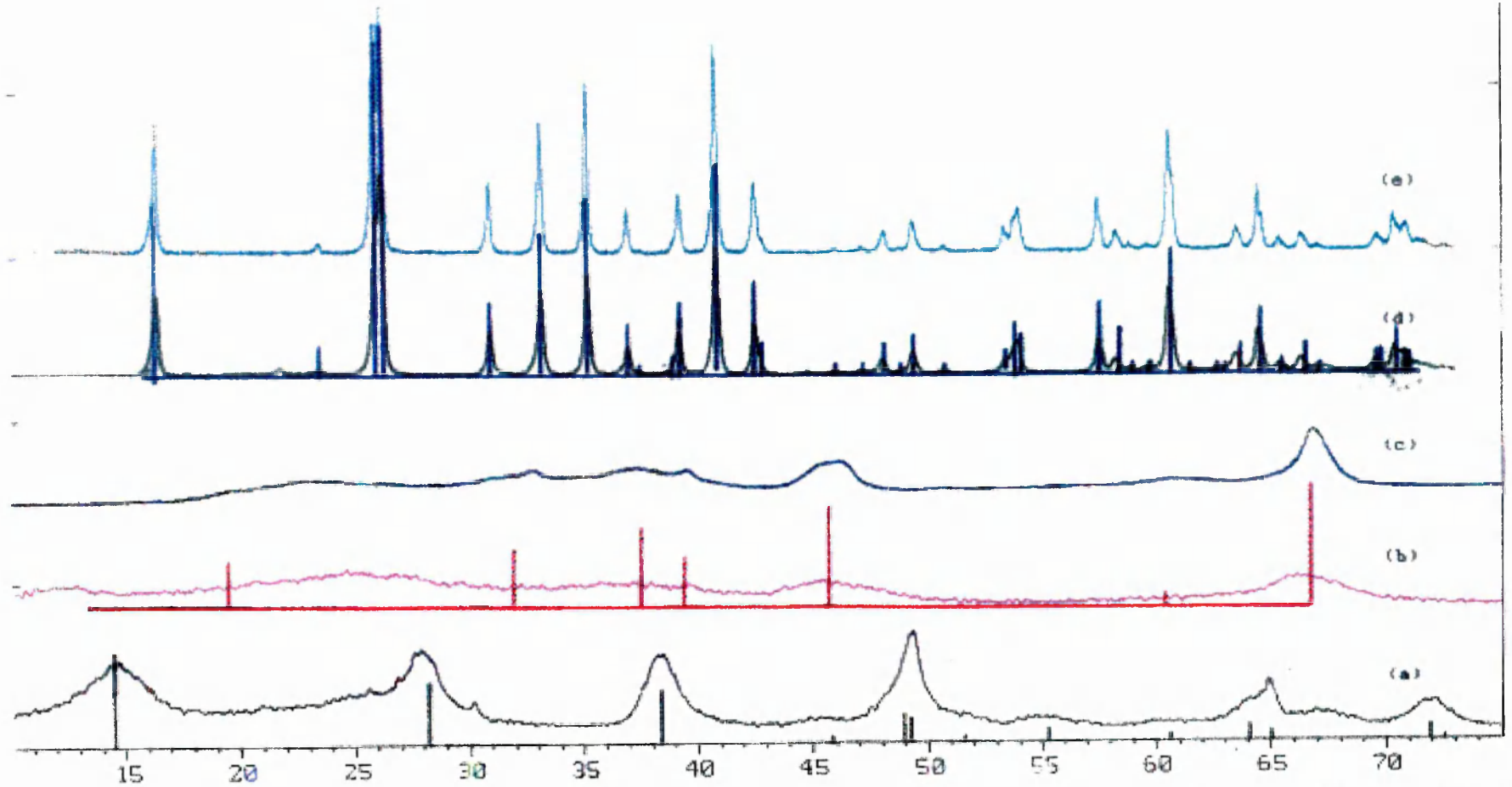

Figure 20. X-ray powder diffraction patterns recorded from hydrothermally co-processed acidified aluminium- and silicon- acetates (a) dried under an infrared lamp (b) calcined at 450°C (c) calcined at 1100°C (d) calcined at 1250°C (e) calcined at 1400°C. The bar diagrams represent the patterns for: figure (a) boehmite, figure (b) $\gamma - Al_2O_3$, figure (d) mullite

The x-ray powder diffraction pattern recorded from hydrothermally co-processed aluminium- and silicon- acetates dried under an infrared lamp was identical to that of the samples which had been calcined up to a temperature of 350°C. The patterns are characteristic of pseudoboehmite. It is however notable that in the x-ray powder diffraction pattern recorded from hydrothermally co-processed silicon- and aluminium- acetates the two reflections which can be indexed as (020) and (120) showed small but significant shifts compared to the x-ray powder diffraction pattern recorded from hydrothermally processed aluminium acetate dried under an infrared lamp. This shifting of peak positions has been quantified by measuring the lattice parameters in each case. The results are given in Table 5.

The x-ray powder diffraction patterns recorded from samples calcined between 400°C and 1200°C all showed a considerable loss of crystallinity compared to pseudoboehmite and are all characteristic of $\gamma-Al_2O_3$; see for example Figure 19(b).

There is a slight crystallisation of the $\gamma-Al_2O_3$ phase with increasing calcination temperature evident by the slight increase in intensity and resolution of the two peaks at ca. 46° 2θ and ca. 67° 2θ in Figure 19(c) compared to Figure 19(b). The absence of a crystalline silicon containing phase in materials heated to these temperatures is notable.

The x-ray powder diffraction patterns recorded from samples calcined at 1250°C and 1400°C are characteristic of mullite (Figures 19(d) and 19(e)). Comparing the x-ray powder diffraction patterns recorded from hydrothermally co-processed aluminium- and silicon- acetates with the x-ray powder diffraction patterns recorded from hydrothermally processed aluminium acetate it is apparent that the pseudoboehmite to $\gamma-Al_2O_3$ phase transition occurs in both materials at the same calcination temperature. This suggests that the presence of silica has little influence on the temperature of the phase transformation.

At higher calcination temperatures the sample prepared from the hydrothermal co-processing of aluminium- and silicon- acetates formed mullite whereas the sample which was prepared from the hydrothermal processing of aluminium acetate formed α-alumina. Hence this difference is the most fundamental effect of the silica.

The x-ray powder diffraction patterns recorded from samples prepared by calcining hydrothermally co-processed acidified aluminium- and silicon- acetates were identical to

those recorded from samples prepared by calcining non-acidified hydrothermally co-processed aluminium- and silicon- acetates (Figures 20(a)-(d)). Further investigation was not pursued. This result indicates that acidification of the precursors does not result in structural difference in the intermediate formed during the formation of mullite.

4.3.2. Lattice parameters

The lattice parameters recorded from the orthorhombic pseudoboehmite phase observed in the x-ray powder diffraction pattern recorded from hydrothermally co-processed non-acidified aluminium- and silicon- acetates which had been dried under an infrared lamp are shown in Table 5. The lattice parameters were recorded using the method described in Section 3.5.2 (p.57).

Sample History	Lattice Parameters /Å		
	a±0.005	b±0.02	c±0.005
Pseudoboehmite prepared by drying hydrothermally co-processed aluminium- and silicon- acetates	3.678	12.134	2.850
Pseudoboehmite prepared by drying hydrothermally processed aluminium acetate	3.680	12.176	2.860
Literature values for boehmite [3]	3.700	12.227	2.868

Table 5. Lattice parameters for pseudoboehmite prepared by drying hydrothermally co-processed aluminium- and silicon- acetates.

The lattice parameters obtained from the pseudoboehmite phase formed by hydrothermally co-processing aluminium- and silicon- acetates were smaller than those obtained from hydrothermally processing aluminium acetate on its own. The most significant change is in the ***b*** parameter which is 0.04Å smaller than that obtained from aluminium acetate hydrothermally processed on its own. The difference between the ***a*** parameters is within the error limits and the difference between the ***c*** parameter is of borderline significance.

The lattice parameters for the orthorhombic mullite phase observed in the x-ray powder diffraction patterns recorded from hydrothermally co-processed aluminium- and silicon-

acetates which had been dried, ground and calcined at 1250°C and 1400°C are shown in Table 6:

Sample History	Lattice Parameters /Å		
	a ±0.01	b ±0.01	c ±0.005
Mullite prepared by calcining hydrothermally co-processed aluminium- and silicon- acetates at 1250°C	7.569	7.696	2.889
Mullite prepared by calcining hydrothermally co-processed aluminium- and silicon- acetates at 1400°C	7.545	7.687	2.882
Literature values for mullite [3]	7.5456	7.6898	2.8842

Table 6. Lattice parameters for mullite prepared by calcining hydrothermally co-processed aluminium- and silicon- acetates at 1250°C and 1400°C

The lattice parameters of the sample calcined at 1250°C are larger than both the literature values and those of mullite prepared by calcining hydrothermally co-processed aluminium- and silicon- acetates at 1400°C. This suggests that the phase formed at 1250°C is a metastable phase which converts to crystalline 3/2 mullite at 1400°C. The lattice parameters for the sample calcined at 1400°C show good agreement with the literature values for mullite.

4.3.3. MASNMR

The ^{27}Al MASNMR spectra recorded, with reference to external $Al(H_2O)_6^{3+}$, from hydrothermally co-processed non-acidified aluminium- and silicon- acetates calcined at different temperatures are shown in Figure 21. In all cases, a low-frequency peak assignable to aluminium in octahedral AlO_6 units was observed which broadened with increasing calcining temperature. A second peak in the 50 ppm region of the spectra was also observed. This region is at the low-frequency end of the range conventionally accepted for aluminium in near-regular tetrahedral AlO_4 units. This second peak was evident in the material calcined at 300°C (Figure 21(a)). The spectrum recorded from the material calcined at 400°C gave two distinct peaks (Figure 21(b)). The peak in the 50 ppm

region of the spectrum had increased in intensity significantly compared to that in the spectrum recorded from the material calcined at 300°C. This would suggest that there is an increase in the amount of aluminium in a tetrahedral environment in this sample.

The spectrum recorded from the material calcined at 600°C (Figure 21(d)) was similar to that expected for γ-alumina,[7] and is therefore consistent with the x-ray powder diffraction information. In other studies[8,9] of the formation of mullite from various precursor materials, a distinct ^{27}Al MASNMR resonance has been observed in the region of 30 ppm for materials calcined at temperatures in the region 600°C - 900°C. This resonance has been assigned to the presence of fivefold coordinated aluminium (AlO_5). Such a resonance was not detected in the present work and this suggests that its presence depends on the method of preparation.

The spectrum of $\frac{3}{2}$ – type mullite (Figure 21(e)) showed three main components and is typical of that described in the literature,[10] although the high-frequency contribution at ca. 60 ppm is present as an unresolved shoulder. At lower MAS rotor frequencies (3 kHz) this peak was resolved although the spectrum was complicated by the presence of spinning sidebands.

The ^{29}Si MASNMR spectrum recorded from hydrothermally processed aluminium- and silicon- acetates is shown in Figure 17(b). This spectrum is noticeably different from that recorded from hydrothermally processed silicon acetate (Figure 17(a)).

There is a general similarity between the two spectra in that they have a main peak at ca. -97 δ (Q^3). However, the spectra differ in two ways; firstly the spectrum recorded from hydrothermally processed aluminium- and silicon- acetates has an unresolved feature to the left of the main peak, whereas the spectrum recorded from hydrothermally processed silicon acetate has a clearly resolved peak at ca. -91 δ. Secondly, the spectrum recorded from hydrothermally co-processed aluminium- and silicon- acetates shows no feature at ca. -110 δ, whereas the spectrum recorded from hydrothermally processed silicon acetate has a peak at ca. -110 δ.

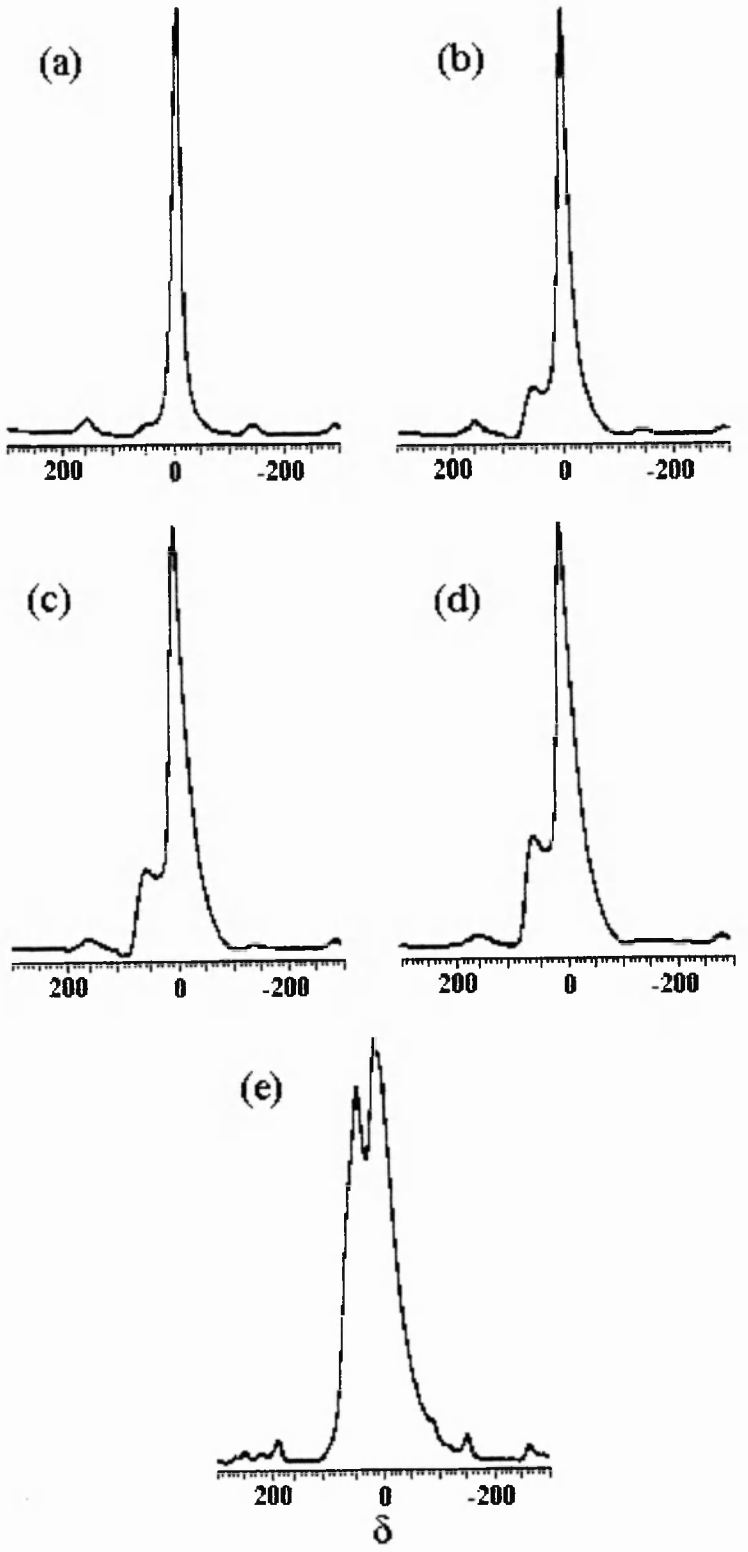

Figure 21. ^{27}Al MASNMR spectra recorded from hydrothermally co-processed aluminium- and silicon- acetates calcined at (a) 300°C, (b) 400 °C, (c) 450°C, (d) 600°C, (e) 1250°C

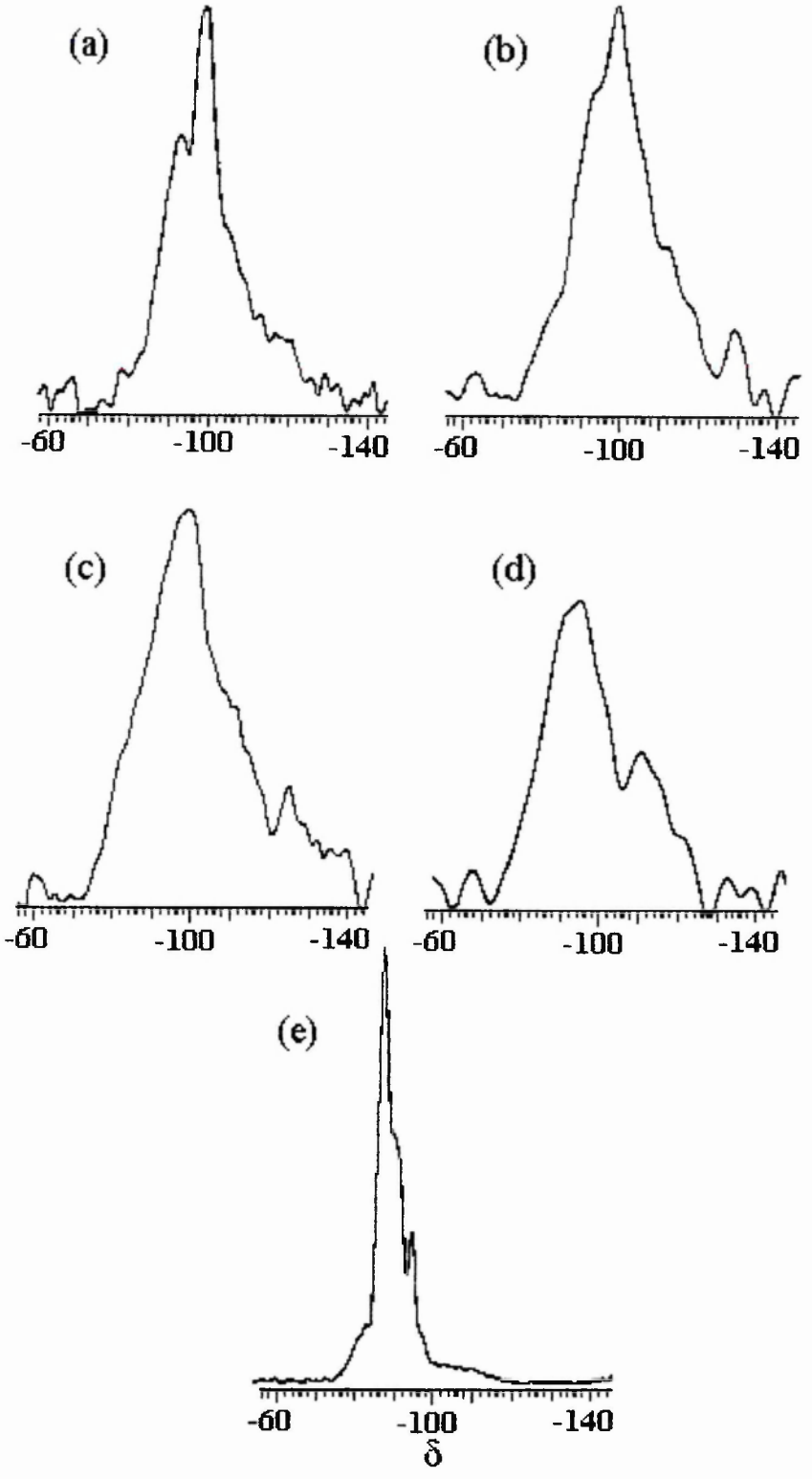

Figure 22. ^{29}Si MASNMR spectra recorded from hydrothermally co-processed aluminium- and silicon- acetates calcined at (a) 300°C, (b) 400 °C, (c) 600°C,(d) 800°C, (e) 1250°C

The spectra recorded from samples of hydrothermally co-processed aluminium- and silicon- acetates after calcination at temperatures between 300°C and 1350°C are shown in Figures 22(a)-(e). The spectra are generally complex and show a broad chemical-shift distribution, presumably due to the presence of a range of distorted SiO_4 units.

All of these spectra show a prominent peak close to -98 δ which is close to the value of the main peak in the spectrum recorded from hydrothermally processed aluminium- and silicon- acetates dried under an infrared lamp (Figure 17(b)). As the calcination temperature increases the spectra show a general trend, in that the feature in the spectrum at around -75 δ fades away. The diminution of the feature in the spectrum at around -75 δ is accompanied by the appearance of an increasingly large feature at ca. -110 δ which becomes partially resolved in the spectrum recorded after calcination at 800°C. Thus the general shape of the spectra become increasingly similar to the shape of the spectrum recorded from the sample calcined at 1250°C, which is typical of mullite.[11]

The results presented in Sections 4.1.-4.3. indicate that the hydrothermal co-processing of aluminium- and silicon- acetates produce solids with different properties than would be anticipated from a mixture of silicon acetate and aluminium acetate hydrothermally processed separately.

This is apparent by:

- The change in the lattice parameters calculated from x-ray powder diffraction data
- The small partially resolved peak in the ^{27}Al MASNMR spectra
- The complex nature of the ^{29}Si MASNMR spectra

4.3.4. FTIR

The FTIR spectrum recorded from hydrothermally co-processed aluminium- and silicon- acetates is shown in Figure 23. The spectrum is more similar to that recorded from hydrothermally processed aluminium acetate (Figure 15) than to the spectrum recorded from hydrothermally processed silicon acetate (Figure 18). The effect of the silicon appears to be to broaden the peaks in the doublet at ca. 3300 cm^{-1} and ca. 3090 cm^{-1} and the triplet below 800 cm^{-1}. It is not clear from this spectrum whether the aluminium-and silicon- phases have formed a simple mixture or are interacting in some way.

The FTIR spectrum recorded from hydrothermally co-processed aluminium- and silicon-acetates calcined at 1400°C is shown in Figure 24. The spectrum is almost featureless between 3000 cm^{-1} and 1200 cm^{-1} which is consistent with mullite being used as a mid-range infrared window, (Chapter 1 Section 1.2.2.).

4.4. THE PARTICLE SIZE OF MULLITE

Transmission electron microscopy (TEM) was performed to examine the particle size of hydrothermally co-processed aluminium- and silicon- acetates and mullite (prepared by calcining the hydrothermally co-processed silicon- and aluminium- acetates at 1400°C.) The micrographs and electron diffraction patterns are shown in Figure 25 and Figure 26 respectively.

The micrograph recorded from hydrothermally co-processed aluminium- and silicon-acetates dried under an infrared lamp (Figure 25(a)) shows the presence of small semi-amorphous platelets (<20 nm) which are clustered together. The edges of the platelets are indistinct which is consistent with the amorphous nature of the material. The intimate contact of the particles may explain why mullite can be prepared hydrothermally at a lower temperature than is possible using conventional methods of preparation. Figure 25(b) shows the electron diffraction pattern recorded from hydrothermally co-processed aluminium- and silicon- acetates. The diffuse rings are attributable to the copper grid on which the sample is supported whilst the faint dots located on the perimeter of the rings can be correlated with the semi-crystalline pseudoboehmite phase.

The micrograph recorded from mullite, prepared by calcining hydrothermally co-processed aluminium- and silicon- acetates at 1400°C (Figure 26(a)), shows the presence of larger crystalline platelets (50-100 nm). The range of particle sizes among the crystals is still small and the crystals are generally uniform in nature. The micrograph recorded from the mullite sample also shows the presence of parallel Moiré patterns in some cases where the platelets overlap. Moiré patterns are produced when two crystals which have different lattice parameters or orientation, overlap.

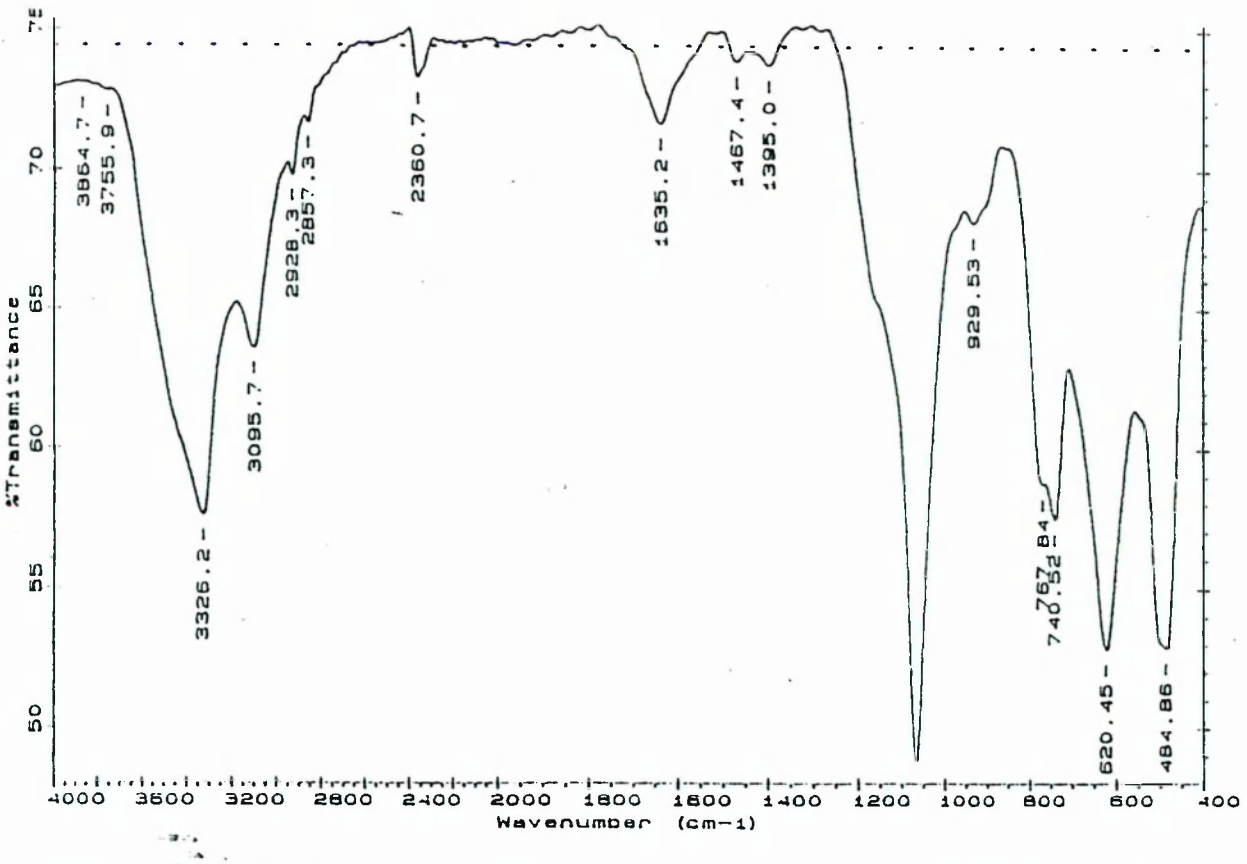

Figure 23. FTIR spectrum recorded from hydrothermally co-processed aluminium- and silicon- acetates dried under an infrared lamp.

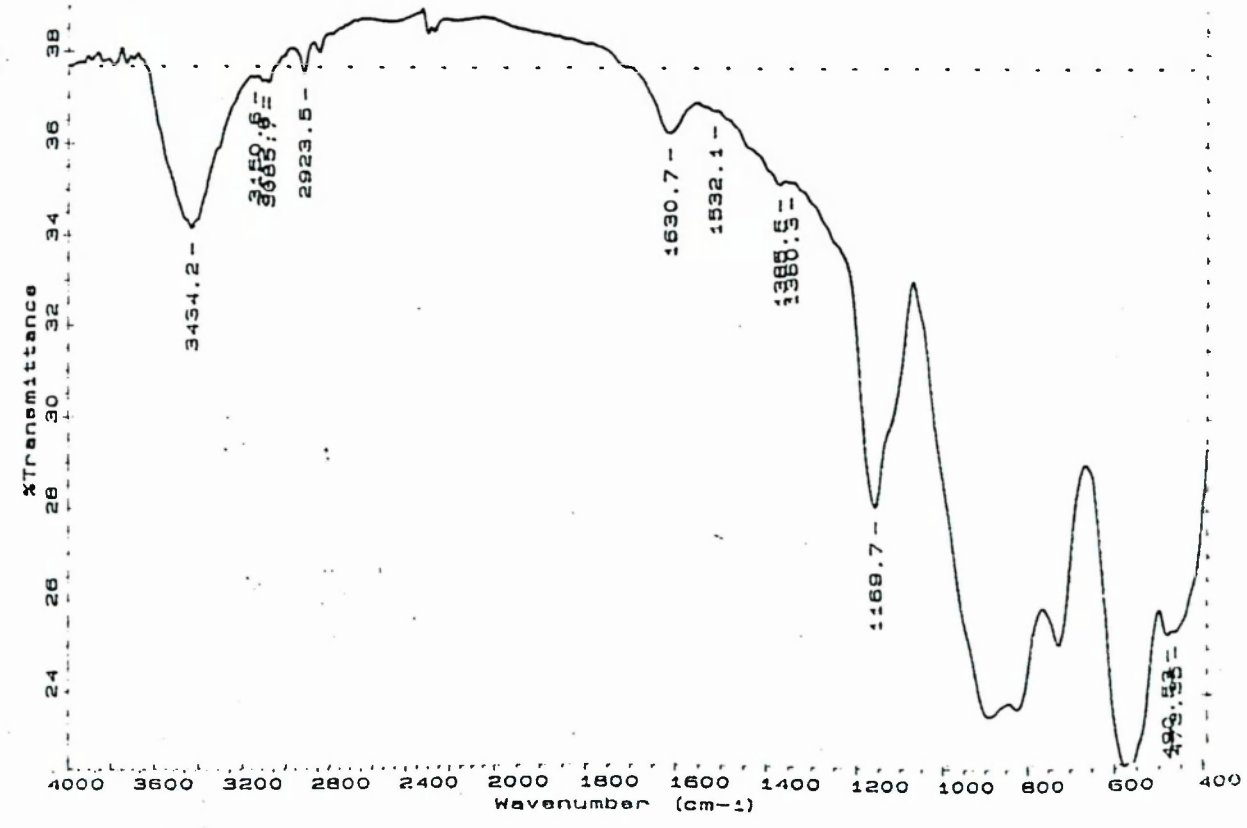

Figure 24. FTIR spectrum recorded from hydrothermally co-processed aluminium- and silicon- acetates calcined at 1400°C.

(a)

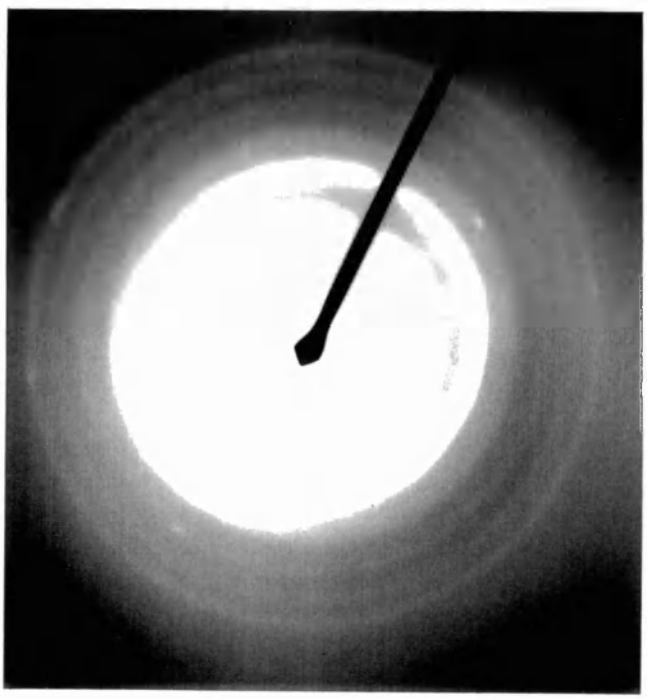

(b)

Figure 25. (a) Transmission electron micrograph of hydrothermally co-processed aluminium- and silicon- acetates dried under an infrared lamp (b) Electron diffraction pattern recorded from hydrothermally co-processed aluminium- and silicon- acetates dried under an infrared lamp

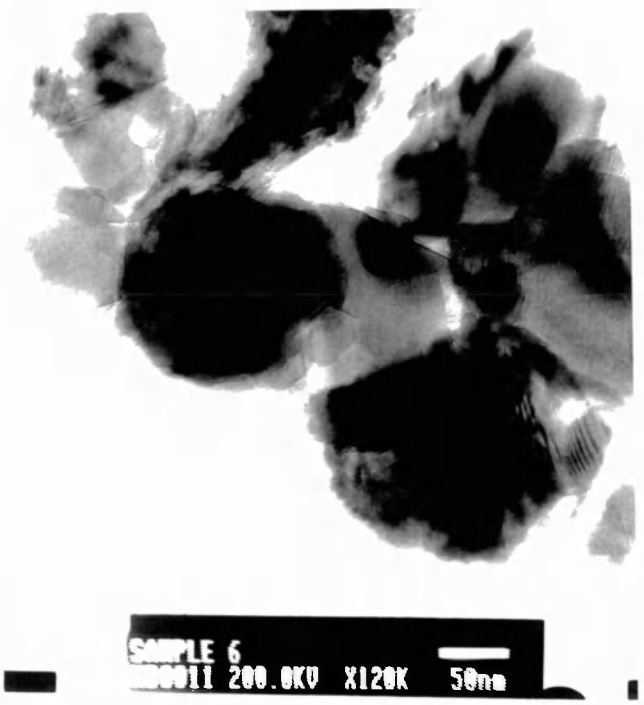

(a)

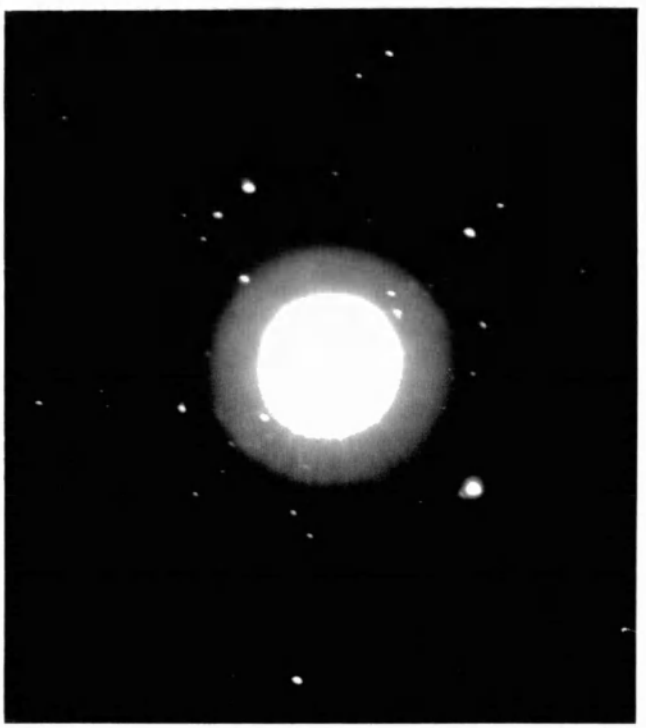

(b)

Figure 26. (a) Transmission electron micrograph of hydrothermally co-processed aluminium- and silicon- acetates calcined at 1400°C (b) Electron diffraction pattern recorded from hydrothermally co-processed aluminium- and silicon- acetates calcined at 1400°C

The presence of parallel Moiré patterns in the mullite samples is likely to indicate that two thin platelet crystals, with slightly different orientation are overlapping and producing constructive interference. Figure 26(b) shows the electron diffraction pattern recorded from aluminium- and silicon- acetates hydrothermally processed and calcined at 1400°C. This diffraction pattern can be attributed to the presence of crystalline mullite although the overlaying of the crystals precluded indexing of the pattern.

4.5. THE FORMATION OF MULLITE FROM KAOLINITE

In order to compare the nature of mullite reported here with that prepared by a conventional method, mullite was prepared from kaolinite, which is a readily available material and is relatively inexpensive. The x-ray powder diffraction pattern recorded from the kaolinite powder is shown in Figure 27(a).

X-ray powder diffraction patterns were recorded from kaolinite following calcination at 500°C, 980°C and 1250°C and are shown in Figures 27(b)-(d). The pattern recorded from the untreated sample is characteristic of crystalline kaolinite. The patterns recorded from the samples calcined at 500°C and 980°C are very similar to each other and show the material to be amorphous.

Studies by differential thermal analysis[11] have shown an exothermic peak at 980°C which was attributed to the formation of an intermediate phase. However this intermediate phase was reportedly disordered and not amenable to identification by x-ray powder diffraction. The results presented here confirm that the nature of the intermediate phase is amorphous and cannot be identified by x-ray powder diffraction.

The x-ray diffraction pattern recorded from the sample calcined at 1250°C was assigned to a poorly crystalline mullite phase. The large peak at ca. 25° 2θ is attributable to a form of SiO_2. The results show that at the same temperature at which pure mullite is formed by hydrothermal synthesis, only an impure, partially crystalline mullite can be formed from the direct calcination of kaolinite. The results confirm that the calcination of hydrothermally processed sols is a superior method of preparing mullite.

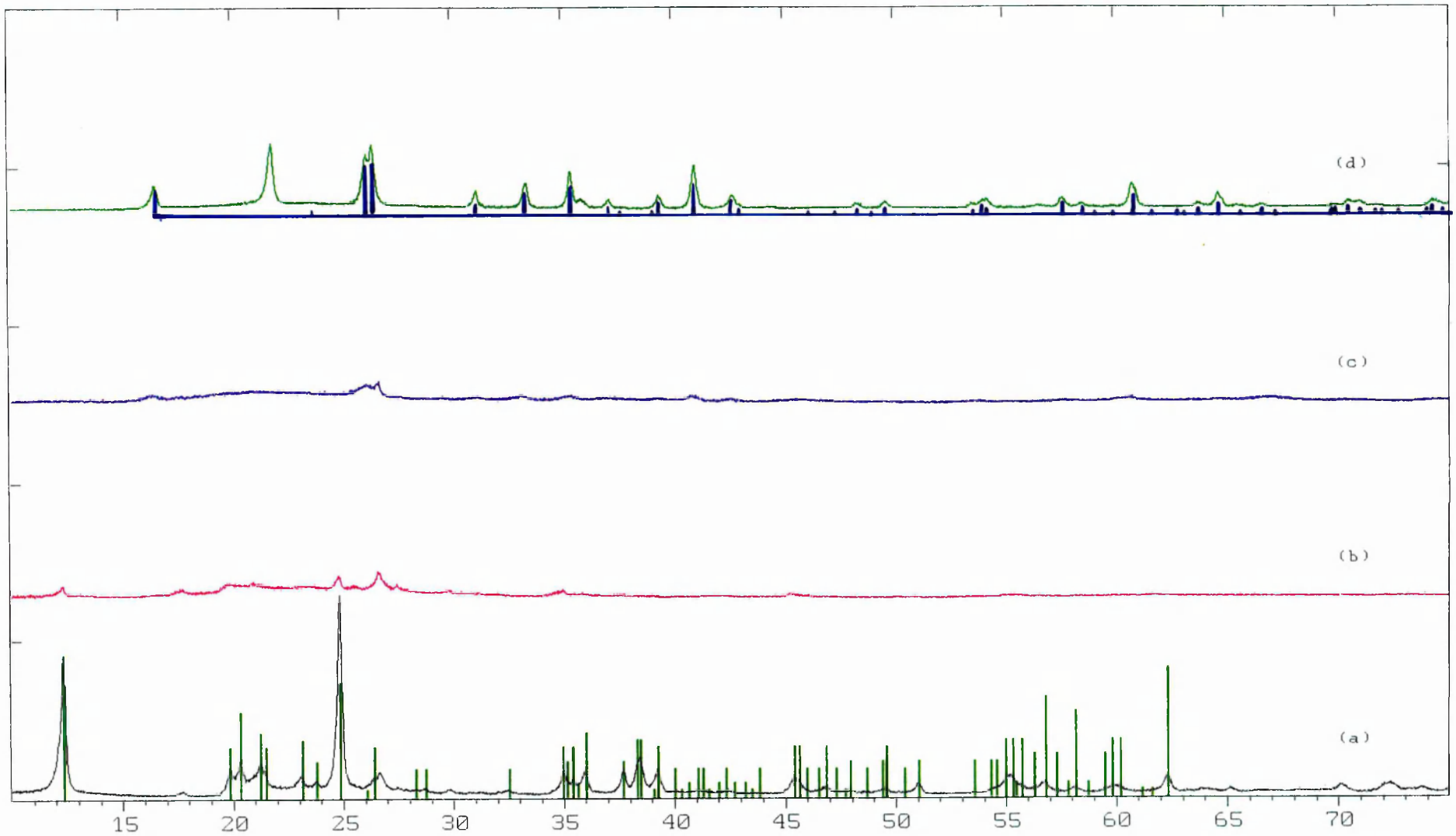

Figure 27. X-ray powder diffraction patterns for kaolinite (a) from bottle (b) calcined at 500°C (c) calcined at 980°C (d) calcined at 1250°C

The bar diagrams represent the patterns for: figure (a) kaolinite, figure (b) mullite.

4.6. THE EFFECT OF FREEZE DRYING THE SOL PRODUCED BY HYDROTHERMALLY CO-PROCESSING ALUMINIUM- AND SILICON- ACETATES.

The rate limiting step in mullite formation using the hydrothermal processing route described in this work is the drying of the sol produced. The use of the infrared lamp and hotplate also results in some agglomeration.

Although these agglomerates are 'soft' and can be easily broken, their formation is not ideal. A method which avoids the formation of agglomerates and takes similar or less time could be beneficial. A sol produced from hydrothermally co-processed non-acidified aluminium- and silicon- acetates was transferred to a round bottom flask, placed into an acetone/ice bath and rotated by hand such that the maximum internal surface area of the flask was covered. The flask was then placed on a freeze dryer for 48 hours.

The resulting powder did not need grinding, indeed the nature of the particles was such that the particles had strong repulsion for each other and could not be contained in the normal size container used for the quantity of material which had been processed. X-ray powder diffraction patterns were recorded from samples of the resulting powder which had been calcined at 1150°C, 1250°C 1350°C and 1400°C. The pattern shown in Figure 28(a) was recorded from the pre-calcined powder, and is characteristic of pseudoboehmite.

The pattern recorded from the sample calcined at 1150°C shown in Figure 28(b) is characteristic of $\gamma - Al_2O_3$.

The results indicate that the phase evolution of samples prepared by calcining freeze-dried hydrothermally co-processed aluminium- and silicon- acetates is identical to that obtained by calcining hydrothermally co-processed aluminium- and silicon- acetates, dried in the standard way (Section 4.3.). The pattern recorded from the sample calcined at 1250°C, (Figure 28(c)), is characteristic of a mullite which, although pure, is only partially crystalline. The pattern recorded from the sample calcined at 1350°C, (Figure 28(d)), is characteristic of crystalline mullite and is identical to the pattern recorded from the sample calcined at 1400°C, (Figure 28(e)).

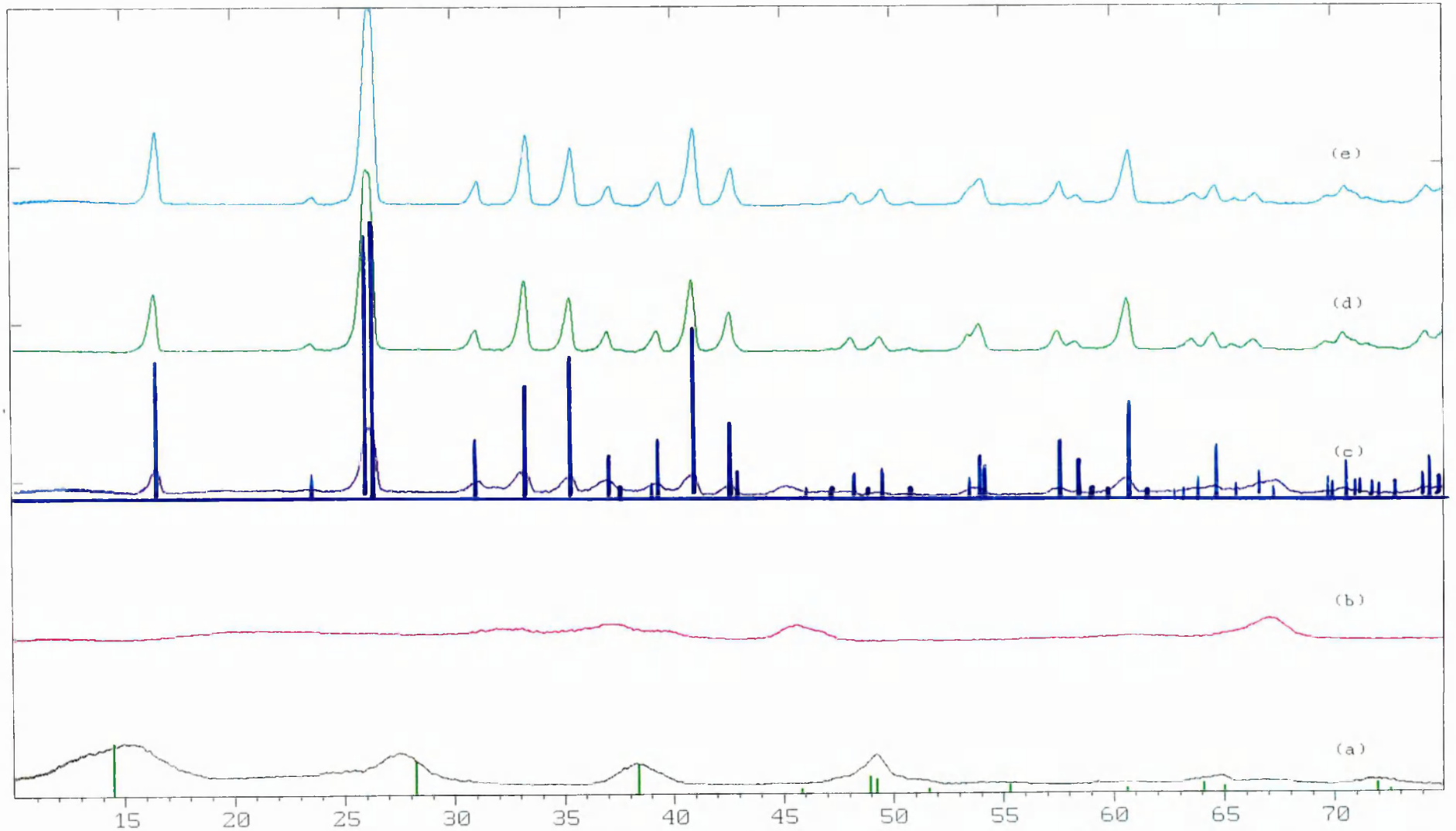

Figure 28. X-ray powder diffraction patterns recorded from freeze-dried non-acidified hydrothermally co-processed aluminium- and silicon-acetates (a) dried under an infrared lamp (b) calcined at 1150°C (c) calcined at 1250°C (d) calcined at 1350°C (e) calcined at 1400°C. The bar diagrams represent the patterns for: figure (a) boehmite, figure (c) mullite

These results indicate that mullite is formed at a higher temperature when the sol resulting from the hydrothermal co-processing of aluminium- and silicon- acetates was freeze dried. Taken together the results show that the hydrothermal co-processing of aluminium- and silicon- acetates does not give a simple mixture of pseudoboehmite- and silica-gel related phases. It appears that the strong interfacial interaction in the material dried under an infrared lamp have a strong influence on the silicon-containing phase. It is also clear that the development of tetrahedrally coordinated Al occurs at temperatures as low as 300°C. Together with the formation of mullite at a lower temperature than expected, this development may be associated with the intimate interaction between the pseudoboehmite- and silica-gel related phases formed after drying the sol produced in the autoclave.
Therefore, freeze drying is not a suitable method for reducing the time scale of mullite formation.

4.7. THE RESISTANCE OF MULLITE TO ACID

The observation that the crystallinity of mullite increased with increasing calcination temperature (Figure 19) and the variation in the lattice parameters for mullite (Section 4.3.2.) suggests that mullite may pass through a metastable state, where not all of the characteristic properties of mullite are present.

One of the advantageous properties of mullite described in Chapter 1 Section 1.2.2. was its resistance to harsh environmental conditions. The stability to acid of two samples of hydrothermally processed mullite; one calcined at 1250°C and the other calcined at 1400°C, were tested against a sample of ground mullite tubing. The treatment in acid was performed according to the procedure described in Section 3.2. The x-ray powder diffraction pattern recorded from the sample of hydrothermally processed mullite calcined at 1250°C washed once in acid (Figure 29(a)) showed a large reduction in the intensity of the mullite phase. There was a significant increase in the background intensity of this pattern which suggested that an amorphous phase was being formed. This amorphous phase is likely to be SiO_2 resulting from the breakdown of the mullite. The aluminium-containing phase which would also be expected appears to be soluble in acid and is

removed in the washings. Since $\alpha - Al_2O_3$ is only very slightly soluble in acid[12] it is likely that some other aluminium containing phase which is soluble in acid is being formed.

The x-ray powder diffraction pattern recorded after the second washing of this sample (Figure 29(b)) showed an almost complete loss of any crystalline phase, except for one peak at ca. 22° 2θ which is unassignable.

The x-ray powder diffraction pattern recorded from the sample of hydrothermally co-processed aluminium- and silicon- acetates calcined at 1400°C (Figure 30(a)) washed once in acid showed the mullite phase to be more resistant to acid. This resistance was identifiable firstly by most of the peaks characteristic of the mullite phase being resolved and secondly by the intensity of the amorphous peak characteristic of silica being much lower than that previously observed in the x-ray pattern recorded from the sample of hydrothermally co-processed aluminium- and silicon- acetates calcined at 1250°C, after one washing in acid. There is also a second phase observable in the x-ray powder diffraction pattern recorded from the acid washed sample of hydrothermally co-processed aluminium- and silicon- acetates calcined at 1400°C, which is attributable to $AlCl_3 \cdot 6H_2O$. The presence of this material is somewhat surprising but would appear to result from the chloride ions in the HCl reacting with the aluminium-containing product formed from the breakdown of the mullite.

This $AlCl_3 \cdot 6H_2O$ phase would also appear to be the cause of a yellow colouration often observed in the reaction vessel. The washings obtained from the samples were also yellow, and when the combined washings were taken to dryness using rotary evaporation, the resulting powder gave an x-ray powder diffraction pattern which was characteristic of $AlCl_3 \cdot 6H_2O$. The presence of the $AlCl_3 \cdot 6H_2O$ is only observed in powder x-ray diffraction patterns where a substantial mullite phase is also present, which may suggest that the $AlCl_3 \cdot 6H_2O$ is coating the mullite particles. When the mullite phase breaks down significantly the $AlCl_3 \cdot 6H_2O$ is no longer able to coat the mullite particles and is lost into the washings. The x-ray powder diffraction patterns recorded from subsequent acid washings of the sample of hydrothermally co-processed aluminium- and silicon- acetates calcined at 1400°C showed almost complete breakdown of the mullite and the loss of nearly all crystallinity (Figures 30(b) and 30(c)).

The x-ray powder diffraction pattern recorded from the acid washed mullite tubing (Figure 31(a)) showed no significant change from the x-ray powder diffraction pattern recorded from the unwashed tube. The x-ray diffraction patterns recorded from subsequent acid washings of the sample obtained from mullite tubing also showed no significant change from the starting material (Figure 31(b)).

The results show that finely ground, high surface area, samples of mullite prepared by hydrothermal processing break down under very harsh acidic conditions.

The hydrothermally processed mullite sample calcined at the higher temperature showed significantly better resistance after one acid washing, but did break down after two washings. The commercial mullite tubing showed no obvious signs of being affected by the acid, but it may well have been mechanically hardened during its processing.

4.8. THE EFFECT OF HYDROTHERMALLY PROCESSING SILICON ACETATE AT VARYING pH

The effect of acidifying mullite precursor sols has been reported[13] to cause small increases in the densification of samples prepared in the presence of HCl, compared to samples prepared in the absence of HCl. This observation was explained in terms of the H^+ and Cl^- ions affecting the surface charge of the composite sol particles.

By processing silicon acetate at varying pH it should be possible to establish whether the higher rate of densification achieved by acidification of the sol is a purely physical effect or whether there is a chemical effect as well. If there is a chemical effect then a difference in the x-ray powder diffraction patterns recorded would be expected. Dried powder samples were prepared by the methods described in Chapter 3 Section 3.1.1 The x-ray powder diffraction patterns recorded from the hydrothermal processing of silicon acetate at different pH's are shown in Figure 32. The x-ray powder diffraction patterns recorded from samples prepared by processing at pH 1 to pH 3 (Figure 32(a)-(c)) are identical and show the material to be amorphous. The patterns resemble those recorded from non- acidified hydrothermally processed silicon acetate which had been dried under an infrared lamp (Figure 16(a)).

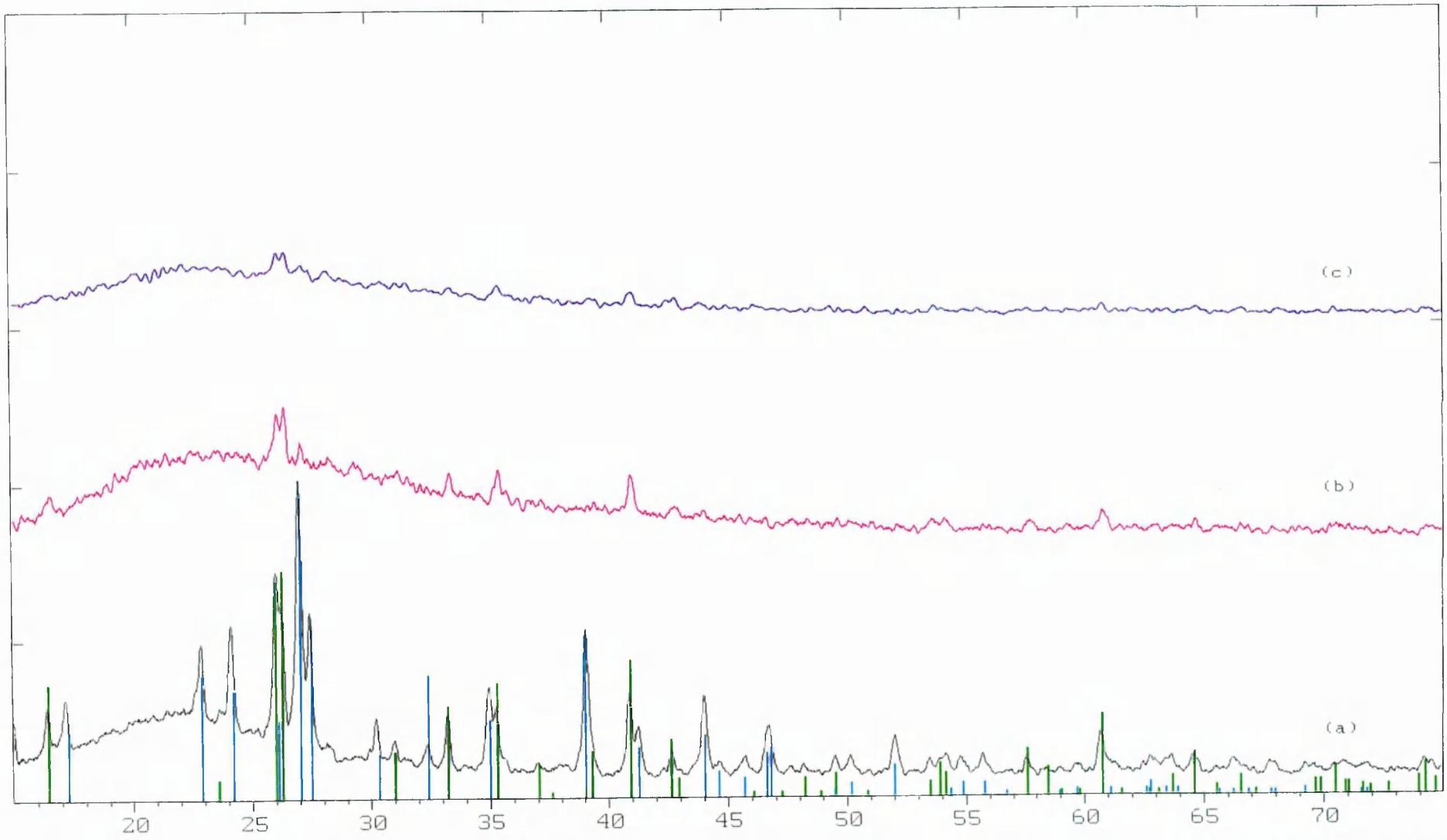

Figure 29. X-ray powder diffraction patterns recorded from acid washed samples of hydrothermally processed mullite calcined at 1250°C (a) after one washing (b) after two washings. The bar diagram represents the pattern for mullite

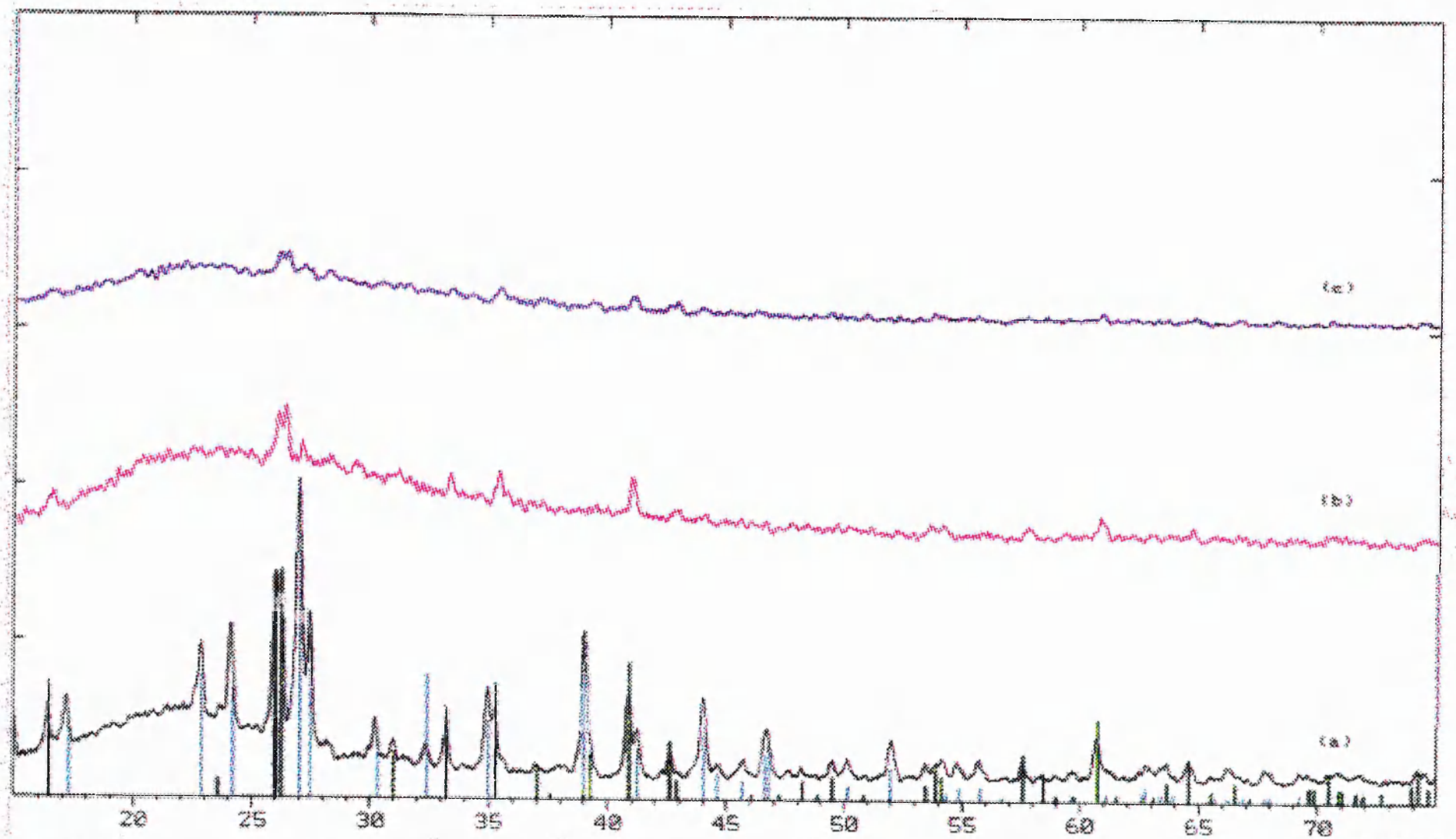

Figure 30. X-ray powder diffraction patterns recorded from acid washed samples of hydrothermally processed mullite calcined at 1400°C (a) after one washing (b) after two washings (c) after three washings. The bar diagrams represent the patterns for mullite and $AlCl_3.6H_2O$

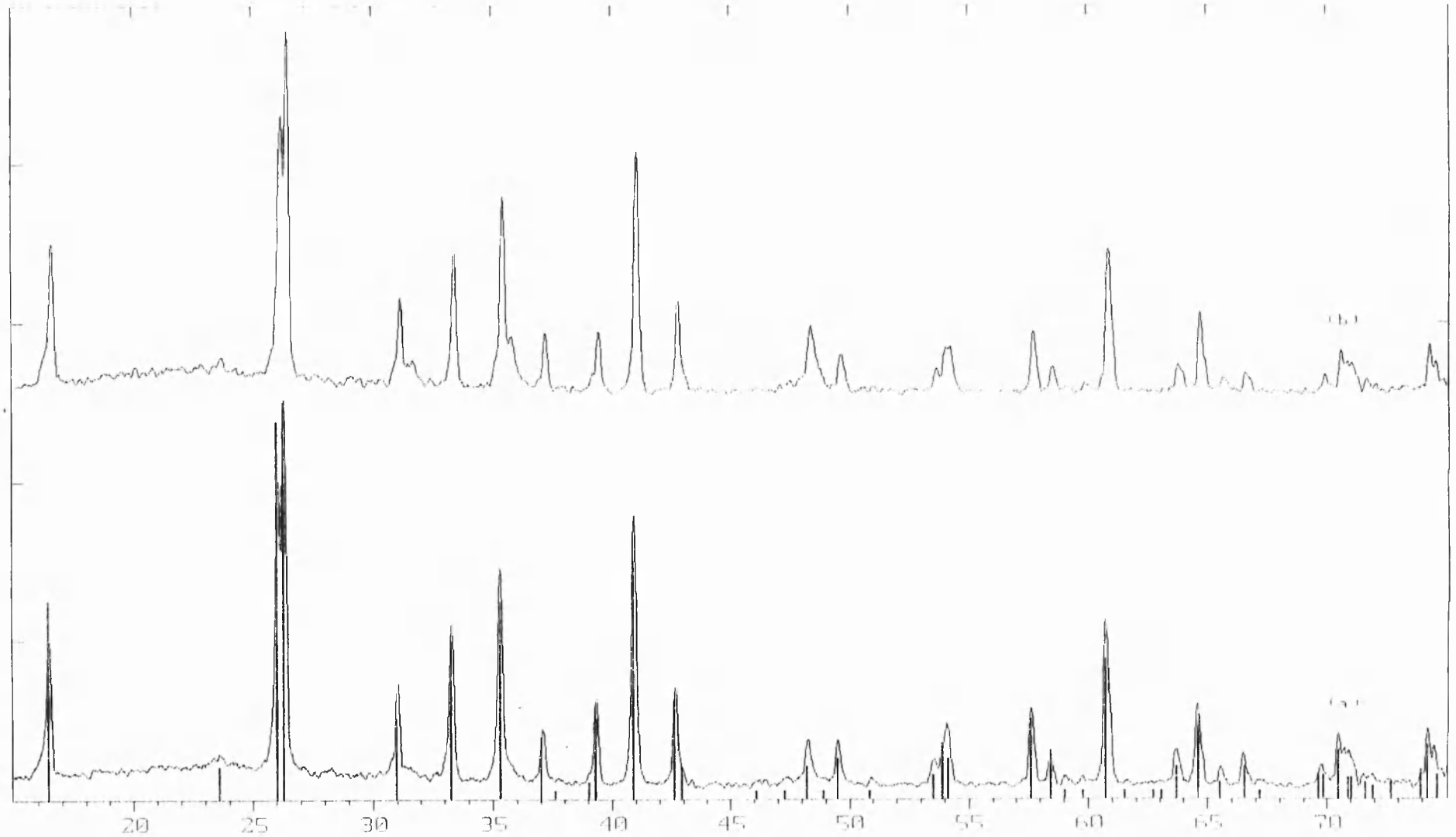

Figure 31. X-ray powder diffraction patterns recorded from acid washed samples obtained from commercial mullite tubing (a) after one washing (b) after two washings. The bar diagram represents the pattern for mullite

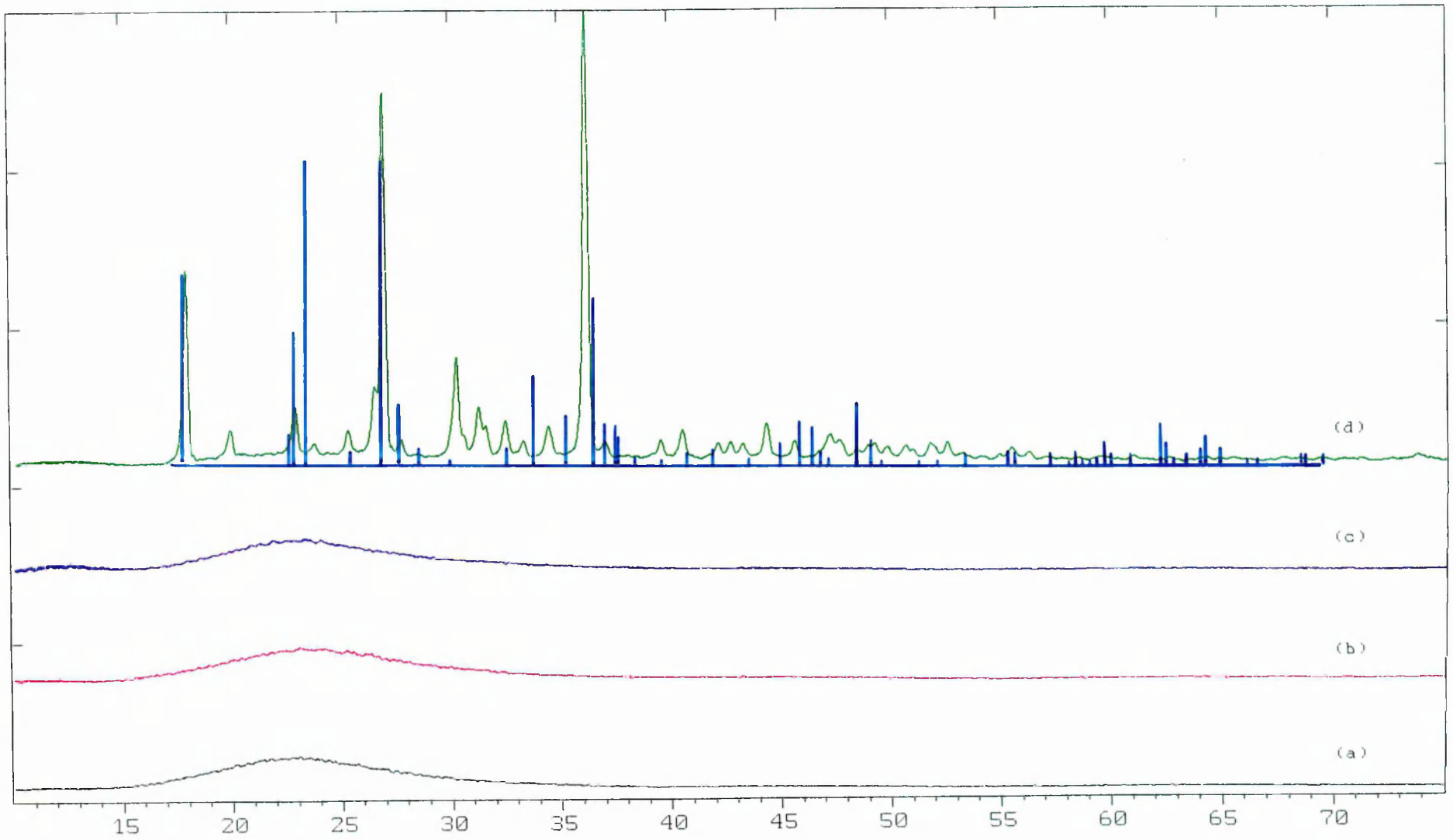

Figure 32. X-ray powder diffraction patterns recorded from silicon acetate suspensions of (a) pH 1, (b) pH 2, (c) pH 3, (d) pH 7, hydrothermally processed. The bar diagram represents the pattern for silicon acetate

The x-ray powder diffraction pattern recorded from the silicon acetate suspension processed at pH 7 however, showed the presence of some sodium-containing phases. Sodium acetate and another phase which could possibly be assigned to sodium silicate appear to be forming from the sodium in the sodium hydroxide, and are formed in preference to acetic acid, which is the usual by-product of this reaction. The presence of sodium in such large amounts is undesirable as it is likely to form an impurity phase during subsequent calcination. The absence of a sodium- containing phase in the silicon acetate suspension processed at pH 3 is presumably because very little sodium hydroxide was required to modify the pH, and hence any sodium acetate formation was below the detection limit of x-ray powder diffraction. The formation of this sodium-containing phase may be quite normal as the hydrothermal processing performed in this work has always been in an acidic pH as acetic acid is a natural by-product of the reaction.

These results indicate that the acidification of silica sols prior to hydrothermal processing results in changes only to the physical properties of the sol and hence materials resulting from it.

4.9. THE PRESENCE OF HYDROGEN-CONTAINING MATERIAL IN MULLITE

4.9.1. The nature of ^{1}H free induction decay with temperature

All the results presented here are qualitative as calibration of the ^{1}H free induction decay was not attempted; that is the relative amount of proton containing material on a mass for mass basis was not determined. This would have been difficult to achieve given that there is a solid component in the free induction decay for which the intense part of the signal is obscured by the NMR probe dead time.

Two sets of samples were prepared. One set was prepared from hydrothermally processed aluminium- and silicon- acetates in the presence of acid, the other set was prepared from hydrothermally processed aluminium- and silicon- acetates with no acid added. Each set of samples was calcined at 500°C and 1250°C.

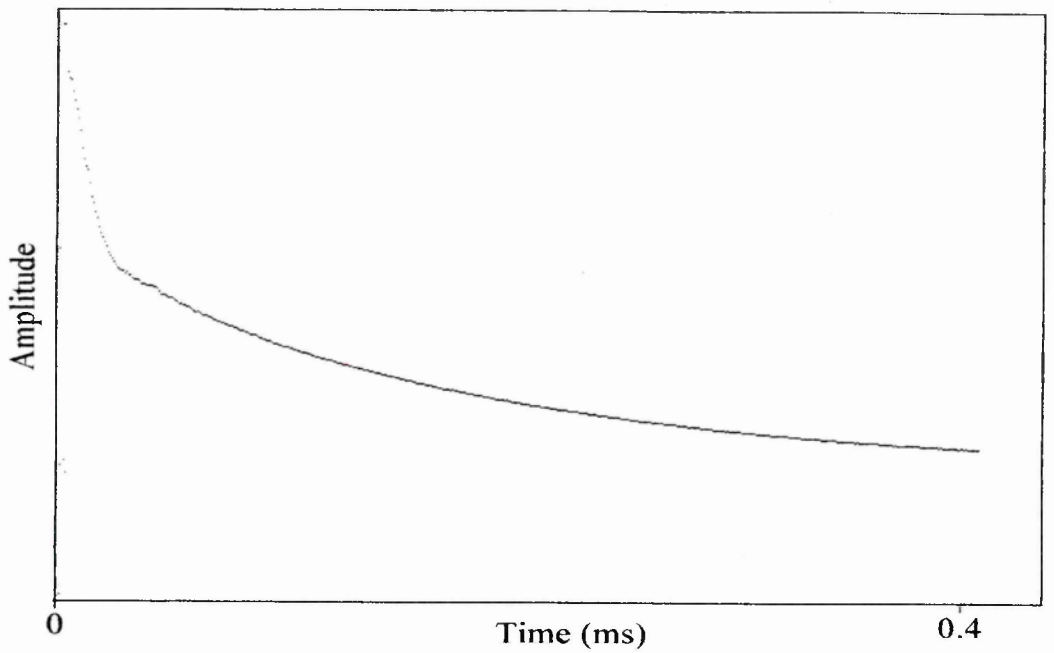

(a)

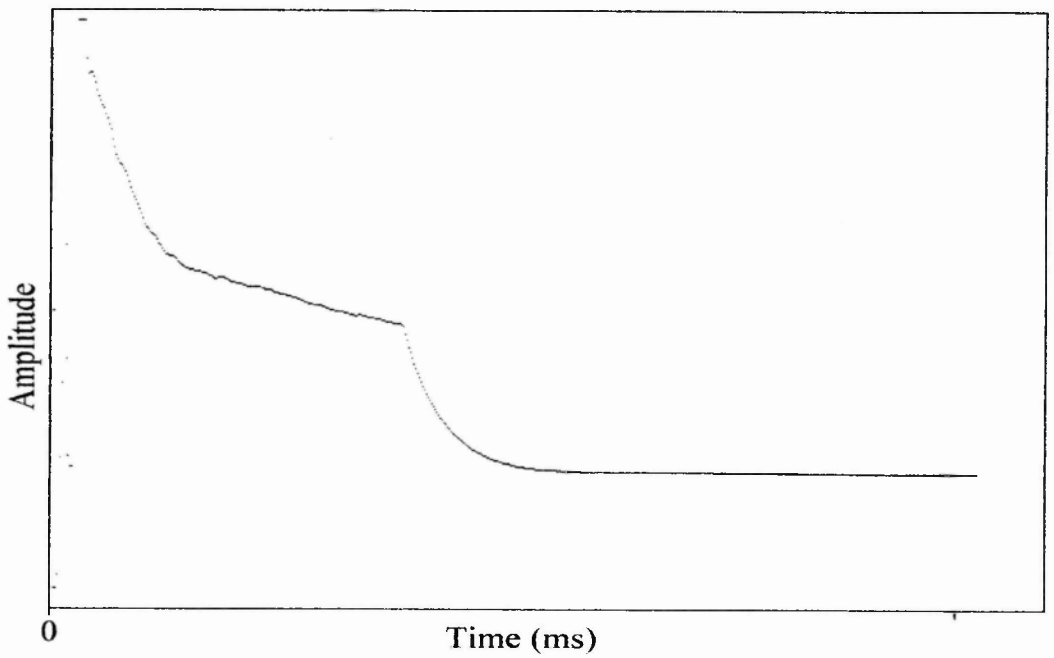

(b)

Figure 33. ^{1}H Free Induction Decay recorded from hydrothermally processed aluminium- and silicon- acetates dried under an infrared lamp recorded on (a) a continuous timescale (b) on a variable timescale

a) Hydrothermally co-processed aluminium- and silicon- acetates

A packed sample of mass 0.27g produced a ^{1}H free induction decay which contained two components (Figures 33(a) and (b)). The first component, located near the origin was typical of that to be expected for a rigid solid whereas the other which was more extensive in time was indicative of liquid-like material. The ratio of the two components was estimated to be 2:1 (rigid : liquid). The continuous timescale recording gave an accurate picture of the free induction decay (Figure 33(a)) whereas the recording measured at two distinct timescales highlighted the rigid component (Figure 33(b)).

This result is not inconsistent with the x-ray powder diffraction measurement; the component of the free induction decay curve attributable to hydrogen-containing material held in a rigid environment could be associated with a species such as pseudoboehmite, whereas the hydrogen-containing material held in a mobile environment could be associated with hydrated silica or surface held water.

b) Dried, acidified hydrothermally co-processed aluminium- and silicon- acetates

There was no observable difference between the free induction decay recorded from this sample and the free induction decay curve recorded from the previous sample.

c) Hydrothermally co-processed aluminium- and silicon- acetates calcined at 500°C

A packed sample of mass 0.27g produced a free induction decay which had an intensity reduced by 40% compared to the free induction decay recorded from the dried powder. The signal again consisted of two components.

The component attributable to hydrogen-containing material in a rigid environment was largely unchanged compared to the dried powder, but the length of time taken for the component attributable to hydrogen-containing material in a mobile environment to tail off was reduced by a factor of four. The ratio between the two components was estimated to be 4:1 (rigid : liquid).

This indicates that the mobility of the hydrogen-containing material in this component has been significantly restricted. The phase change $\gamma - AlOOH.nH_2O \rightarrow \gamma - Al_2O_3$ observed at this calcination temperature in the x-ray powder diffraction analyses would explain the lower intensity of the ^1H free induction decay observed. The loss of water of crystallisation during the phase change could also explain the decreased mobility of the hydrogen-containing material observed.

d) Acidified hydrothermally co-processed aluminium- and silicon- acetates calcined at 500°C

There was no observable difference between the free induction decay recorded from this sample and the free induction decay recorded from the previous sample.

e) Hydrothermally co-processed aluminium- and silicon- acetates calcined at 1250°C

A packed sample of mass 0.27g produced a free induction decay curve which had an intensity reduced by 60% compared to the sample dried under an infrared lamp. The signal consisted of two components. The component which has previously been attributed to hydrogen-containing material in a rigid environment was significantly reduced in size. The component which had previously been attributed to hydrogen-containing material in a mobile environment had a shorter spin-lattice relaxation time than that observed in the free induction decays recorded from either of the two samples (a) and (c). This indicates that whereas there had been a spread of relatively mobile hydrogen-containing material in the free induction decays recorded from samples calcined at less than 1250°C, after calcination at 1250°C the more mobile hydrogen-containing material is lost while the less mobile hydrogen-containing material remains. It is surprising however that any signal can be detected after calcining at a temperature at which the only phase expected is mullite, which should contain no hydrogen-containing material at all.

f) Acidified hydrothermally co-processed aluminium- and silicon- acetates calcined at 1250°C

There was no observable difference between the free induction decay curve recorded from this sample and the free induction decay curve recorded from the previous sample.

4.9.2. The effect of sintering time on the ^1H free induction decay signal

a) Dried, hydrothermally co-processed aluminium- and silicon- acetates

The samples were calcined at 600°C for periods of 3 hrs, 6 hrs, 12 hrs and 24 hrs. The weight lost on calcination was recorded to see whether prolonged calcination times resulted in any further reaction. In each case 0.6g of starting material was used and in each case 0.52g ± 0.1g was obtained.

The free induction decay curves observed from these samples were identical to each other and were similar to the free induction decay curves observed from the samples calcined at 500°C.

b) Dried, acidified hydrothermally co-processed aluminium- and silicon- acetates

The samples were calcined at 600°C for periods of 3 hrs and 24 hrs. The weight lost on calcination was recorded to see whether prolonged calcination times resulted in any further reaction. In each case 0.6g of starting material was used and in each case 0.48g ± 0.1g was obtained.

The free induction decay curves observed from these samples were identical to each other and were similar to the free induction decay curves observed from the samples calcined at 500°C.

4.9.3. The effect of drying and sealing NMR samples under vacuum prior to recording the free induction decay curve

Two batches of samples were made from mullite precursor powder. One batch was prepared by calcining the sample at the requisite temperature and packing the required quantity in an NMR tube. The other batch was prepared by packing the calcined sample in an NMR tube, and exposing it to a vacuum for ca. 2 hours. In this case the packing prevented the fine powder from being sucked into the trap of the vacuum pump. Exposure to the vacuum was gradual and performed over 15-30 minutes. It was observed that the higher the temperature that the sample had been calcined at prior to this process, the easier the process was, due to densification of the samples. The processing conditions were: dried under an infrared lamp followed by calcination at 400°C, 500°C, 800°C, 1150°C, 1250°C and 1400°C.

The sample calcined at 1150°C was run first, and the results are shown in Figures 34(a), 34(b) and 34(c). The results would suggest that the intensity of the signal observed in Figure 34(a) is due to the mullite sample absorbing water from the atmosphere and bonding it to its surface more tightly than would have been expected.

4.10 MICROWAVE HEATING

Microwave heating was performed according to the methods described in Chapter 3 Section 3.3 (p55). The sample prepared from hydrothermally processed aluminium- and silicon- acetates dried under an infrared lamp did not couple with the microwaves used and so the sample did not significantly heat up. The x-ray powder diffraction pattern recorded showed no change from the starting material and was therefore identical to that shown in Figure 19(a). The sample of liquid sol prepared from hydrothermally processed aluminium- and silicon- acetates was used to investigate whether the water would absorb enough microwaves and encourage furthur reaction. The x-ray powder diffraction pattern recorded was identical to that shown in Figure 19(a). The sample prepared from hydrothermally processed aluminium- and silicon- acetates dried under an infrared lamp

which was then ground with 10wt% iron sulphate was used to investigate whether iron sulphate would absorb enough microwaves to encourage furthur reaction. The x-ray powder diffraction pattern recorded was identical to that shown in Figure 19(a). It was therefore decided that a tuneable microwave oven might be a better way of proceeding and could be part of furthur investigations.

4.11. CONCLUSIONS

The results confirm that hydrothermal synthesis is a superior method for forming mullite at a low temperature.

The observed shifting of the (020) and (120) peaks of pseudoboehmite in the x-ray powder diffraction pattern recorded from hydrothermally co-processed aluminium- and silicon-acetates (Section 4.3.), lead to a thorough investigation into precise and accurate measurements of the lattice parameters of the unit cell. The lattice parameters were smaller than those of the pseudoboehmite phase prepared from hydrothermally processed aluminium acetate (Section 4.1.).

There appears to be an interfacial interaction between the aluminium- and silicon-containing phases.

Evidence that this interfacial interaction had some effect on the silicon phase was apparent from the ^{29}Si MASNMR spectra where the difference between the spectra recorded from hydrothermally processed silicon acetate and hydrothermally co-processed aluminium- and silicon- acetates was clear (Figure 17).

Mullite passes through a metastable crystalline state at ca. 1250°C where some of the properties of mullite are not fully developed. This metastability is also evident in the comparative resistances to acid of mullite calcined at 1250°C and 1400°C.

The effect of acid on the progress is not apparent either on the phases which evolve or on the temperature at which the phase transformations occur. Hence it can be concluded that any improvement which acid is observed to have on the final material can be associated with effects on particle charges or particle size.

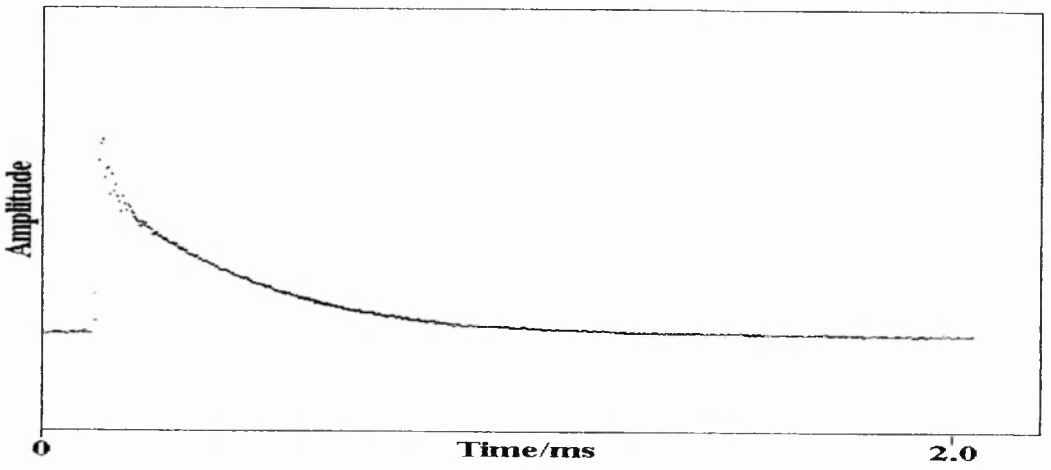

(a)

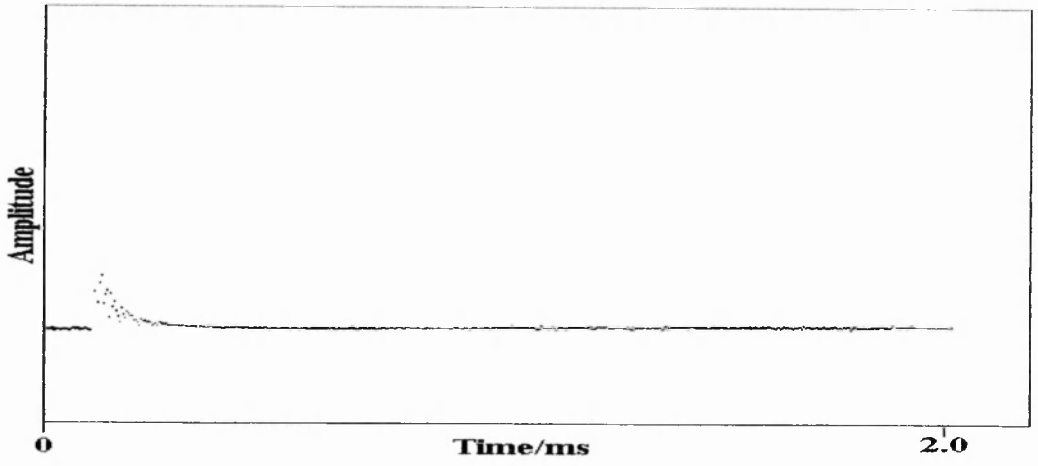

(b)

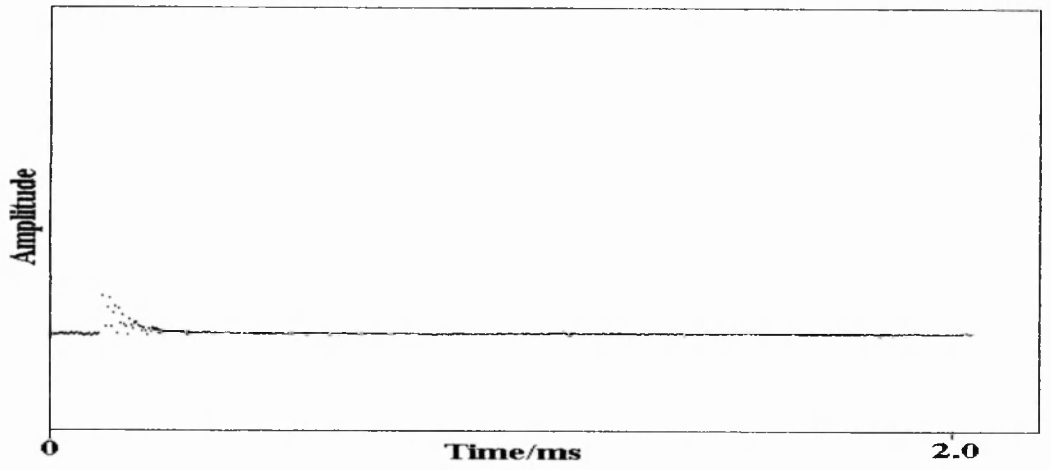

(c)

Figure 34. ^{1}H Free Induction Decay recorded from hydrothermally processed aluminium- and silicon- acetates (a) calcined at $1150^{0}C$ (b) calcined at $1150^{0}C$ and then vacuum sealed. (c) was recorded from an empty sample tube.

4.11. REFERENCES

[1] R. C. T. Slade, J. C. Southern and I. M. Thompson *J. Mater. Chem.* 1991 **1** 875

[2] R. C. T. Slade, J. C. Southern and I. M. Thompson *J. Mater. Chem.* 1991 **1** 563

[3] International Centre for Diffraction Data PDF-2 Database on CD-ROM.

[4] J. A. Gadsden *Infra-red Spectra of Minerals and Related Inorganic Compounds.*

[5] G. E. Maciel and D. W. Sindorf *J. Am. Chem. Soc.* 1980 **102** 7607

[6] D. W. Sindorf and G. E. Maciel *J. Am. Chem. Soc.* 1983 **105** 1487

[7] R. C. T. Slade, J. C. Southern and I. M. Thompson, *J. Mater. Chem.* 1991 **1** 875

[8] J. Sanz, I. Sobrados, A.L. Cavalieri, P. Pena, S. De Aza and J. S. Maya, *J. Am. Ceram. Soc.* 1991 **74** 2398

[9] H. Schneider, L. H. Merwin and A. Sebald, *J. Mater. Sci.* 1992 **27** 805

[10] L. H. Merwin, A. Sebald, H. Rager and H. Schneider, *Phys. Chem. Miner.* 1991 **18** 47

[11] J. Sanz, A. Madini, J. M. Serratosa, J. S. Moya and S. Aza *J. Am. Ceram. Soc.* 1988 **71** C-418

[12] *Handbook of Chemistry and Physics (73rd Edition)* Ed D.R. Lide 1992 Chemical Rubber Company Florida.

[13] M. R. Piramoon, J. Wang, C. B. Ponton and P. M. Marquis in *Processing and Properties of Materials.*

Chapter 5
The Formation of Iron- Doped Mullite by Hydrothermal Processing : Results and Discussion

5.1. THE EVOLUTION OF PHASES OBTAINED BY CALCINING HYDROTHERMALLY PROCESSED IRON(II) ACETATE

5.1.1. X-ray powder diffraction

X-ray powder diffraction patterns were recorded from hydrothermally processed iron(II) acetate which had been dried and ground according to the procedure described in Chapter 3 Section 3.1.1. and then calcined at 300°C, 400°C, 800°C, 1150°C, 1250°C and 1400°C (Figure 35(a)-(g)). The x-ray powder diffraction pattern recorded from the sample dried under an infrared lamp showed the presence of two phases (Figure 35(a)). One phase is characteristic of hematite (α-Fe_2O_3) and the other is characteristic of magnetite (Fe_3O_4). The x-ray powder diffraction pattern recorded from the sample calcined at 300°C (Figure 35(b)), also showed two phases. One phase is characteristic of hematite and the other is characteristic of maghemite ($\gamma - Fe_2O_3$). The x-ray powder diffraction data therefore indicate that Fe_3O_4 converted to $\gamma - Fe_2O_3$ after calcination at 300°C. The decomposition of magnetite to $\gamma - Fe_2O_3$ is known[1] to occur at ca. 300°C. The x-ray powder diffraction patterns for maghemite and magnetite are very similar[63] and the assignment of phases can therefore be difficult, especially if the peaks are broad. The assignment of phases in the materials described here is based on close examination of the relevant x-ray powder diffraction patterns (Figures 35(a) and 35 (b)) in the region 62° - 63° 2θ. The x-ray powder diffraction pattern recorded from the dried material shows a single broad feature centred around 62.5° 2θ. This can be explained in terms of a peak attributable to hematite almost overlapping a peak attributable to magnetite. The x-ray powder diffraction pattern recorded from the material calcined at 300°C shows two partially resolved peaks; one situated at ca. 62.5° 2θ and the other at ca. 63° 2θ. This observation can be attributed to a hematite peak still being present at ca. 62.5° 2θ along with a peak attributable to maghemite now being present at ca 63° 2θ. This detailed examination is therefore in agreement with the decomposition of magnetite into maghemite.

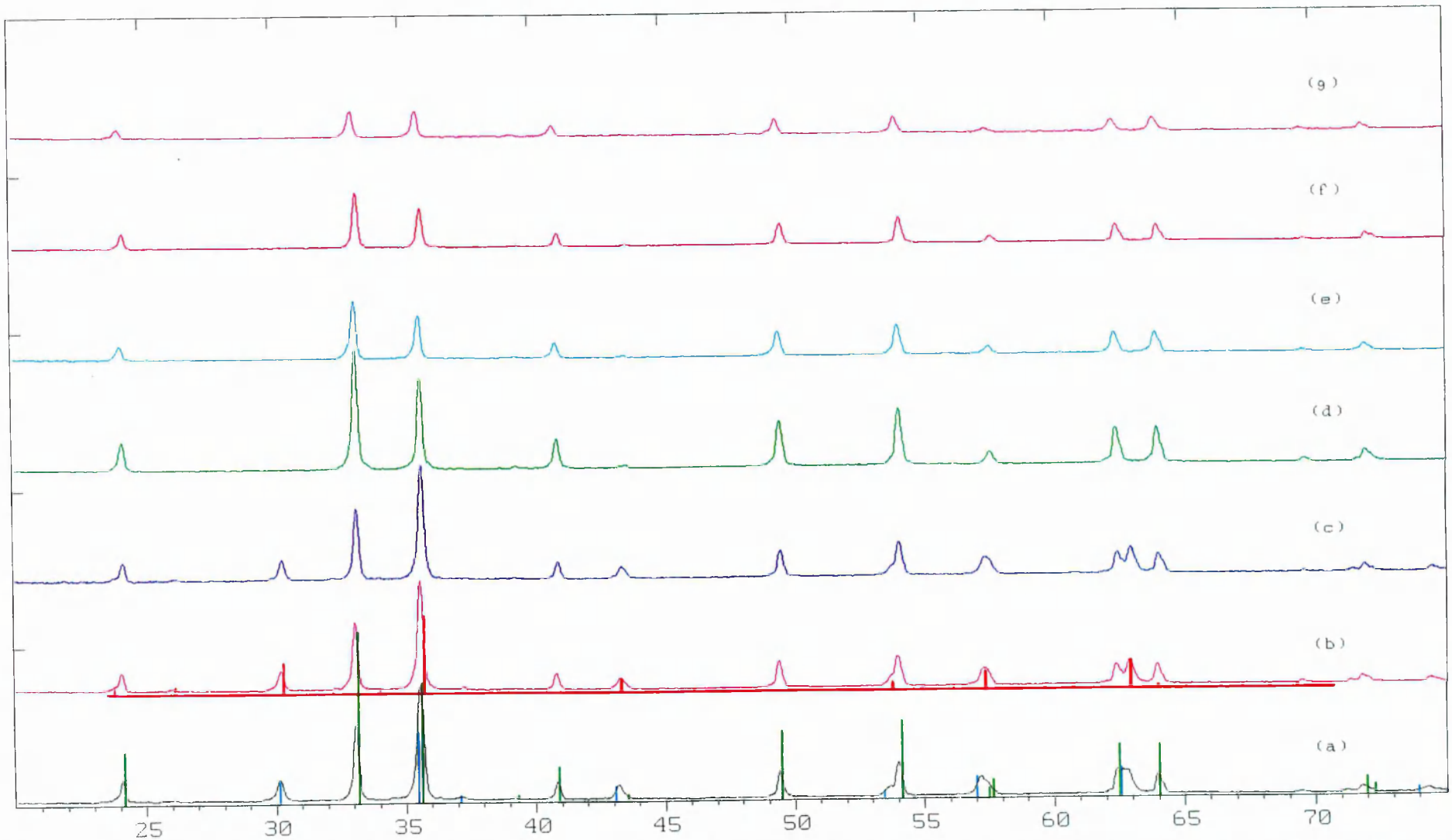

Figure 35. X-ray powder diffraction patterns recorded from hydrothermally processed iron(II) acetate (a) dried under an infrared lamp (b) calcined at 300°C (c) calcined at 400°C (d) calcined at 800°C (e) calcined at 1150°C (f) calcined at 1250°C (g) calcined at 1400°C. The bar diagrams represent the patterns for: figure (a) magnetite and hematite, figure (b) maghemite

The x-ray powder diffraction pattern recorded from the sample calcined at 400°C (Figure 35(c)) is identical to that recorded from the sample calcined at 300°C. The x-ray powder diffraction pattern recorded from the sample calcined at 800°C (Figure 35(d)) shows the material to be single phasic and is characteristic of hematite. Hence maghemite converts to hematite between 400°C and 800°C as previously reported.[75]

The x-ray powder diffraction patterns recorded from samples calcined at 1150°C, 1250°C and 1400°C (Figures 35(e)-(g)) are all characteristic of single phase samples of hematite. This indicates that there are no further phase changes during the calcination of this material at elevated temperature.

5.1.2. Mössbauer spectroscopy

The ^{57}Fe Mössbauer spectrum recorded from the sample dried under an infrared lamp showed two sextets and a singlet (Figure 36(a)). The ^{57}Fe Mössbauer parameters are shown in Table 7:

	Sextet 1		Sextet 2		Singlet
	H/kG ±5	δ/mms^{-1} ±0.05	H/kG ±5	δ/mms^{-1} ±0.05	δ/mms^{-1} ±0.05
Hydrothermally processed iron(II) acetate dried under an infrared lamp	491	0.28	459	0.67	0.62

Table 7. ^{57}Fe Mössbauer parameters recorded from hydrothermally processed iron(II) acetate.

The ^{57}Fe Mössbauer parameters for the two sextets are in good agreement with the literature values[2] for Fe_3O_4 (H=491kG, δ=0.27 mms^{-1} and H=453kG, δ=0.27 mms^{-1}). The observed peak area ratio between sextet 1 : sextet 2 is 32:50 which is close to the value quoted in the literature[75] of 32:68. The presence of two sextets is due to magnetite having an inverse spinel structure with Fe^{3+} ions on the tetrahedral (A) sites and equal numbers of Fe^{3+} and Fe^{2+} ions on the octahedral (B) sites. A sextet is observed for each of the two

environments. The reason why the Fe^{3+} and Fe^{2+} ions on the octahedral (B) sites produce one sextet rather than two sextets is due to rapid electron exchange between these two ions at temperatures above 120K.[3] The singlet is associated with superparamagnetic, small particle Fe_3O_4 (Chapter 2 Section 2.4.3.). Although the effect of superparamagnetism in magnetite has been reported[4,5] the isomer shift for the singlet observed has not been given. The ^{57}Fe Mössbauer spectrum failed to show evidence for α-Fe_2O_3 as identified by x-ray powder diffraction. It is possible that the hematite exists in the superparamagnetic form and is masked by the other features in the central part of the spectrum.

The ^{57}Fe Mössbauer spectrum recorded from the sample calcined at 300°C showed two sextets and a doublet (Figure 36(b)). The ^{57}Fe Mössbauer parameters are shown in Table 8:

	Sextet 1		Sextet 2		Doublet	
	H/kG ±5	δ/mms^{-1} ±0.05	H/kG ±5	δ/mms^{-1} ±0.05	Δ/mms^{-1} ±0.05	δ/mms^{-1} ±0.05
Hydrothermally processed iron(II) acetate calcined at 300°C	513	0.28	491	0.33	0.82	0.32
Hydrothermally processed iron(II) acetate calcined at 400°C	516	0.35	499	0.4	-	-

Table 8. ^{57}Fe Mössbauer parameters recorded from hydrothermally processed iron(II) acetate calcined at 300°C and 400°C.

The ^{57}Fe Mössbauer parameters are in good agreement with the literature parameters [76] for a mixture of hematite (H=517kG, δ=0.37) and maghemite (H=491kG, δ=0.32) and endorse the results obtained from the x-ray powder diffraction patterns recorded from these materials. The doublet in the spectrum recorded from the sample calcined at 300°C arises from small particle α-Fe_2O_3. The particle size of the hematite in this sample is larger than that in the hydrothermally processed iron(II) acetate dried under an infrared lamp.

The ^{57}Fe Mössbauer spectrum recorded from iron(II) acetate hydrothermally processed and calcined at 400°C shows two sextets, characteristic of α-Fe_2O_3 and $\gamma - Fe_2O_3$ (Figure 36(c) and Table 8). The absence of a doublet is indicative of the increasing hematite particle size with calcination temperature.

The ratio of the peak areas for sextet 1 (hematite) : sextet 2 (maghemite) in the ^{57}Fe Mössbauer spectra recorded from iron(II) acetate hydrothermally processed and calcined at 300°C is 40:47. The ratio of the peak areas in the ^{57}Fe Mössbauer spectrum recorded from iron(II) acetate hydrothermally processed and calcined at 400°C for sextet 1 : sextet 2 is 72:28. The difference between the two ratios reflects the increasing size of the hematite particles, (which were previously superparamagnetic and now show bulk behaviour) and the gradual conversion of maghemite into hematite at temperatures exceeding 300°C.[74]

The ^{57}Fe Mössbauer spectra recorded from hydrothermally processed iron(II) acetate calcined at 800°C, 1150°C, 1250°C and 1400°C were all very similar and showed one sextet which can be associated with hematite (Figures 36(d)-(g)). The ^{57}Fe Mössbauer parameters are shown in Table 9.

5.2. THE EVOLUTION OF PHASES OBTAINED BY CALCINING HYDROTHERMALLY CO-PROCESSED ALUMINIUM - AND IRON(II)- ACETATES

5.2.1. X-ray powder diffraction

X-ray powder diffraction patterns were recorded from hydrothermally co-processed aluminium- and iron(II)- acetate which had been dried and ground according to the procedure described in Chapter 3 Section 3.1.1. and then calcined at 300°C, 400°C, 800°C, 1150°C, 1250°C and 1400°C Figures 37(a)-(g).

The x-ray powder diffraction patterns recorded from the material dried under an infrared lamp and the material calcined at 300°C showed three phases, attributable to pseudoboehmite, $\gamma - Al_2O_3$ and hematite (Figures 37(a) and 37(b)). The presence of the pseudoboehmite is to be expected on the basis of the known behaviour of aluminium acetate under such conditions (Chapter 4, Section 4.1.).

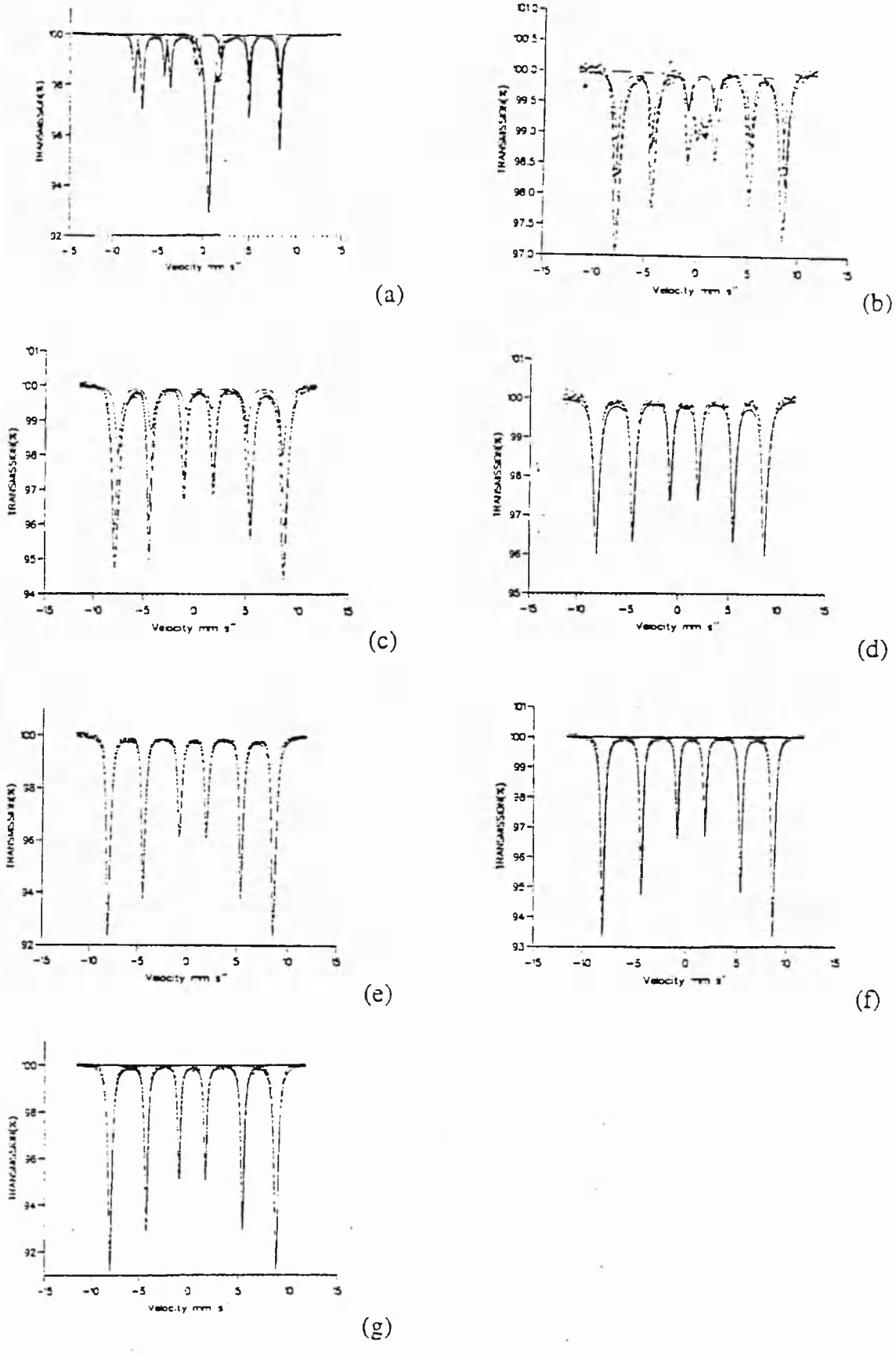

Figure 36. ^{57}Fe Mössbauer spectra recorded from hydrothermally processed iron(II) acetate (a) dried under an infrared lamp (b) calcined at 300°C (c) calcined at 400°C (d) calcined at 800°C (e) calcined at 1150°C (f) calcined at 1250°C (g) calcined at 1400°C

	H/kG ±5	δ/mms^{-1} ±0.05
Hydrothermally processed iron(II) acetate calcined at 800°C	521	0.25
Hydrothermally processed iron(II) acetate calcined at 1150°C	520	0.28
Hydrothermally processed iron(II) acetate calcined at 1250°C	519	0.28
Hydrothermally processed iron(II) acetate calcined at 1400°C	522	0.34

Table 9. ^{57}Fe Mössbauer parameters recorded from hydrothermally processed iron(II) acetate calcined at 800°C, 1150°C, 1250°C and 1400°C.

The iron(II) acetate however shows different behaviour than might have been expected. The x-ray powder diffraction pattern recorded from hydrothermally processed iron(II) acetate dried under an infrared lamp showed the presence of both hematite and magnetite (Section 5.1.1.). It would appear that the presence of aluminium increases the rate of conversion of magnetite into hematite and could be altering the mechanism by which magnetite converts to hematite. When hydrothermally processed iron(II) acetate was calcined, Fe_3O_4 was converted to α-Fe_2O_3 via $\gamma - Fe_2O_3$ (Section 5.1.1.). However, in this case, $\gamma - Fe_2O_3$ was not observed which may reflect either a faster rate of conversion of Fe_3O_4 to α-Fe_2O_3 or a direct conversion of magnetite to hematite as is known to occur when coarsely-crystalline stoichiometric Fe_3O_4 undergoes "dry" oxidation in air. [74] The formation of $\gamma - Al_2O_3$ at 300°C is at a lower temperature than that observed when aluminium acetate is hydrothermally processed (Chapter 4 Section 4.3.) which further suggests that there is an interaction between the aluminium- and the iron- containing phases. It is also notable that $\gamma - Al_2O_3$ is observed to coexist with pseudoboehmite in this system.

The x-ray powder diffraction pattern recorded from the sample calcined at 400°C showed phases characteristic of pseudoboehmite, $\gamma - Al_2O_3$, and hematite (Figure 37(c)) with a distinct increase in the $\gamma - Al_2O_3$ phase. Although the peaks in the samples dried under an

infrared lamp, calcined at 300°C and calcined at 400°C are broad and are complicated by the presence of the iron-containing phase, lattice parameters for pseudoboehmite have been measured using the techniques described in Chapter 4 Section 4.1.2. (Table 10). These are discussed in Section 5.2.2.

The x-ray powder diffraction pattern recorded from the sample calcined at 800°C showed the presence of hematite and $\gamma - Al_2O_3$ (Figure 37(d)). The peaks attributable to $\gamma - Al_2O_3$ had increased in intensity and were less broad than in the x-ray powder diffraction patterns recorded from hydrothermally co-processed aluminium- and iron(II)-acetates calcined at 300°C and 400°C. These changes indicate that all the pseudoboehmite is converted at 800°C into $\gamma - Al_2O_3$ and that the $\gamma - Al_2O_3$ phase is more crystalline.

The x-ray powder diffraction patterns recorded from the samples calcined at 1150°C and 1250°C (Figures 37(e) and 37(f)) showed two phases characteristic of hematite and corundum ($\alpha - Al_2O_3$). This is consistent with earlier results (Chapter 4 Section 4.1.), which showed that $\gamma - Al_2O_3$ converts to corundum at similar temperatures.

The intensity of the pattern corresponding to the hematite phase was observed to decrease in samples heated at the higher temperature. This is likely to indicate that iron is substituting into the corundum lattice as corundum and hematite are isomorphous. The solubility of α-Fe_2O_3 in $\alpha - Al_2O_3$ is reported to be ca. 11 mol%.[6]

The x-ray powder diffraction pattern recorded from the sample calcined at 1400°C (Figure 37(g)) showed a main phase attributable to corundum along with two phases of very small intensity. One of the phases is the hematite phase; the reduced intensity reflects the substitution of iron into the corundum lattice. The other phase which is of very low intensity can be attributed to $AlFeO_3$. This could suggest that as the iron, which was added at a level of 14 mol%, substitutes into the corundum lattice and approaches the maximum reported solubility of ca. 11 mol%,[79] some of the displaced aluminium reacts with the excess iron to form $AlFeO_3$.

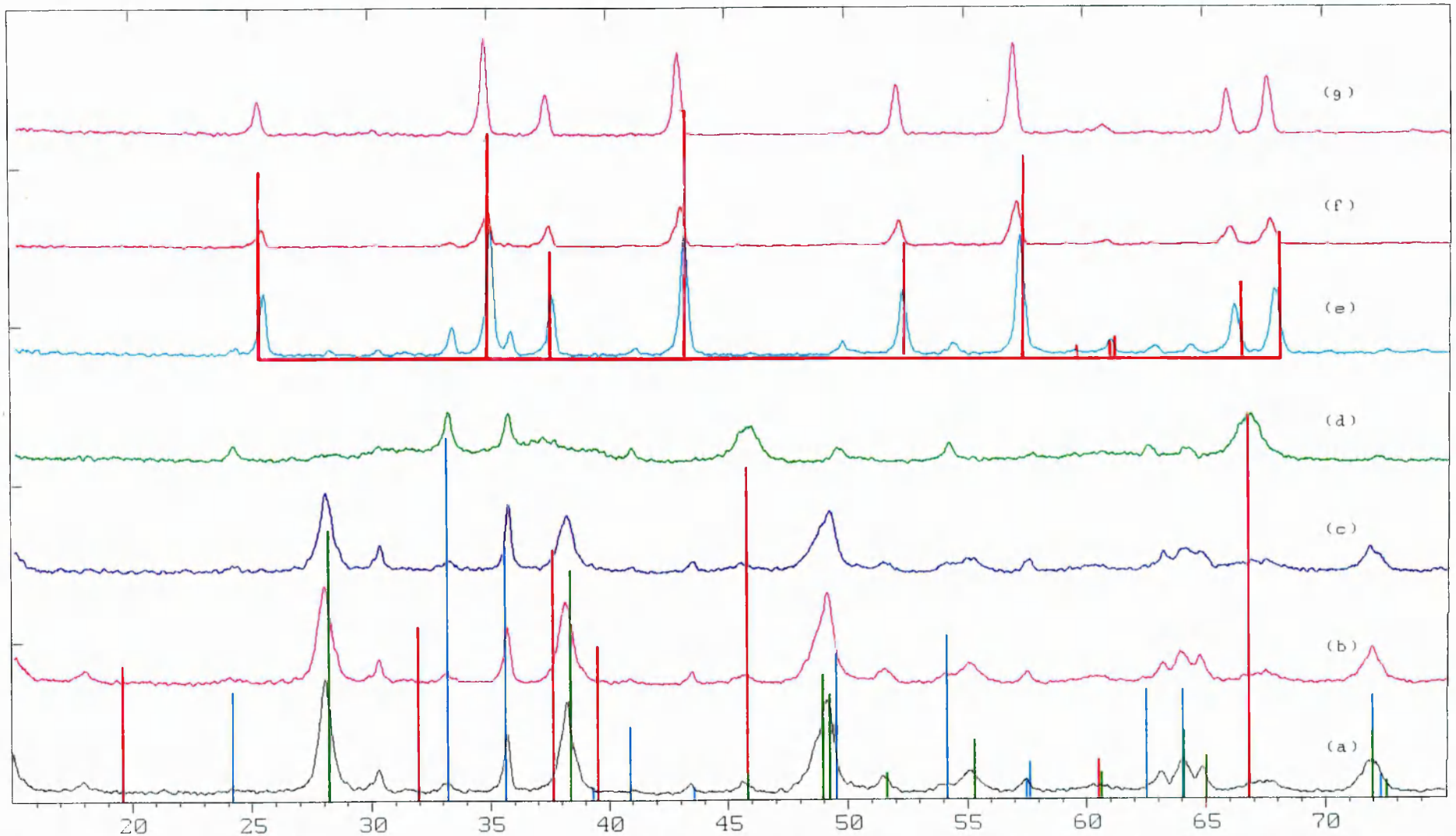

Figure 37. X-ray powder diffraction patterns recorded from hydrothermally co-processed aluminium- and iron(II)- acetates (a) dried under an infrared lamp (b) calcined at 300°C (c) calcined at 400°C (d) calcined at 800°C (e) calcined at 1150°C (f) calcined 1250°C (g) calcined at 1400°C. The bar diagrams represent the patterns for: figure (a) boehmite, $\gamma - Al_2O_3$ and hematite, figure (e) corundum

5.2.2. Lattice parameters

The lattice parameters (calculated from the 10 most intense peaks) of the pseudoboehmite phase observed in the x-ray powder diffraction patterns recorded from hydrothermally co-processed aluminium- and iron- acetates dried under an infrared lamp, calcined at 300°C and calcined at 400°C (Figures 37(a)-(c)) are shown in Table 10. The lattice parameters were recorded using the method described in Section 3.5.2 (p.57). The ***a*** and ***c*** lattice parameters are similar to those for pseudoboehmite previously recorded in this work (Tables 1 and 5). The ***b*** lattice parameter is slightly lower than that observed for pseudoboehmite prepared by the hydrothermally processing of aluminium acetate (Chapter 4 Section 4.1.) and slightly higher than that observed for pseudoboehmite prepared hydrothermally co-processed aluminium- and silicon- acetates, where a strong interfacial interaction was observed (Table 5). The results suggest that there was some interfacial interaction occurring between the aluminium and iron although it is not as strong as that observed for hydrothermally co-processed aluminium- and silicon- phases.

The lattice parameters (calculated from the 10 most intense peaks) for the hematite phases observed in the x-ray powder diffraction patterns recorded from hydrothermally co-processed aluminium- and iron(II)- acetates calcined between 400°C and 1250°C (Figures 37(c)-(f)) are shown in Table 11.

The decrease in the lattice parameters with increasing calcination temperature may indicate that some aluminium enters the hematite structure. This would indicate that both the hematite phase and the corundum phase observed in the x-ray powder diffraction patterns are partially doped by each other. The relatively small size of the Al^{3+} (54 pm) ionic radius compared to the Fe^{3+} (65 pm) ionic radius makes the observed decrease in lattice parameters the expected observation. Corundum and hematite are isostructural and the quantity of aluminium in the hematite phase appears to increase with increasing calcination temperature as illustrated by the general downward trend of the lattice parameters with increasing calcination temperature. The reduction in the lattice parameters is significantly larger between calcination at 400°C and 800°C than that between calcination of the material at 800°C and 1150°C.

Sample History	Lattice Parameters /Å		
	a±0.01	b±0.025	c±0.005
Pseudoboehmite prepared by drying hydrothermally co-processed aluminium- and iron(II)- acetates	3.666	12.151	2.855
Pseudoboehmite prepared by calcining hydrothermally co-processing aluminium- and iron(II) acetates at 300°C	3.662	12.134	2.852
Pseudoboehmite prepared by calcining hydrothermally co-processing aluminium- and iron(II) acetates at 400°C	3.670	12.141	2.854
Literature values for boehmite [63]	3.700	12.227	2.868

Table 10. Lattice parameters for pseudoboehmite prepared by drying and calcining hydrothermally co-processed aluminium- and iron(II)- acetates at 300°C and 400°C

Sample History	Lattice Parameters /Å	
	a±0.005	b±0.005
Hematite prepared by calcining hydrothermally co-processing aluminium- and iron(II)- acetates at 400°C	4.995	13.629
Hematite prepared by calcining hydrothermally co-processing aluminium- and iron(II)- acetates at 800°C	4.987	13.604
Hematite prepared by calcining hydrothermally co-processing aluminium- and iron(II)- acetates at 1150°C	4.988	13.598
Hematite prepared by calcining hydrothermally co-processing aluminium- and iron(II) acetates at 1250°C	4.979	13.571
Literature values for hematite [63]	5.037	13.756

Table 11. Lattice parameters for hematite prepared by hydrothermally co-processing aluminium- and iron(II)- acetates and calcining between 400°C and 1250°C.

There is a phase transformation from $\gamma - Al_2O_3$ to corundum between 800°C and 1150°C which would seem to indicate that the amount of aluminium in the hematite structure remains almost static across the temperature range at which a phase transformation occurs. The maximum reported solubility of alumina in hematite is ca. 10 mol%. [80]

It is interesting to note the indication that hematite is initially doped by aluminium from $\gamma - Al_2O_3$. If this is the case then it is possible that $\gamma - Al_2O_3$ could be doped by iron from hematite. Unfortunately it is not possible to determine the lattice parameters of $\gamma - Al_2O_3$ because of the broad amorphous nature of the peaks.

The lattice parameters (calculated from 10 high angle peaks) for the corundum phases (hexagonal) observed in the x-ray powder diffraction patterns recorded from hydrothermally co-processed aluminium- and iron(II)- acetates calcined between 1150°C and 1400°C (Figures 37(e)-(g)) were calculated using the methods described in Section 4.1.2., and are shown in Table 12.

The increase in the lattice parameters can be associated with Fe^{3+} (65 pm) replacing Al^{3+} (54 pm) in the corundum structure to an increasing degree after calcination at a higher temperature. As the ionic radius for Fe^{3+} is larger than that for Al^{3+} an increase in the lattice parameters when iron enters the corundum structure is the expected outcome.

5.2.3. Mössbauer spectroscopy

The ^{57}Fe Mössbauer spectra recorded from hydrothermally processed aluminium- and iron(II)- acetates dried under an infrared lamp (Figure 38(a)) and subsequently calcined between 300°C and 1400°C (Figures 38(b)-38(g)) showed one sextet and a doublet. The ^{57}Fe Mössbauer parameters are given in Table 13.

The sextet present in all the samples was characteristic of hematite (H=517kG, δ=0.37).[75] In the spectra recorded from the sample dried under an infrared lamp and the sample calcined at 300°C the hematite is poorly crystalline and a substantial part of the structure is superparamagnetic as illustrated by the significant contribution of the doublet to the spectrum.

Sample History	Lattice Parameters /Å	
	a±0.005	b±0.005
Corundum prepared by calcining hydrothermally co-processing aluminium- and iron(II)- acetates at 1150°C	4.782	13.044
Corundum prepared by calcining hydrothermally co-processing aluminium- and iron(II)- acetates at 1250°C	4.787	13.056
Corundum prepared by calcining hydrothermally co-processing aluminium- and iron(II)- acetates at 1400°C	4.795	13.085
Literature values for corundum [63]	4.757	12.988

Table 12. Lattice parameters for corundum prepared by hydrothermally co-processing aluminium- and iron(II)- acetates and calcining between 1150°C and 1400°C.

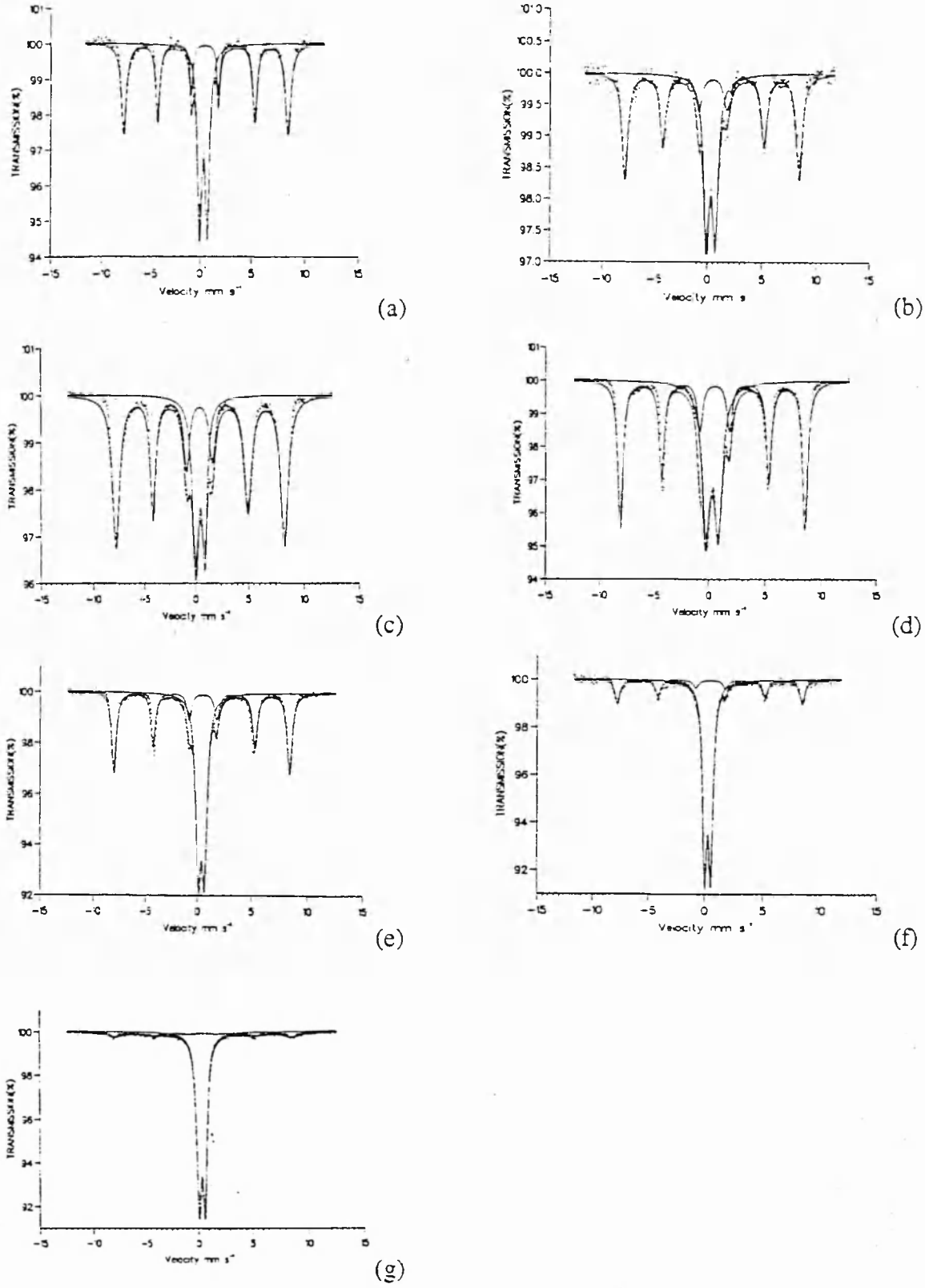

Figure 38. ^{57}Fe Mössbauer spectra recorded from hydrothermally co-processed iron(II)- and aluminium- acetates, (a) dried under an infrared lamp (b) calcined at 300°C (c) calcined at 400°C (d) calcined at 800°C (e) calcined at 1150°C (f) calcined at 1250°C (g) calcined at 1400°C

	Sextet		Doublet	
	H/kG ±5	δ/mms^{-1} ±0.05	Δ/mms^{-1} ±0.05	δ/mms^{-1} ±0.05
Hydrothermally co-processed aluminium- and iron(II)- acetates dried under an infrared lamp	504	0.29	0.78	0.34
Hydrothermally co-processed aluminium- and iron(II)- acetates calcined at 300°C	504	0.27	0.81	0.32
Hydrothermally co-processed aluminium- and iron(II)- acetates calcined at 400°C	501	0.21	0.89	0.41
Hydrothermally co-processed aluminium- and iron(II)- acetates calcined at 800°C	519	0.21	1.09	0.29
Hydrothermally co-processed aluminium- and iron(II)- acetates calcined at 1150°C	515	0.18	0.58	0.38
Hydrothermally co-processed aluminium- and iron(II)- acetates calcined at 1250°C	502	0.28	0.53	0.28
Hydrothermally co-processed aluminium- and iron(II)- acetates calcined at 1400°C	516	0.30	0.57	0.34

Table 13. ^{57}Fe Mössbauer parameters recorded from hydrothermally co-processed aluminium- and iron(II)- acetates dried under an infrared lamp and calcined at 300°C, 400°C, 800°C, 1150°C, 1250°C and 1400°C.

The magnetic field for the sextet is somewhat smaller than the literature value of 517 kG and this reduction in magnetic field strength at the nucleus is known for materials where the particle size is too large to show total superparamagnetic behaviour and too small to show complete bulk behaviour. In the spectrum recorded from hydrothermally co-processed aluminium- and iron(II)- acetates calcined at 400°C the intensity of the doublet showed a considerable increase indicative of an additional component. This component may arise from the interfacial interaction between the hematite phase and the $\gamma - Al_2O_3$ phase as suggested by x-ray powder diffraction.

In the ^{57}Fe Mössbauer spectrum recorded from hydrothermally co-processed aluminium- and iron(II)- acetates calcined at 800°C the fully crystalline hematite phase exhibits the magnetic field strength at the nucleus expected from bulk hematite. The decrease in the ratio of the sextet to the doublet corresponds to the loss of superparamagnetic hematite. This result is consistent with the x-ray powder diffraction pattern which showed that hematite is the only iron-containing phase present.

The ^{57}Fe Mössbauer spectrum recorded from hydrothermally co-processed aluminium- and iron(II)- acetates calcined at 1150°C shows a sextet attributable to hematite and a doublet attributable to iron in corundum ($\alpha - Al_2O_3$).

The ratios between the sextet and the doublet in the spectra recorded from hydrothermally co-processed aluminium- and iron(II)- acetates calcined at 1250°C and 1400°C are 24:76 and 22:78 respectively and although very similar support the incorporation of iron into the corundum structure with increasing calcination temperature. The decrease in the hematite structure lattice parameters with increasing calcination temperature (Section 5.2.2.) does not appear to influence the ^{57}Fe Mössbauer spectra. This contrasts with the reported[7,8] linear reduction of the magnetic field at the nucleus for aluminium doped hematite from a value for pure hematite of 518 kG to 512 kG at 14 mol% aluminium doping.

5.3. THE EVOLUTION OF PHASES OBTAINED BY CALCINING HYDROTHERMALLY CO-PROCESSED SILICON- AND IRON(II)- ACETATES

5.3.1. X-ray powder diffraction

X-ray powder diffraction patterns were recorded from hydrothermally co-processed silicon- and iron(II)- acetate which had been dried and ground according to the procedure described in Chapter 3 Section 3.1.1. and then calcined at 300°C, 400°C, 800°C, 1150°C, 1250°C and 1400°C (Figures 39(a)-(g)). The x-ray powder diffraction patterns recorded from the dried material and the samples of hydrothermally co-processed silicon- and iron(II)- acetate calcined at 300°C and 400°C (Figures 39(a)-(c)) showed two phases characteristic of hematite and maghemite. The presence of silicon was evident by the increase of noise in the baseline and a broadened peak which had a maximum at ca. 22°2θ and spanned the range 15°2θ - 45°2θ. This peak is therefore assignable to an amorphous hydrated form of SiO_2.[51]

The absence of magnetite in the x-ray diffraction pattern recorded from the sample dried under an infrared lamp would suggest that one effect of silicon in this system is to increase the speed of conversion from magnetite to maghemite compared to hydrothermally processed iron(II) acetate (Section 5.1.1.).

This effect could be a result of the silicon interacting with the iron to form a transformation pathway with a lower activation energy. The presence of maghemite in the x-ray powder diffraction patterns recorded from the sample dried under an infrared lamp, calcined at 300°C, and calcined at 400°C suggests that a second effect of the silicon is to decrease the rate of conversion of maghemite to hematite compared to hydrothermally co-processed aluminium- and iron(II)- acetates (Section 5.2.1.). The x-ray powder diffraction pattern recorded from hydrothermally co-processed silicon- and iron(II)- acetates calcined at 800°C (Figure 39(d) showed one phase, attributable to hematite.

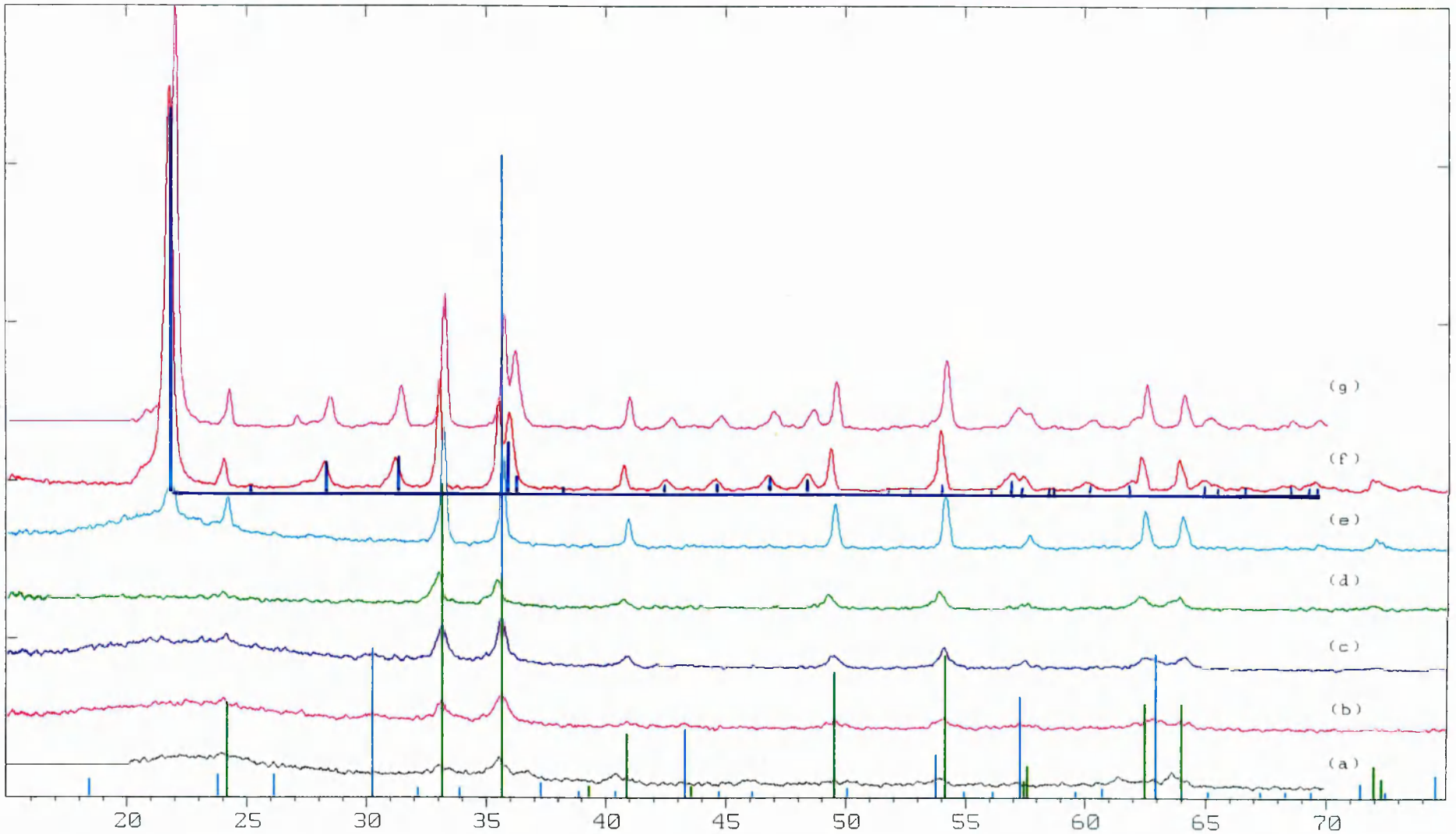

Figure 39. X-ray powder diffraction patterns recorded from hydrothermally co-processed silicon- and iron(II)- acetates (a) dried under an infrared lamp (b) calcined at 300°C (c) calcined at 400°C (d) calcined at 800°C (e) calcined at 1150°C (f) calcined 1250°C (g) calcined at 1400°C. The bar diagrams represent the patterns for: figure (a) hematite and maghemite, figure (f) cristobalite

The disappearance of the large broad peak associated with an amorphous silicon-containing phase in the x-ray diffraction patterns recorded from the samples calcined at 300°C and 400°C is indicative of a change in the nature of the dehydrated silicon-containing phase, although this change does not give rise to any crystalline phases which can be detected by x-ray powder diffraction.

The absence of a phase attributable to maghemite indicates that the maghemite has converted into hematite and complete conversion has occurred at an analogous point to that recorded for hydrothermally processed iron(II) acetate (Section 5.1.1.).

The x-ray powder diffraction patterns recorded from silicon- and iron(II)- acetates calcined at 1150°C, 1250°C and 1400°C (Figures 39(e)-(g)) showed two phases characteristic of hematite and cristobalite. The formation of cristobalite is expected as it was observed during the calcination of hydrothermally processed silicon acetate (Chapter 4 Section 4.2.). The main peak of the cristobalite phase greatly increased in intensity in the material calcined at 1400°C.

5.3.2. Mössbauer spectroscopy

The ^{57}Fe Mössbauer spectra recorded from hydrothermally processed silicon- and iron(II)-acetates dried under an infrared lamp (Figure 38(a)) and hydrothermally processed silicon- and iron(II)- acetates calcined at 300°C and 400°C (Figures 40(a)-(c)) showed one sextet and a doublet. The ^{57}Fe Mössbauer parameters are shown in Table 14. The presence of the doublet is due to the superparamagnetic nature of the hematite particles.

The presence of a small amount of maghemite in the x-ray powder diffraction patterns is not reflected in the ^{57}Fe Mössbauer spectra.

The ^{57}Fe Mössbauer spectrum recorded from hydrothermally processed silicon- and iron(II)- acetates calcined at 800°C (Figures 40(d)) showed two sextets, with an intensity ratio of 80:6, and a doublet. The ^{57}Fe Mössbauer parameters are shown in Table 15. The high intensity sextet can be attributed to hematite (H=517kG, δ=0.37),[75] and the doublet to superparamagnetic α-Fe_2O_3 which decreases with calcination temperature, due to increasing particle size.

	Sextet		Doublet		Area Ratio	
	H/kG ±5	δ/mms^{-1} ±0.05	Δ/mms^{-1} ±0.05	δ/mms^{-1} ±0.05	Sextet	Doublet
Hydrothermally co-processed silicon- and iron(II) acetates dried under an infrared lamp	501	0.27	0.78	0.36	16	84
Hydrothermally processed silicon- and iron(II) acetates calcined at 300°C	501	0.27	0.89	0.34	17	83
Hydrothermally processed silicon- and iron(II) acetates calcined at 400°C	501	0.27	0.95	0.34	18	82

Table 14. ^{57}Fe Mössbauer parameters recorded from hydrothermally co-processed silicon- and iron(II)- acetates, dried under an infrared lamp, calcined at 300°C and 400°C.

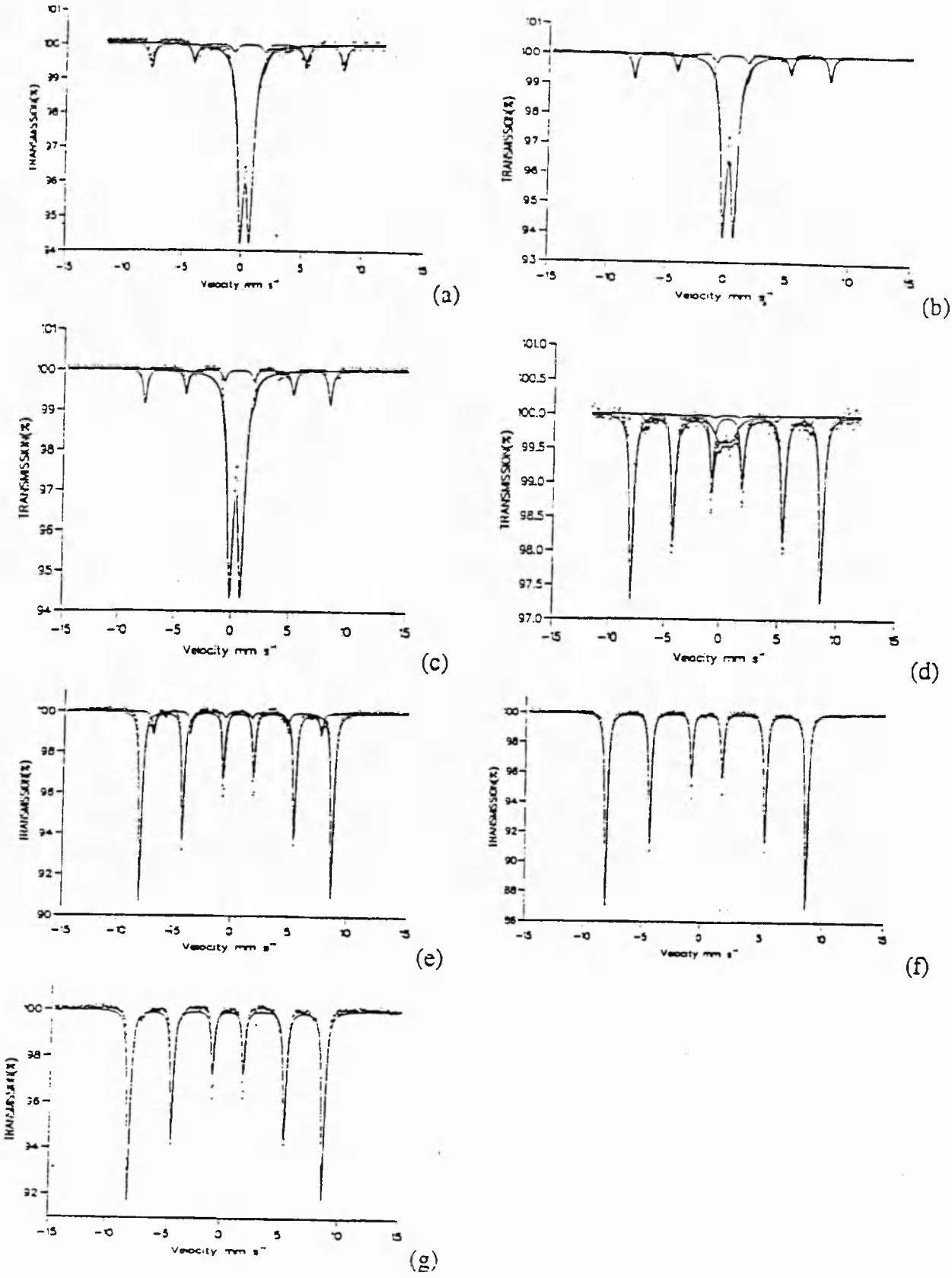

Figure 40. The ^{57}Fe Mössbauer spectra recorded from hydrothermally co-processed iron(II)- and silicon- acetates, (a) dried under an infrared lamp (b) calcined at 300°C (c) calcined at 400°C (d) calcined at 800°C (e) calcined at 1150°C (f) calcined at 1250°C (g) calcined at 1400°C

The low intensity sextet is hard to assign but might result from an amorphous iron silicate species. At room temperature however, Fe_2SiO_4 and Ilvaite both give ^{57}Fe Mössbauer spectra consisting of a doublet.[9,10] The ^{57}Fe Mössbauer spectrum recorded from the sample calcined at 1150°C showed one sextet attributable to hematite and another sextet of low intensity which is likely to correspond to the same species that was identified in the material calcined at 800°C.

The ^{57}Fe Mössbauer spectra recorded from silicon- and iron(II) acetates calcined at 1250°C and 1400°C showed one sextet, attributable to hematite. The ^{57}Fe Mössbauer parameters for these spectra are shown in Table 16. The absence of any other feature in these spectra would indicate that any material containing silicon and iron formed at lower temperatures has broken down to form the expected products of hematite and cristobalite.

5.4. The Evolution of Phases Obtained by Calcining Hydrothermally Co-Processed Aluminium-, Silicon- and Iron(II)- Acetates

5.4.1. X-ray powder diffraction

X-ray powder diffraction patterns were recorded from hydrothermally co-processed aluminium-, silicon- and iron(II)- acetates which had been dried and ground according to the procedure described in Chapter 3 Section 3.1.1. and calcined at 300°C, 400°C, 800°C, 1150°C, 1250°C and 1400°C (Figures 41 (a)-(g)).

The x-ray powder diffraction pattern recorded from hydrothermally co-processed aluminium-, silicon- and iron(II)- acetates dried under an infrared lamp (Figure 41(a)) showed phases attributable to hematite, goethite (α – FeOOH) and pseudoboehmite. The presence of amorphous silica is identifiable by the poor resolution of the peaks and the relatively poor signal/noise ratio.

The x-ray powder diffraction pattern recorded from hydrothermally co-processed aluminium-, silicon- and iron(II)- acetates calcined at 300°C (Figure 41(b)) showed two phases attributable to pseudoboehmite and hematite.

	Sextet 1		Sextet 2		Doublet	
	H/kG ±5	δ/mms^{-1} ±0.05	H/kG ±5	δ/mms^{-1} ±0.05	H/kG ±5	δ/mms^{-1} ±0.05
Hydrothermally co-processed silicon- and iron(II) acetates calcined at 800°C	519	0.27	444	0.30	0.95	0.28
Hydrothermally co-processed silicon- and iron(II) acetates calcined at 1150°C	518	0.28	453	0.25	-	-

Table 15. ^{57}Fe Mössbauer parameters recorded from hydrothermally co-processed silicon- and iron(II)- acetates calcined at 800°C and 1150°C.

	Sextet 1	
	H/kG ±5	δ/mms^{-1} ±0.05
Hydrothermally co-processed silicon- and iron(II)- acetates calcined at 1250°C	518	0.27
Hydrothermally co-processed silicon- and iron(II)- acetates calcined at 1400°C	517	0.28

Table 16. ^{57}Fe Mössbauer parameters recorded from hydrothermally co-processed silicon- and iron(II)- acetates calcined at 1250°C and 1400°.

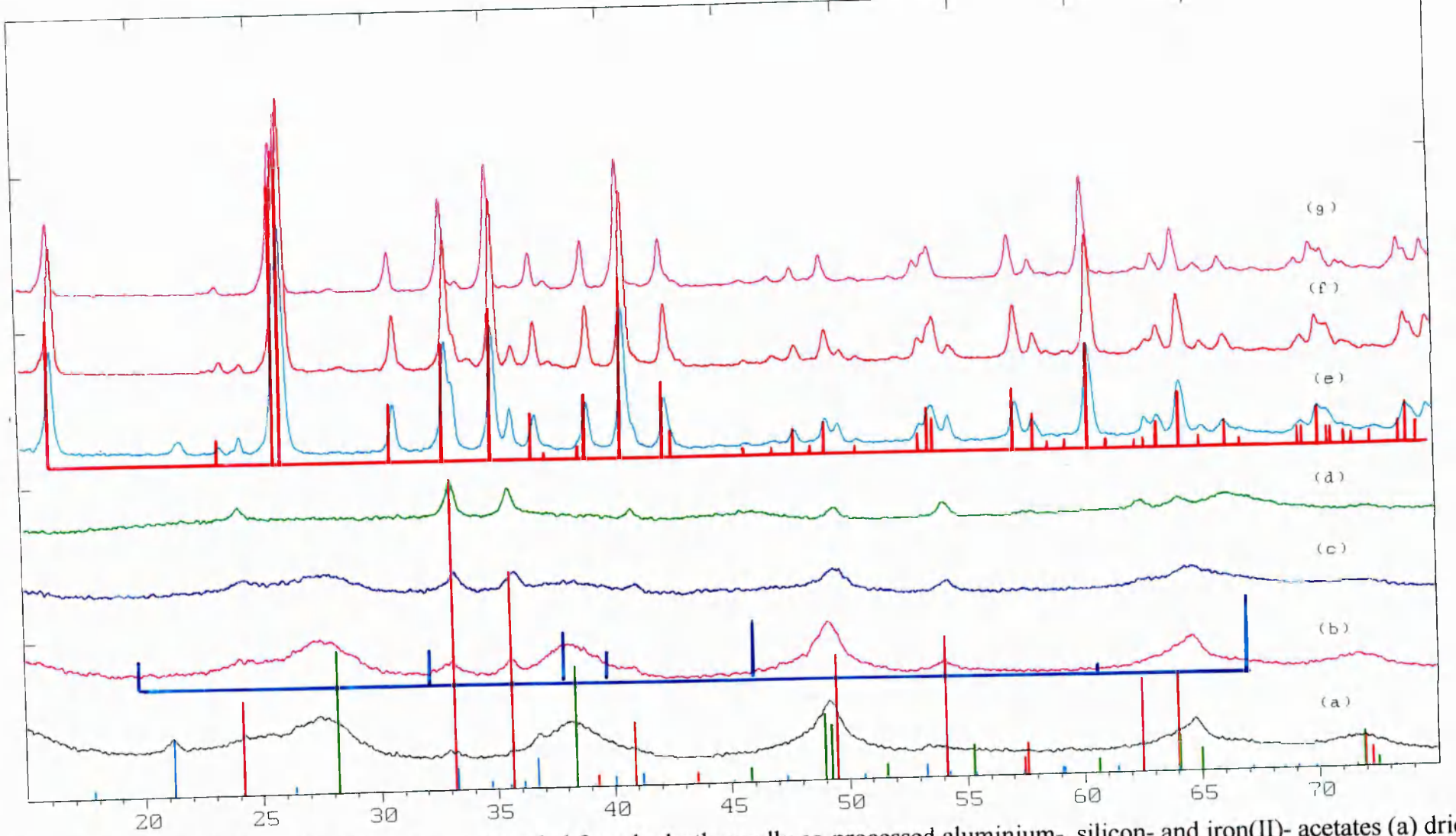

Figure 41. X-ray powder diffraction patterns recorded from hydrothermally co-processed aluminium-, silicon- and iron(II)- acetates (a) dried under an infrared lamp (b) calcined at 300°C (c) calcined at 400°C (d) calcined at 800°C (e) calcined at 1150°C (f) calcined at 1250°C (g) calcined at 1400°C. The bar diagrams represent the patterns for: figure (a) boehmite, goethite and hematite, figure (b) $\gamma - Al_2O_3$, figure (e) mullite

The absence of the 100% goethite peak at ca. 21° 2θ in this pattern suggests that the goethite has been converted into hematite after calcination at 300°C. The peaks are still poorly resolved and the signal/noise ratio is still poor suggesting that the nature of the silicon-containing phase has not been significantly affected.

The x-ray powder diffraction pattern recorded from hydrothermally co-processed aluminium-, silicon- and iron(II)- acetates calcined at 400°C (Figure 41(c)) showed phases attributable to hematite, pseudoboehmite and $\gamma - Al_2O_3$. The presence of $\gamma - Al_2O_3$ is distinguishable by the appearance of a peak at ca. 67° 2θ which is manifest as a shoulder on the pseudoboehmite peak at ca. 65° 2θ. The calcination temperature required to form $\gamma - Al_2O_3$ is 100°C higher in this system than it was for hydrothermally co-processed aluminium- and iron- acetates (Section 5.2.1.) where $\gamma - Al_2O_3$ was observable after calcination at 300°C. This would suggest that silica has a retarding effect on the formation of $\gamma - Al_2O_3$. The co-existence of pseudoboehmite and $\gamma - Al_2O_3$ is notable and contrasts with the results obtained for hydrothermally processed aluminium acetate (Section 4.1.).

The lattice parameters for boehmite were calculated using the methods described in Section 4.1.2. for the sample dried under an infrared lamp and for the samples calcined at 300°C and 400°C (Table 17). The errors on the parameters are higher than in previous systems because the pseudoboehmite peaks had been broadened by the presence of the silica relative to hydrothermally processed aluminium- and iron(II)- acetates (Section 5.2.1.). Also, some pseudoboehmite peaks were not fully resolved from peaks attributable to the iron-containing phase and hence needed mathematical fitting (Appendix A). The results are discussed in Section 5.4.2.

The x-ray powder diffraction pattern recorded from hydrothermally co-processed aluminium-, silicon- and iron(II)- acetates calcined at 800°C (Figure 41(d)) showed two phases attributable to hematite, and $\gamma - Al_2O_3$. The $\gamma - Al_2O_3$ became more crystalline and had increased in quantity detectable by the enlargment of the 100% peak situated at ca. 67° 2θ. In the x-ray powder diffraction pattern recorded from hydrothermally co-processed aluminium-, silicon- and iron(II)- acetates calcined at 400°C the 100% peak of $\gamma - Al_2O_3$ existed as a shoulder on the neighbouring peak at ca. 65° 2θ, which is

attributable to hematite, but in the material heated at 800°C the 100% peak is more intense than its neighbour. The nature of the silicon-containing phase appeared to be unchanged.

The x-ray powder diffraction pattern recorded from hydrothermally co-processed aluminium-, silicon- and iron(II)- acetates calcined at 1150°C (Figure 41(e)) showed two phases attributable to hematite and mullite. The formation of mullite at this temperature is surprising as hydrothermally co-processed aluminium- and silicon acetates were observed to form mullite after calcination at 1250°C (Section 4.3.). This would imply that the presence of the iron assists the formation of mullite.

The x-ray powder diffraction patterns recorded from hydrothermally co-processed aluminium-, silicon- and iron(II)- acetates calcined at 1250°C and 1400°C (Figures 41(f)-(g)) showed one main phase attributable to mullite with a much less intense phase attributable to $AlFeO_3$.

The presence of $AlFeO_3$ has been observed before in these iron-containing systems (Section 5.2.1.) and is attributable to iron atoms entering the mullite structure and displacing some aluminium atoms, which then react with the hematite phase.

The lattice parameters of the mullite phase formed at temperatures exceeding 1150°C are shown in Table 18.

5.4.2. Lattice parameters

The lattice parameters (calculated from the 10 most intense peaks) of the pseudoboehmite phase observed in the x-ray powder diffraction patterns recorded from hydrothermally co-processed aluminium-, silicon- and iron- acetates dried under an infrared lamp, calcined at 300°C and calcined at 400°C (Figures 41(a)-(c)) are shown in Table 17. The lattice parameters were recorded using the method described in Section 3.5.2 (p.57).

The ***a*** and ***c*** lattice parameters for pseudoboehmite prepared by hydrothermally co-processing aluminium-, silicon- and iron(II)- acetates are very similar to those for pseudoboehmite prepared by hydrothermally co-processing aluminium- and iron(II) acetates (Table 10). The ***b*** lattice parameter shows a marked increase relative to all other occurrences of pseudoboehmite in this work and indeed is greater than the standard values for boehmite. This would imply that in the presence of silicon, the interfacial interaction

between the iron-containing phase and the pseudoboehmite phase does not seem to be present and instead it is possible that the iron phase is doping the pseudoboehmite structure which would explain why the lattice parameters are larger than those for standard boehmite.

Sample History	Lattice Parameters /Å		
	a±0.015	b±0.025	c±0.01
Pseudoboehmite prepared by drying hydrothermally co-processed aluminium-, silicon- and iron(II)- acetates under an infrared lamp	3.636	12.396	2.834
Pseudoboehmite prepared by calcining hydrothermally co-processing aluminium-, silicon- and iron(II) acetates at 300°C	3.660	12.300	2.853
Pseudoboehmite prepared by calcining hydrothermally co-processing aluminium- silicon- and iron(II) acetates at 400°C	3.633	12.362	2.836
Literature values for boehmite [63]	3.700	12.227	2.868

Table 17. Lattice parameters for pseudoboehmite prepared by drying and calcining hydrothermally co-processed aluminium-, silicon- and iron(II)-acetates at 300°C and 400°C

It may also be significant therefore that it is only in this system that the formation of goethite, which has a related structure to that of boehmite, was observed.

The lattice parameters (calculated from 10 high angle peaks) for the mullite phase (orthorhombic) observed in the x-ray powder diffraction patterns recorded from hydrothermally co-processed aluminium-, silicon- and iron(II)- acetates calcined between 1150°C and 1400°C (Figures 41(e)-(g)) were calculated using the methods described in Section 4.1.2., and are shown in Table 18.

Comparing the values in this table with those in Table 6 (Section 4.3.) calculated from the mullite phase formed from the calcination of hydrothermally processed aluminium- and silicon- acetates, there is a significant increase in all three lattice parameters. This is to be

expected as the ionic radius of the Fe^{3+} ion is 0.65Å compared to the ionic radius of Al^{3+} which is 0.54Å. It is also interesting to note that the lattice parameters increase with calcination temperature from 1150°C to 1250°C and then decrease upon calcination at 1400°C. This same trend in lattice parameters was observed for calcination of hydrothermally processed aluminium- and silicon- acetates (Section 4.3. Table 6) and this result gives further credence to the possibility that crystalline mullite passes through a metastable state. The question of whether this metastability could be tailored to produce a variety of properties to fulfil specific needs in industry is one which could be investigated in further detail in future work.

Sample History	Lattice Parameters /Å		
	a±0.005	b±0.005	c±0.005
Mullite prepared by calcining hydrothermally processed aluminium-, silicon-, and iron(II)- acetates at 1150°C	7.581	7.720	2.903
Mullite prepared by calcining hydrothermally processed aluminium-, silicon-, and iron(II)- acetates at 1250°C	7.601	7.739	2.906
Mullite prepared by calcining hydrothermally processed aluminium-, silicon-, and iron(II)- acetates at 1400°C	7.586	7.729	2.902
Literature values for mullite [63]	7.542	7.688	2.883

Table 18. Lattice parameters calculated from the peak positions of mullite measured from the x-ray powder diffraction pattern recorded from hydrothermally co-processed aluminium-, silicon- and iron(II)- acetates calcined between 1150°C and 1400°C.

5.4.3. Mössbauer spectroscopy

The ^{57}Fe Mössbauer spectra recorded from hydrothermally processed aluminium-, silicon- and iron(II) acetates dried under an infrared lamp (Figure 42(a)) and subsequently calcined between 300°C and 1250°C all showed a sextet and a doublet (Figures 42(b)-(f)).

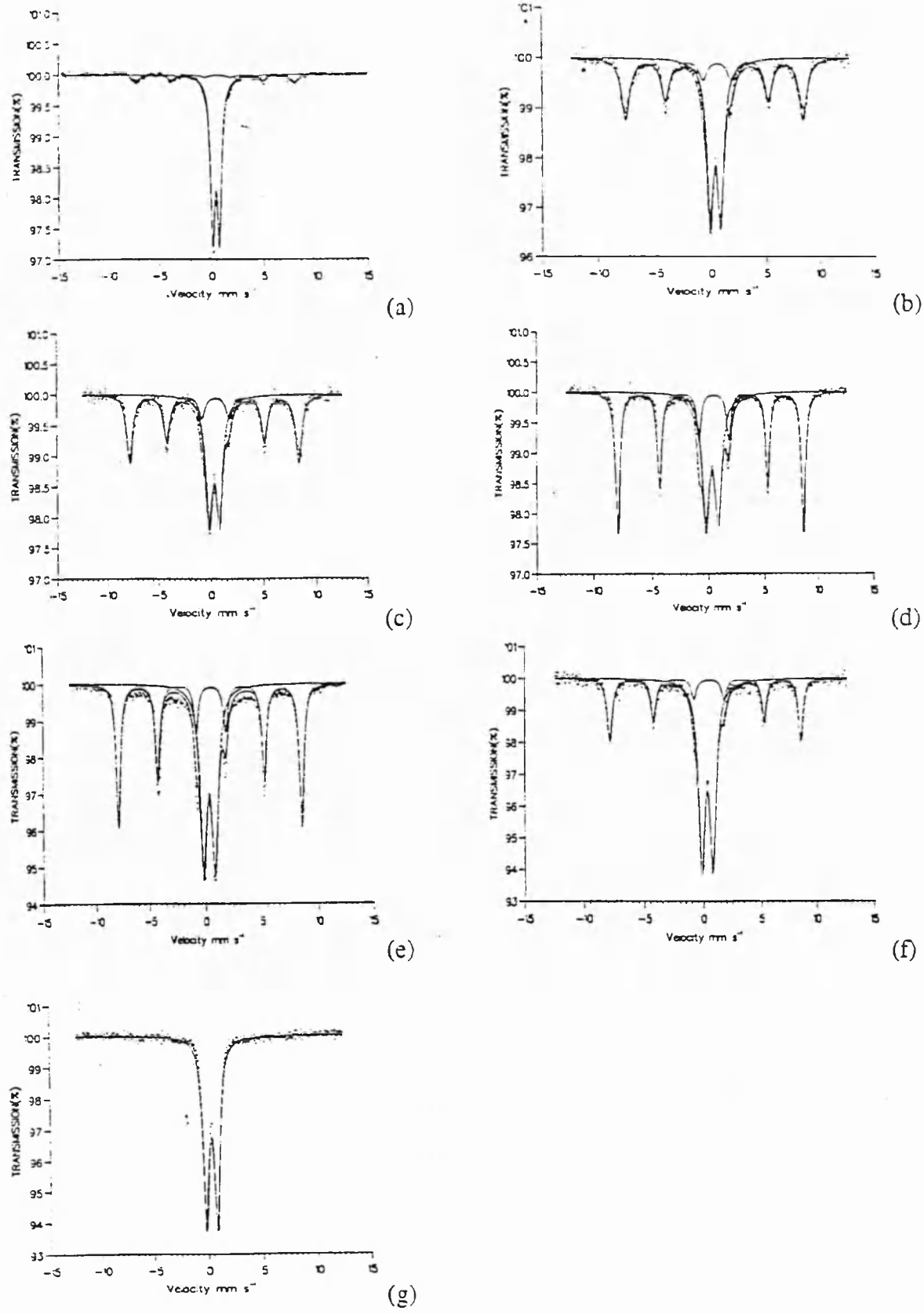

Figure 42. The ^{57}Fe Mössbauer spectra recorded from hydrothermally co-processed iron(II)-, aluminium- and silicon- acetates (a) dried under an infrared lamp (b) calcined at 300°C (c) calcined at 400°C (d) calcined at 800°C (e) calcined at 1150°C (f) calcined at 1250°C (g) calcined at 1400°C

	Sextet		Doublet	
	H/kG ±5	δ/mms^{-1} ±0.05	Δ/mms^{-1} ±0.05	δ/mms^{-1} ±0.05
Hydrothermally co-processed aluminium-, silicon- and iron(II)-acetates dried under an infrared lamp	467	0.27	0.63	0.37
Hydrothermally co-processed aluminium-, silicon- and iron(II)-acetates calcined at 300°C	492	0.32	0.95	0.32
Hydrothermally co-processed aluminium-, silicon- and iron(II)-acetates calcined at 400°C	496	0.31	0.97	0.31
Hydrothermally co-processed aluminium-, silicon- and iron(II)-acetates calcined at 800°C	512	0.32	1.12	0.31
Hydrothermally co-processed aluminium-, silicon- and iron(II)-acetates calcined at 1150°C	507	0.31	1.01	0.30
Hydrothermally co-processed aluminium-, silicon- and iron(II)-acetates calcined at 1250°C	505	0.32	0.98	0.31
Hydrothermally co-processed aluminium-, silicon- and iron(II)-acetates calcined at 1400°C	-	-	1.01	0.30

Table 19. ^{57}Fe Mössbauer parameters recorded from hydrothermally co-processed aluminium-, silicon- and iron(II)- acetates dried under an infrared lamp and calcined at 300°C, 400°C, 800°C, 1150°C, 1250°C and 1400°C.

The ^{57}Fe Mössbauer spectrum recorded from hydrothermally processed aluminium-, silicon- and iron(II)- acetates calcined at 1400°C showed a doublet (Figure 42(g)). The ^{57}Fe Mössbauer parameters are shown in Table 19. The sextet present in the samples is characteristic of hematite. In the spectrum recorded from the material dried under an infrared lamp the hematite has a somewhat low magnetic field at the nucleus of 467 kG. This is to be expected as the large intensity of the doublet is indicative that the particle size is only just too large for the sample to exhibit total superparamagnetism.

The ^{57}Fe Mössbauer spectra recorded from the materials calcined at 300°C and 400°C (Figures 42(b) and 42(c)) showed a decrease in the intensity of the doublet compared to that observed in the spectrum recorded from the sample dried under an infrared lamp. The lack of difference between these spectra contrasts with the results in for hydrothermally co-processed alunminium- and iron(II) acetates (Section 5.2.3.) and could indicate that the interaction between the hematite phase and the $\gamma - Al_2O_3$ phase proposed is blocked in some way by the presence of the silicon. Hence it would appear that small particle α-Fe_2O_3 is converting to larger particle α-Fe_2O_3 with increasing calcination temperature. The ^{57}Fe Mössbauer spectrum recorded from the sample calcined at 800°C (Figure 42(d)) showed a sextet and a doublet. The magnetic field of the sextet has increased significantly compared to the sprectrum recorded at 400°C which is in agreement with the particle size of the hematite increasing. This explanation is supported by the x-ray powder diffraction pattern recorded from hydrothermally co-processed aluminium-, silicon- and iron(II)- acetates calcined at 800°C as the peaks attributable to hematite are very narrow and well resolved indicating that the phase is likely to be fully crystalline and exhibit bulk behaviour.

The ^{57}Fe Mössbauer spectrum recorded from the sample calcined at 1150°C (Figure 42(e)). showed a slight increase in the ratio between the doublet and the sextet. The increase in the size of the doublet is due to the iron doping the mullite structure which has been shown to form at 1150°C (Section 5.4.1.) In the ^{57}Fe Mössbauer spectrum recorded from the sample calcined at 1250°C (Figure 42(f)). the doublet continued to increase and the magnetic field strength of the hematite phase decreased. This result would imply that the hematite phase began to disintegrate in order that the iron can dope the mullite phase.

The ^{57}Fe Mössbauer spectrum recorded from the sample calcined at 1400°C (Figure 42(g)). showed only a doublet indicative of all the iron present being located within the mullite structure. Although in principle it is possible to distinguish between tetrahedral and octahedral Fe^{3+}, in practice it is difficult. The determination of whether Fe^{3+} is located in octahedral or tetrahedral sites was achieved using EXAFS (Section 5.4.6.).

5.4.4. The particle size of iron-doped mullite

Transmission electron microscopy (TEM) was used to examine the particle size of hydrothermally co-processed aluminium-, silicon- and iron- acetates calcined at 1150°C, 1250°C and 1400°C. The micrographs are shown in Figures 43(a)-(c).

The micrograph recorded from the sample calcined at 1150°C (Figure 43(a)) showed a cluster of overlapping platelets ranging in size from ca. 30nm-50nm. The micrograph recorded from the sample recorded at 1250°C (Figure 43(b)) showed a cluster of platelets which are larger and considerably thicker than those observed in the micrograph recorded from the sample calcined at 1150°C. The range of size of the particles is 50nm-100nm and there is evidence of Moiré patterns where the platelets overlap. The Moiré patterns are caused by the slightly different orientation of overlapping crystals. The micrograph recorded from the sample calcined at 1400°C (Figure 43(c)) showed one very large platelet with several smaller platelets lying on top of it. There are some prominent Moiré patterns at the top right of the crystal.

These micrographs show the effect of sintering on particle size, and the increasing markedness of the Moiré fringes suggests that there is an increase of the crystallinity of the mullite phase with calcination temperature.

5.4.5. Quantitative elemental analysis

The amount of iron in the material prepared from hydrothermally co-processed aluminium-, silicon- and iron- acetates calcined at 1150°C, 1250°C and 1400°C, was semi-quantitatively measured using energy dispersive x-ray analysis on STEM (Table 20) [11-12]. Three different areas were examined for each sample to ensure accuracy of results.

The data produced from Measurement 1 and Measurement 2 agreed very closely for each calcination temperature.

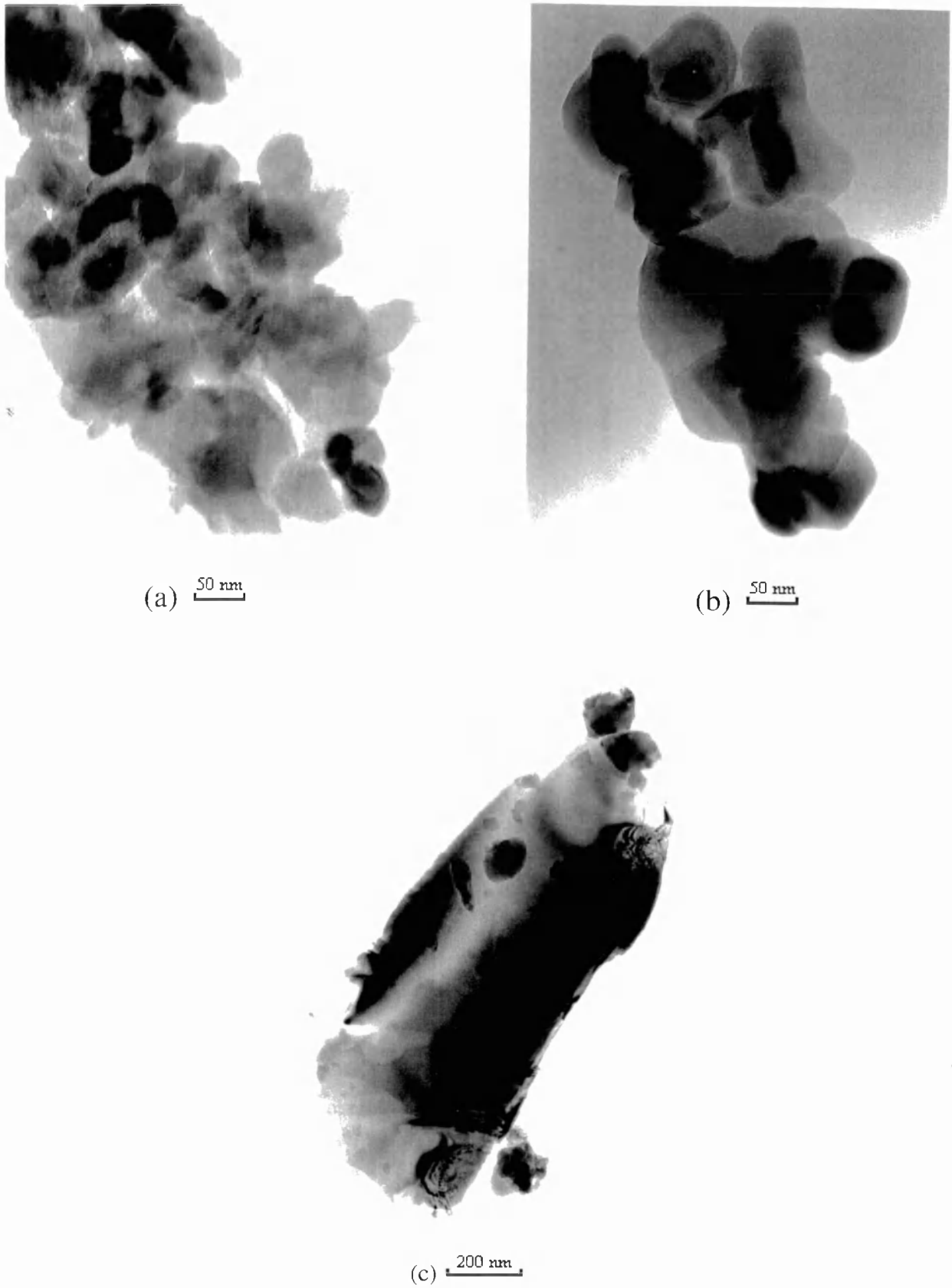

Figure 43. Transmission electron micrographs recorded from hydrothermally co-processed aluminium-, silicon-, and iron- acetates calcined at (a) 1150°C, (b) 1250°C and (c) 1400°C

Calcination Temperature of sample /°C		Aluminium		Silicon		Iron		Weight %			Atomic %		
		Weight %	Atomic%	Weight %	Atomic%	Weight %	Atomic%	Al	Si :	Fe	Al	Si	Fe
1150	Measurement 1	67.07	71.80	21.85	22.47	11.08	5.73	100	33	17	100	31	8
	Measurement 2	66.77	72.08	20.54	21.31	12.68	6.62	100	31	19	100	30	9
	Average	66.10	71.34	21.30	22.09	12.60	6.58	100	32	19	100	31	9
1250	Measurement 1	66.89	71.88	21.28	21.97	11.83	6.14	100	32	18	100	31	9
	Measurement 2	66.87	71.69	21.79	22.44	11.34	5.87	100	33	17	100	31	8
	Average	66.88	71.79	21.54	22.21	11.59	6.01	100	32	17	100	31	8
1400	Measurement 1	61.00	68.26	19.94	21.43	19.07	10.31	100	33	31	100	31	15
	Measurement 2	61.61	68.27	21.14	22.50	17.25	9.23	100	34	28	100	33	14
	Average	61.31	68.27	20.54	21.97	18.16	9.77	100	34	30	100	32	14

Table 20. Energy dispersive x-ray analysis results of iron-containing mullite samples prepared from hydrothermally co-processed aluminium-, silicon- and iron(II)- acetates calcined at 1150°C, 1250°C and 1400°C

The atomic percentages suggest there is no change in the amount of iron in the mullite prepared by calcining hydrothermally processed aluminium-, silicon,- and iron(II)- acetates after calcination at 1150°C and 1250°C. The results are consistent with the interpretation of the ^{57}Fe Mössbauer spectra. The similarity in the amount of iron in mullite after calcination at 1150°C and 1250°C is also consistent with the lattice parameter data (Table 18).

The data obtained from mullite prepared by calcining hydrothermally processed aluminium-, silicon-, and iron(II)- acetates at 1400°C show a large increase in the amount of iron incorporated within mullite and the value of 14 atomic% equated well with the amount added to the reaction mixture (Chapter 3). This result is therefore consistent with the ^{57}Fe Mössbauer spectrum which shows no evidence for any iron-containing phase other than iron-doped mullite.

5.4.6. EXAFS

In order to determine whether the iron replaces aluminium in octahedral or tetrahedral sites when it dopes mullite, the Fe-K-edge EXAFS were recorded, with reference to $FePO_4$, from hydrothermally co-processed aluminium-, silicon- and iron(II)- acetates calcined at 1400°C. Only this sample was suitable as there was only one iron-containing phase present. The experimental and theoretical fourier transforms are shown in Figure 44(a). The coordination number and radii of the shells determined by fitting the data are collected in Table 21.

The results indicate that the first shell is attributable to iron in octahedral coordination and demonstrates that iron replaces aluminium in the chains of AlO_6 octahedra running parallel to the c axis (Chapter 1 Section 1.2.1.).

5.5. THE EVOLUTION OF PHASES OBTAINED BY CALCINING HYDROTHERMALLY CO-PROCESSED ALUMINIUM-, SILICON- AND IRON(III)- ACETATES

5.5.1. X-ray powder diffraction

X-ray powder diffraction patterns were recorded from hydrothermally co-processed aluminium-, silicon- and iron(III)- acetates which had been dried under an infrared lamp and ground according to the procedure described in Chapter 3 Section 3.1.1. and calcined at 300°C, 400°C, 800°C, 1150°C, 1250°C and 1400°C (Figures 45 (a)-(g)).

The x-ray powder diffraction pattern recorded from hydrothermally co-processed aluminium-, silicon- and iron(III)- acetates dried under an infrared lamp (Figure 45(a)) showed phases attributable to hematite, goethite (α – FeOOH) and pseudoboehmite. The presence of silica is identifiable by the poor resolution of the peaks and the relatively poor signal/noise ratio. The x-ray powder diffraction pattern recorded from hydrothermally co-processed aluminium-, silicon- and iron(III)- acetates calcined at 300°C (Figure 45(b)) showed two phases attributable to pseudoboehmite and hematite. The absence of the 100% goethite peak at ca. 21° 2θ suggests that the goethite observed in the x-ray powder diffraction pattern recorded from hydrothermally co-processed aluminium-, silicon- and iron(III)- acetates has been converted into hematite after calcination at 300°C. The peaks are still broad and the signal/noise ratio is still poor suggesting that the nature of the silicon-containing phase has not been significantly affected. The peaks attributable to the hematite phase however are more resolved here than they were in the pattern recorded from hydrothermally co-processed aluminium-, silicon- and iron(II)- acetates calcined at 300°C (Section 5.4.1.).

The x-ray powder diffraction pattern recorded from hydrothermally co-processed aluminium-, silicon- and iron(III)- acetates calcined at 400°C (Figure 45(c)) was virtually identical to that recorded from the material calcined at 300°C.

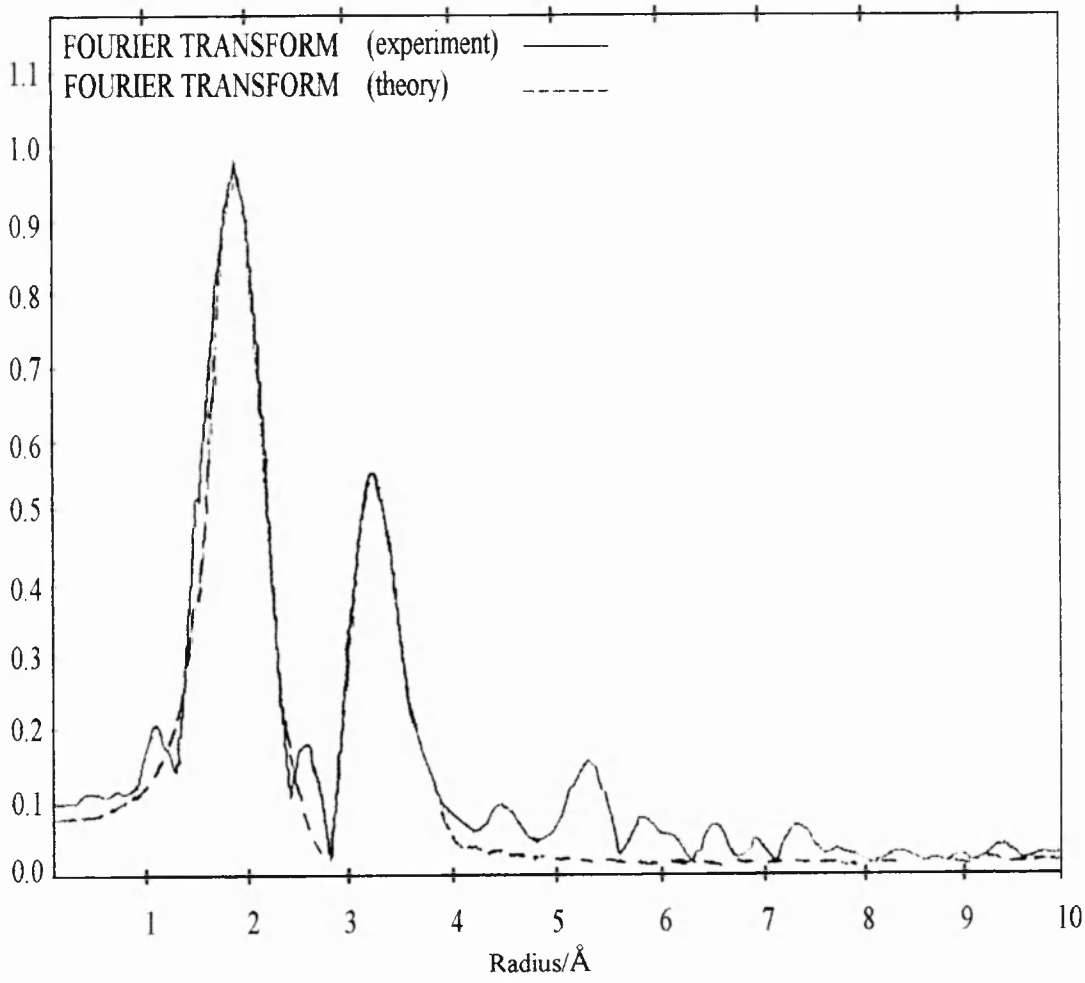

SHELL NUMBER	ELEMENT	COORDINATION	RADIUS/Å
1	O	6	1.936
2	Si	3	3.211

Figure 44. The theoretical and experimental EXAFS fourier transforms recorded from hydrothermally co-processed aluminium-, silicon- and iron(II)- acetates. Table 21. Data used for the theoretical fourier transform

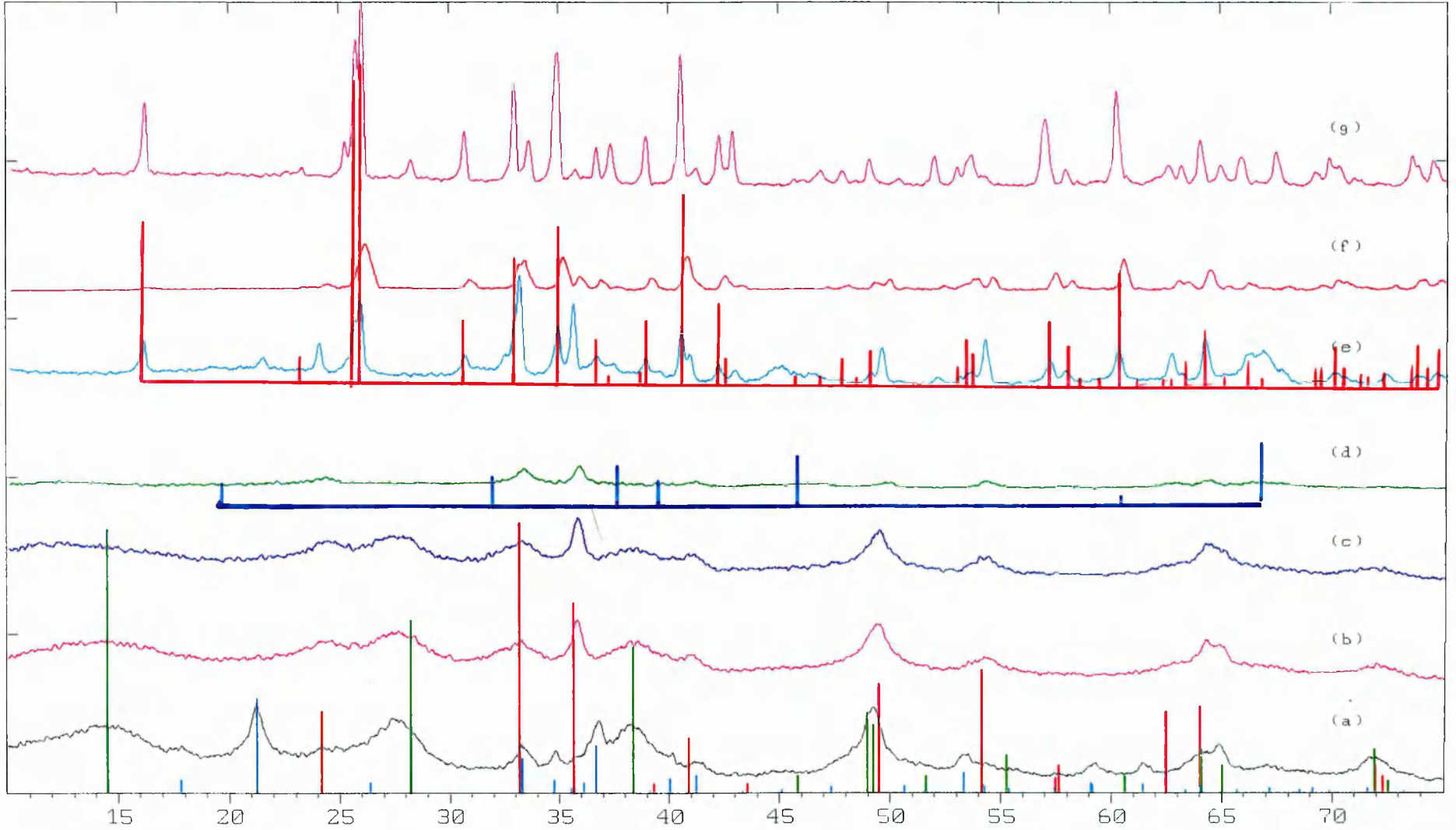

Figure 45. X-ray powder diffraction patterns recorded from hydrothermally co-processed aluminium-, silicon- and iron(III) acetates (a) dried under an infrared lamp (b) calcined at 300°C (c) calcined at 400°C (d) calcined at 800°C (e) calcined at 1150°C (f) calcined at 1250°C (g) calcined at 1400°C. The bar diagrams represent the patterns for: figure (a) boehmite, goethite and hematite, figure (d) $\gamma - Al_2O_3$, figure (e) mullite

The formation of the $\gamma - Al_2O_3$ phase that was observed in the x-ray powder diffraction pattern recorded from hydrothermally co-processed aluminium-, silicon- and iron(II)-acetates calcined at 400°C (Section 5.4.1.) is not apparent.

The x-ray powder diffraction pattern recorded from hydrothermally co-processed aluminium-, silicon- and iron(III)- acetates calcined at 800°C (Figure 45(d)) showed two phases attributable to hematite and $\gamma - Al_2O_3$. The disappearance of the pseudoboehmite phase suggests that it has undergone a phase transformation to $\gamma - Al_2O_3$. This phase transformation is expected and the x-ray powder diffraction pattern recorded from this sample is almost identical to that recorded from hydrothermally co-processed aluminium-, silicon- and iron(II)- acetates calcined at 800°C (Section 5.4.1.). The x-ray powder diffraction pattern recorded from hydrothermally co-processed aluminium-, silicon- and iron(III)- acetates calcined at 1150°C (Figure 45(e)) showed phases attributable to mullite, hematite and $\gamma - Al_2O_3$. This result is interesting because whereas mullite was also formed at 1150°C, by the hydrothermal co-processing of aluminium-, silicon- and iron(II)-acetates (Section 5.4.1.), the baseline in Figure 45(e) is noisy suggesting the presence of a silica-related phase. Also the coexistence of mullite and $\gamma - Al_2O_3$ has not been observed previously in this work.

The x-ray powder diffraction pattern recorded from hydrothermally co-processed aluminium-, silicon- and iron(III)- acetates calcined at 1250°C (Figure 45(f)) showed two phases attributable to mullite and hematite. This result suggests that full conversion of the aluminium-containing and silicon-containing phases to mullite occurs at this temperature.

The x-ray powder diffraction pattern recorded from hydrothermally co-processed aluminium-, silicon- and iron(III)- acetates calcined at 1400°C (Figure 45(c)) showed two phases attributable to mullite and corundum. The formation of corundum is presumably due to iron replacing aluminium in the mullite structure. The absence of a hematite phase would suggest that all the iron has been taken up by the mullite structure.

5.5.2. Mössbauer spectroscopy

The ^{57}Fe Mössbauer spectra recorded from hydrothermally processed aluminium-, silicon- and iron(III)- acetates dried under an infrared lamp (Figure 46(a)) showed a doublet.

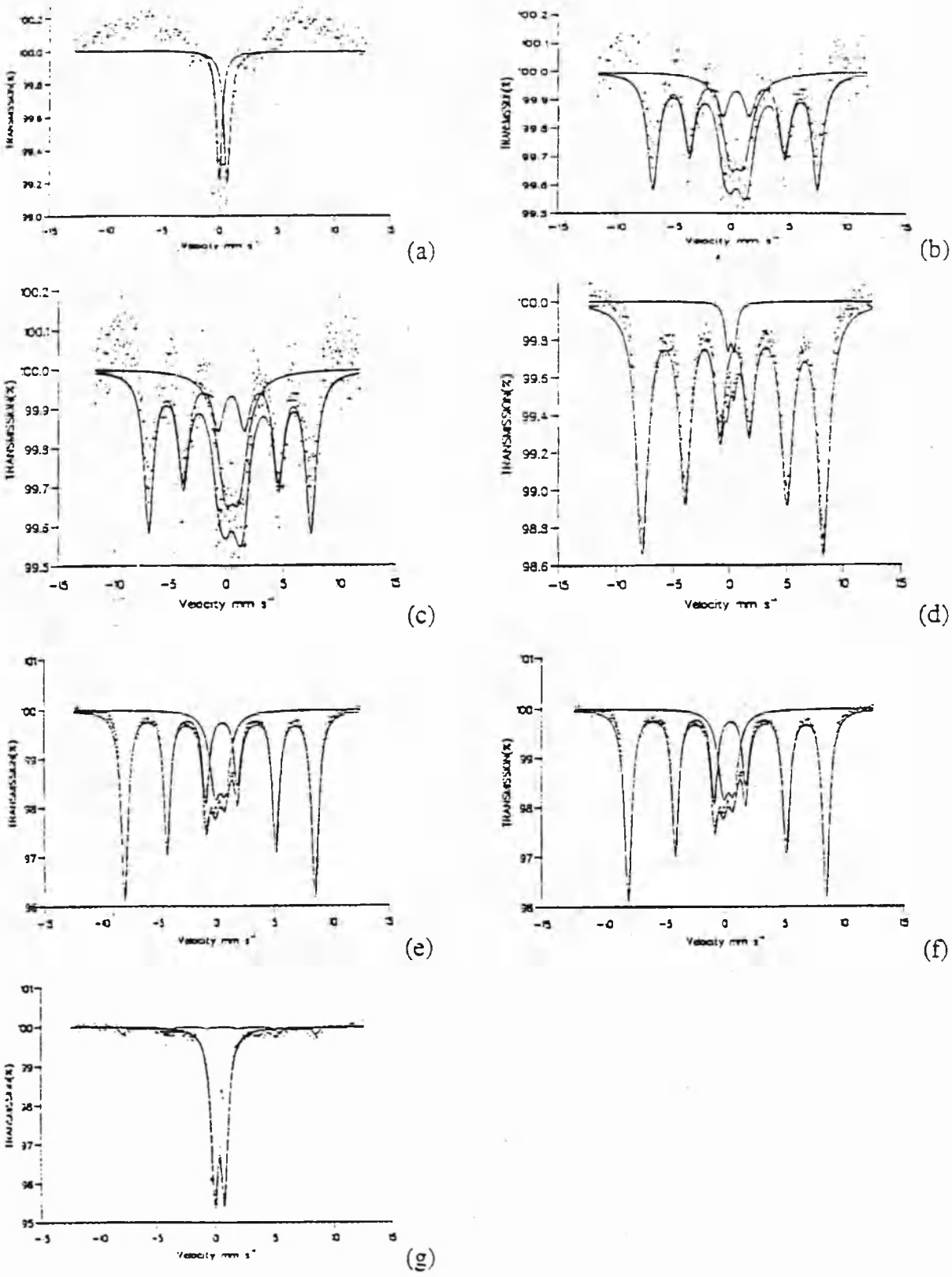

Figure 46. The ^{57}Fe Mössbauer spectra recorded from hydrothermally co-processed iron(III)-, aluminium- and silicon- acetates, (a) dried under an infrared lamp (b) calcined at 300°C (c)calcined at 400°C (d) calcined at 800°C (e) calcined at 1100°C (f) calcined at 1250°C (g) calcined at 1400°C

	Sextet		Doublet	
	H/kG ±5	δ/mms^{-1} ±0.05	Δ/mms^{-1} ±0.05	δ/mms^{-1} ±0.05
Hydrothermally co-processed aluminium-, silicon- and iron(II)-acetates dried under an infrared lamp	-	-	0.69	0.31
Hydrothermally co-processed aluminium-, silicon- and iron(II)-acetates calcined at 300°C	446	0.29	1.20	0.52
Hydrothermally co-processed aluminium-, silicon- and iron(II)-acetates calcined at 400°C	446	0.29	1.20	0.52
Hydrothermally co-processed aluminium-, silicon- and iron(II)-acetates calcined at 800°C	498	0.25	0.58	0.13
Hydrothermally co-processed aluminium-, silicon- and iron(II)-acetates calcined at 1150°C	512	0.25	0.56	0.30
Hydrothermally co-processed aluminium-, silicon- and iron(II)-acetates calcined at 1250°C	513	0.23	1.01	0.35
Hydrothermally co-processed aluminium-, silicon- and iron(II)-acetates calcined at 1400°C	510	0.21	0.81	0.35

Table 22. ^{57}Fe Mössbauer parameters recorded from hydrothermally co-processed aluminium-, silicon- and iron(III)- acetates dried under an infrared lamp and calcined at 300°C, 400°C, 800°C, 1150°C, 1250°C and 1400°C.

The ^{57}Fe Mössbauer spectra recorded from hydrothermally processed aluminium-, silicon- and iron(III)- acetates calcined between 300°C and 1400°C all showed a sextet and a doublet (Figures 46(b)-(g)). The ^{57}Fe Mössbauer parameters are shown in Table 22.

The ^{57}Fe Mössbauer spectrum recorded from the sample dried under an infrared lamp (Figure 46(a) had a complex baseline and required more rigorous background subtraction. The doublet however is characteristic of superparamagnetic hematite. The ^{57}Fe Mössbauer spectra recorded from the samples calcined 300°C and 400°C (Figures 46(b) and 46(g)) had a poor baseline despite being run more than once and for extended periods of time. The spectra are very similar and the value of the magnetic field is typically low for a sample which exhibits a high degree of superparamagnetism. The ^{57}Fe Mössbauer spectrum recorded from the sample calcined at 800°C (Figure 46(d)) showed a sextet characteristic of hematite with a magnetic field of 498 kG which is only slightly smaller than that expected for bulk α-Fe_2O_3. The difference between this spectrum and the spectrum recorded from hydrothermally co-processed aluminium-, silicon- and iron(II)- acetates calcined at 800°C (Table 19) is that the intensity ratio of the sextet to the doublet is much larger. This would indicate that the doublet here is likely to be due to superparamagnetism rather than an interfacial interaction between $\gamma - Al_2O_3$ and hematite (Section 5.4.3.). This result would also suggest that there is no interaction between the hematite phase and the $\gamma - Al_2O_3$ phase in this system. This lack of interfacial interaction at a temperature well below that at which mullite forms may well be the key to why there are such profound differences between two seemingly similar systems.

The ^{57}Fe Mössbauer spectrum recorded from the sample calcined at 1150°C (Figure 46(e)) showed a reduction in the intensity ratio of the sextet to the doublet indicating that there is some level of doping of the mullite phase present by iron. The sextet : doublet intensity ratio is however much lower than that observed in the Mössbauer spectrum recorded from hydrothermally co-processed aluminium-, silicon- and iron(II)- acetates calcined at 1150°C (Table 19). This result is in accordance with the x-ray powder diffraction data which indicated that mullite formation has occurred to a lesser extent after calcining hydrothermally co-processed aluminium-, silicon- and iron(III)- acetates at 1150°C.

The ^{57}Fe Mössbauer spectrum recorded from the sample calcined at 1250°C (Figure 46(f)) showed a more marked decrease in the intensity ratio of the sextet to the doublet. This is indicative of enhanced mullite formation facilitating iron doping. The value of the sextet to doublet intensity ratio is much higher than that recorded from hydrothermally co-processed aluminium-, silicon- and iron(II)- acetates calcined at 1250°C, which could indicate that the mullite formed is slightly different in nature, e.g. less crystalline and is not so amenable to iron doping.

The x-ray powder diffraction pattern recorded from the sample calcined at 1400°C showed that the mullite phase is able to take up iron, however the mullite formed appears to have a lower tolerance for iron doping than that obtained from hydrothermally co-processed aluminium-, silicon- and iron(II)- acetates calcined at 1400°C as not all the iron present is contained in the mullite.

5.6. CONCLUSIONS

(i) The preparation of iron-doped mullite by hydrothermal synthesis confirmed many of the results recorded during the preparation of mullite.

(ii) The lattice parameters of the pseudoboehmite phase present in hydrothermally co-processed aluminium-, silicon- and iron(II)- acetates autoclaved and dried under an infrared lamp (Table 17) were smaller than those for hydrothermally processed aluminium acetate dried under an infrared lamp (Table 1) but larger than those for hydrothermally co-processed aluminium- and silicon- acetates dried under an infrared lamp (Table 5). This implies that any reduction in lattice parameters from an interfacial interaction is partially compensated by iron entering the pseudoboehmite structure and increasing the lattice parameters.

(iii) Some particles produced by hydrothermal processing and drying under an infrared lamp are 18 nm or smaller. This was shown by ^{57}Fe Mössbauer spectra which show superparamagnetism [52] and confirmed the notion that hydrothermal synthesis does lead to very small particle formation.

(iv) Aluminium and silicon effect the phase evolution of iron-containing phases. When iron(II) acetate was hydrothermally processed and dried under an infrared lamp magnetite (Fe_3O_4) was observed which was converted to maghemite ($\gamma - Fe_2O_3$), and then to hematite (α-Fe_2O_3) by calcination. However for hydrothermally co-processed aluminium- and iron(II)- acetates dried under an infrared lamp, the only iron-containing phase present was hematite (α-Fe_2O_3). This would imply that either the phase evolution of iron proceeds via a different mechanism or that the decomposition of the other expected phases is significantly accelerated. For the hydrothermal co-processing of silicon- and iron(II)- acetates dried under an infrared lamp maghemite ($\gamma - Fe_2O_3$) was observed which converted to hematite (α-Fe_2O_3) after calcination. This would suggest that the presence of silicon accelerates the decomposition of magnetite to maghemite, but inhibits the conversion of maghemite to hematite. For the hydrothermal co-processing of aluminium-, silicon- and iron(II)- acetates dried under an infrared lamp goethite (γ-FeOOH) was observed which then converted to hematite after calcination. This would imply that the presence of both silicon and aluminium alter the mechanism by which hematite is formed. This suggests that the phase evolution of iron may be pH sensitive or that silicon- and aluminium- containing phases interact with the iron to form alternative reaction pathways.

(v) The structural similarity between iron-containing phases and the aluminium-containing phases formed resulted in iron also doping intermediate aluminium-containing species such as $\gamma - Al_2O_3$ as well as aluminium doping some iron-containing species, such as hematite.

(vi) Iron(II) acetate is a better starting material for the preparation of iron-doped mullite than iron(III) acetate as crystalline single phasic iron-doped mullite forms at 1150°C when iron(II) acetate is used.

(vii) When iron dopes the mullite structure it replaces aluminium in the AlO_6 octahedral sites rather than the tetrahedral sites. The maximum amount of iron taken up by mullite is 14 mol%.

5.7. REFERENCES

[1] T. W. Swaddle and P. Oltmann *Can. J. Chem.* 1980 **58** 1763

[2] C.W. Childs and J. G. Baker-Sherman *1983 Moessbauer Spectra and Parameters of Standard Samples* Scientific Report 66 N.Z. Soil Bureau New Zealand

[3] G. W. Simmons and H. Leidheiser in *Applications of Mössbauer Spectroscopy Vol. 1.* Ed. R. L. Cohen 1976 Academic Press New York

[4] T. K. McNab, R. A. Fox and J. F. Boyle *J. Appl. Phys.* 1968 **39** 5703

[5] P. Roggwiller and W. Kündig *Solid State Commun.* 1973 **12** 901

[6] F. Gesmundo and C. De Asmundis *J. Phys. Chem. Solids* 1972 **33** 1861

[7] Applied Mössbauer Spectroscopy Chapter 5

[8] E. De Grave, A. E. Verbeek and D. G. Chambaere *Phys. Lett.* 1985 **107A** 181

9 K. Xuemin, S. Goose and B. D. Dunlap *Phys. Chem. Minerals* 1988 16 55

[10] W. Kundig, J. A. Kate, R. H. Lindquist and G. Constabaris *J. App. Phys.* 1967 **38** 947

[11] P. J. Goodhew 1975 *Electron Microscopy and Analysis* Wykeham Publications Ltd., London

[12] P. B. Hirsch, A. Howie, R. B. Nicholson, D. W. Pashley and M. J. Whelan *Electron Microscopy of Thin Crystals* Butterworths, London

Chapter 6 The Formation of Spinel by Hydrothermal Processing: Results and Discussion

6.1. OVERVIEW

Hydrothermally co-processing aluminium- and silicon- acetates produced results which indicated that there was an interaction between pseudoboehmite- and silica gel- related phases. The properties of these precursor materials were not a simple addition of the properties exhibited by the two materials formed by hydrothermally processing the individual reagents.

To ascertain whether this is common to systems other than mullite, the compound spinel, $MgAl_2O_4$ was prepared by hydrothermally co-processing aluminium- and magnesium-acetates.

6.2. THE EVOLUTION OF PHASES OBTAINED BY CALCINING HYDROTHERMALLY PROCESSED ALUMINIUM ACETATE

6.2.1. X-ray powder diffraction

The phases identified and the lattice parameters obtained from x-ray powder diffraction recorded from hydrothermally processed aluminium acetate calcined at various temperatures, were discussed in Chapter 4 Section 4.1.

6.3. THE EVOLUTION OF PHASES OBTAINED BY CALCINING HYDROTHERMALLY PROCESSED MAGNESIUM ACETATE

6.3.1. X-ray powder diffraction

(a) Hydrothermal processing of non-acidified magnesium acetate

X-ray powder diffraction patterns were recorded from magnesium acetate which had been hydrothermally processed, dried, ground and calcined at 500°C (Figure 47) according to the procedures described in Chapter 3 Section 3.1.1 The x-ray powder diffraction pattern recorded from the sample dried under an infrared lamp (Figure 47(a)) was complex and is

likely to represent a mixture of several magnesium-containing phases including hydrated magnesium acetate.

The x-ray powder diffraction pattern recorded from the sample calcined at 500°C is characteristic of periclase (MgO).

(b) Hydrothermal processing of acidified magnesium acetate

X-ray powder diffraction patterns were recorded from acidified magnesium acetate which had been hydrothermally processed, dried, ground and calcined at 500°C (Figure 48) according to the procedures described in Chapter 3 Section 3.1.1 The x-ray powder diffraction pattern recorded from the sample dried under an infrared lamp (Figure 48(a)) is more complex than that recorded from non- acidified magnesium acetate hydrothermally processed and dried under an infrared lamp, and is likely to represent a mixture of several magnesium-containing phases including hydrated magnesium acetate.

The x-ray powder diffraction pattern recorded from the sample calcined at 500°C is characteristic of periclase (MgO).

6.4. THE EVOLUTION OF PHASES OBTAINED BY CALCINING HYDROTHERMALLY CO-PROCESSED ALUMINIUM- AND MAGNESIUM- ACETATES

6.4.1. X-ray powder diffraction

a) Hydrothermal processing of non-acidified aluminium- and magnesium- acetates

X-ray powder diffraction patterns were recorded from aluminium- and magnesium- acetates which had been hydrothermally co-processed, dried, ground and calcined at 400°C, 500°C, 800°C, 1000°C and 1100°C (Figure 49(a)-(f)) according to the procedures described in Chapter 3 Section 3.1.1.

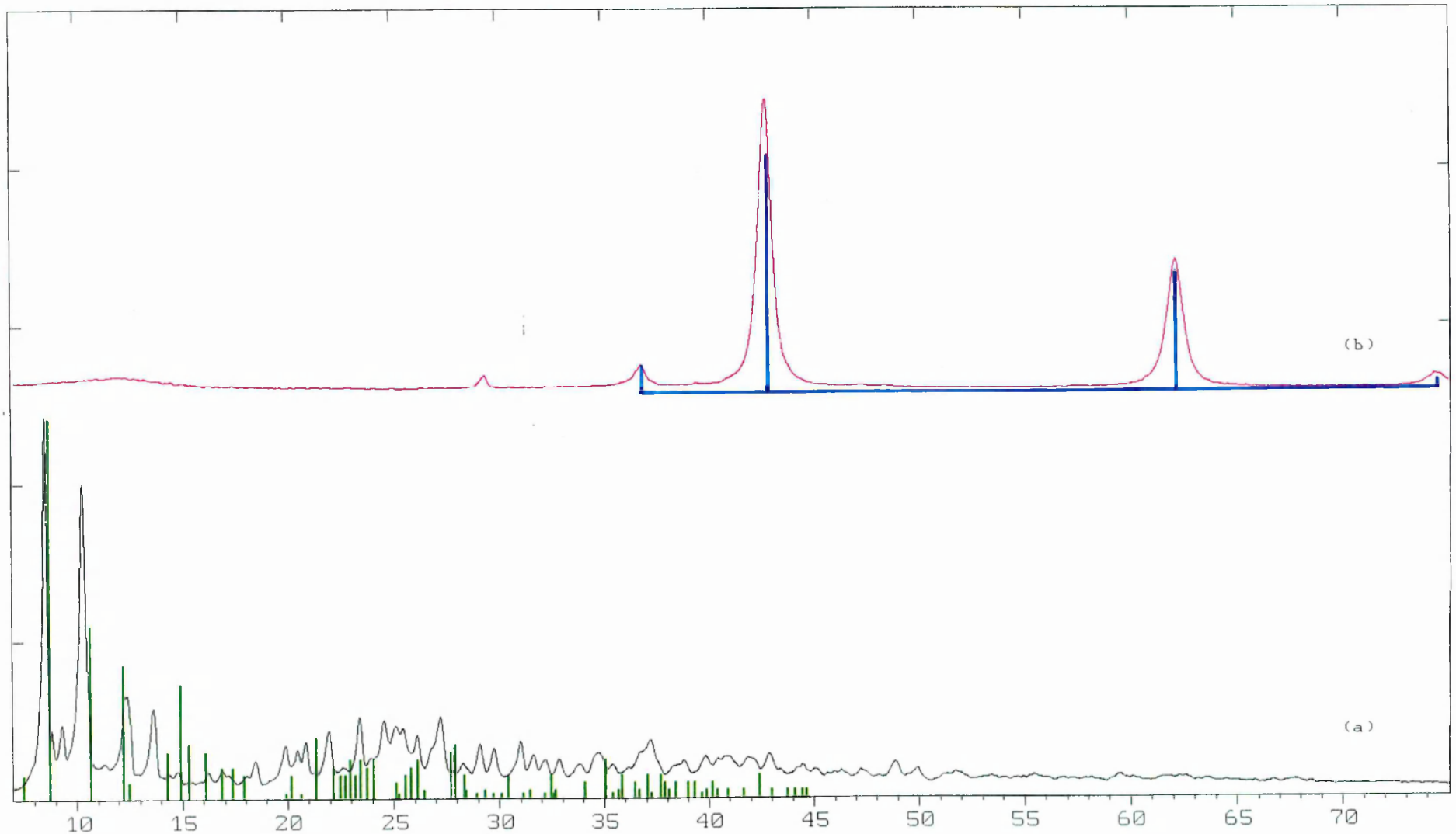

Figure 47. X-ray powder diffraction patterns recorded from hydrothermally processed magnesium acetate (a) dried under an infrared lamp (b) calcined at 500°C. The bar diagrams represent the patterns for: figure (a) magnesium acetate, figure (b) periclase (MgO)

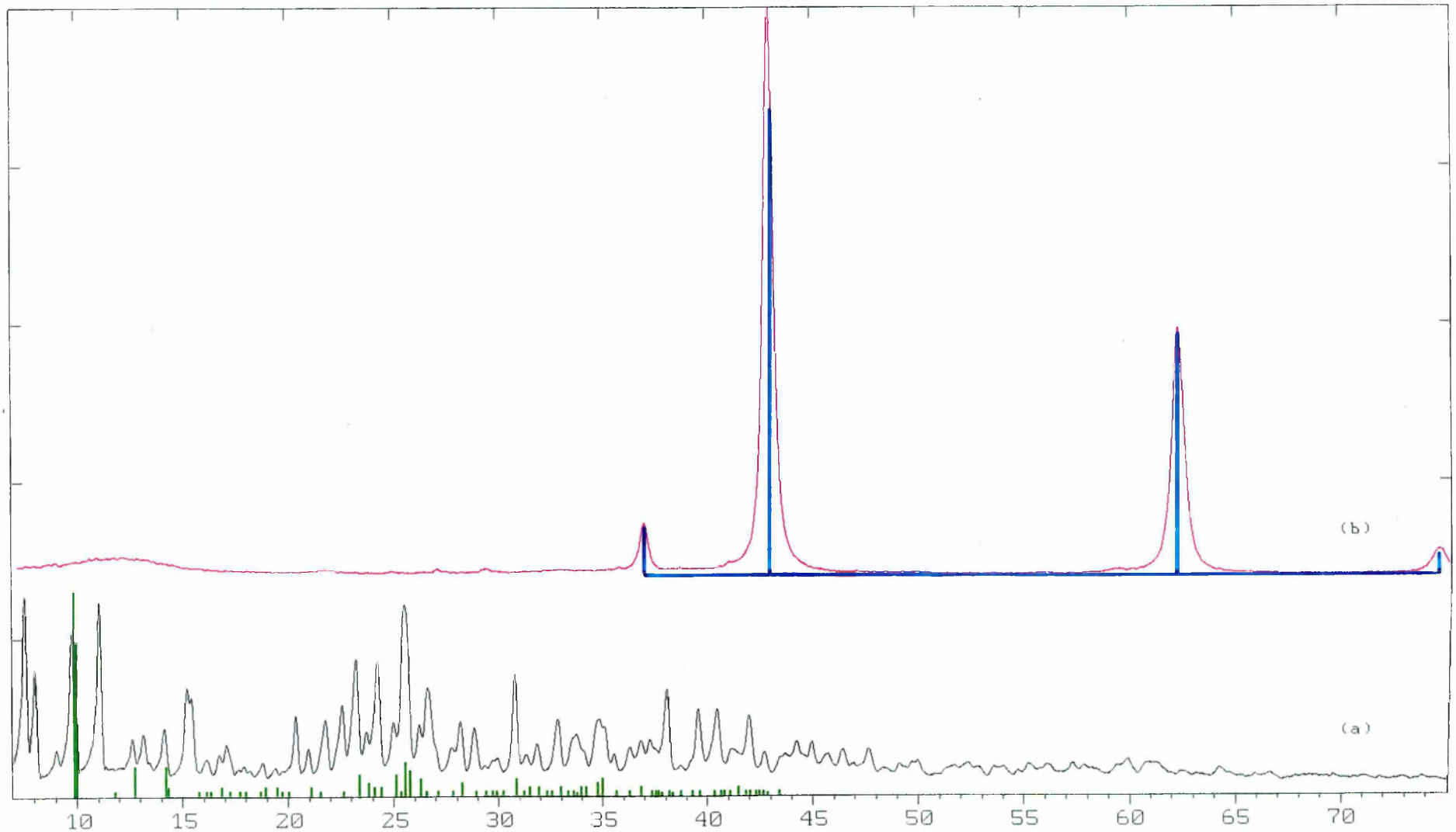

Figure 48. X-ray powder diffraction patterns recorded from hydrothermally processed acidified magnesium acetate (a) dried under an infrared lamp (b) calcined at 500°C. The bar diagrams represent the patterns for: figure (a) magnesium acetate, figure (b) periclase (MgO)

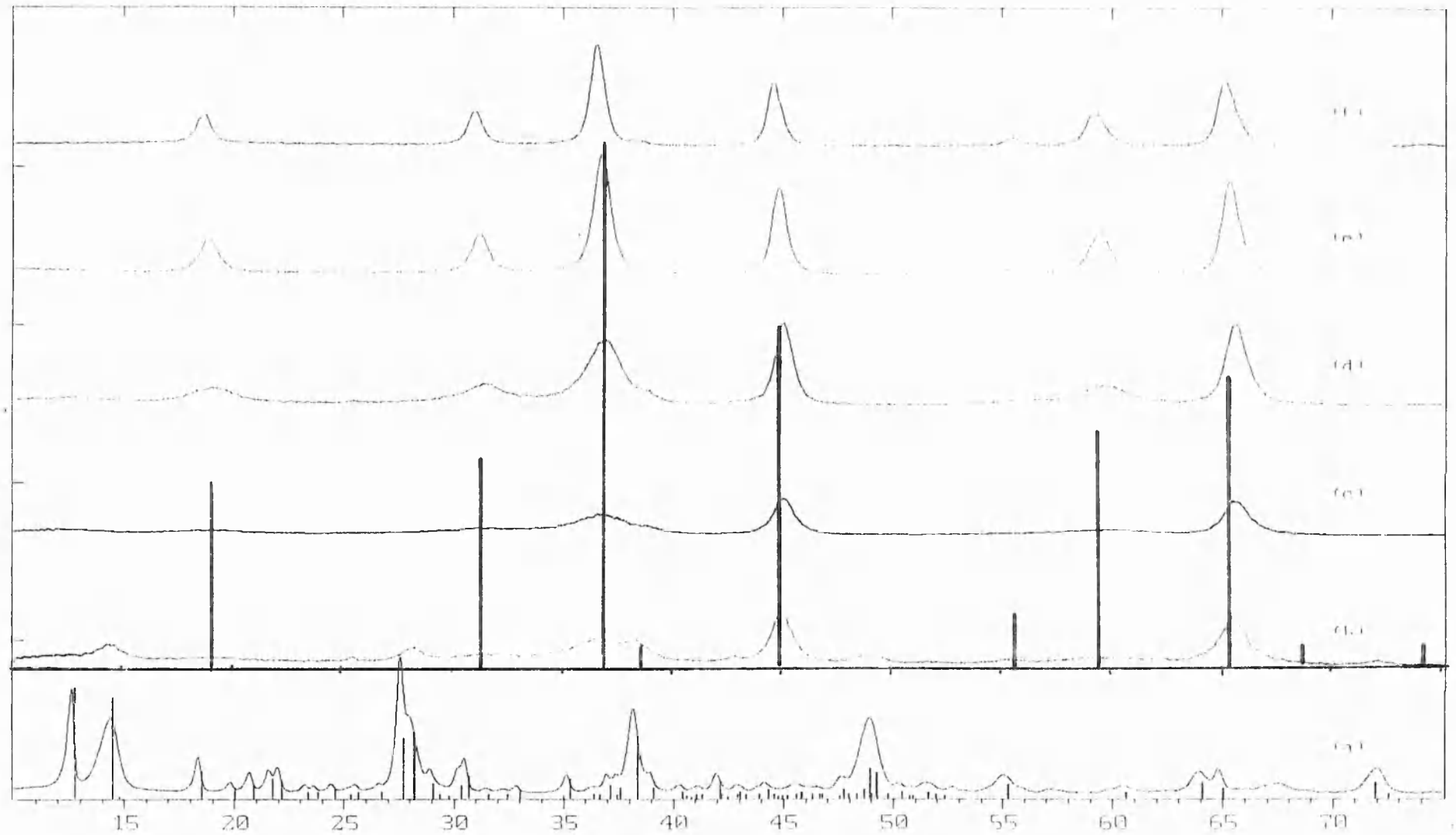

Figure 49. X-ray powder diffraction patterns recorded from hydrothermally co-processed aluminium- and magnesium- acetates (a) dried under an infrared lamp (b) calcined at 400°C (c) calcined at 500°C (d) calcined at 800°C (e) calcined at 1000°C (f) calcined at 1100°C. The bar diagrams represent the patterns for: figure (a) boehmite and magnesium acetate, figure (b) $\gamma - Al_2O_3$, $\alpha - Al_2O_3$ and spinel

The x-ray powder diffraction pattern recorded from the sample dried under an infrared lamp (Figure 49(a)) showed phases attributable to pseudoboehmite and magnesium acetate as well as other peaks of a complex nature which were different from those observed in the x-ray powder diffraction patterns recorded from samples of hydrothermally processed magnesium acetate. The regularity and nature of the peaks would indicate that they are likely to be attributable to magnesium-containing phases.

Comparing the sample prepared from hydrothermally co-processed aluminium- and silicon-acetates dried under an infrared lamp with that prepared from hydrothermally co-processed aluminium- and magnesium- acetates dried under an infrared lamp, it is apparent that the amorphous nature of the silicon-containing phase had a more profound effect on the signal/noise ratio of all the peaks present in the pattern. The magnesium acetate, which appears to be more crystalline, produces a very complex set of peaks but has a relatively flat baseline and does not affect peaks which are not attributable to magnesium-containing phases.

The x-ray powder diffraction pattern recorded from the sample calcined at 400°C (Figure 49(b)) showed the material to be multi-phasic, and to contain pseudoboehmite, spinel, $\alpha - Al_2O_3$ and periclase. The formation of spinel at 400°C is at a significantly lower temperature than obtainable by the sol-gel route.[38] The absence of peaks attributable to $\gamma - Al_2O_3$ and the presence of peaks attributable to corundum, would suggest that the magnesium appears to increase the rate at which $\gamma - Al_2O_3$ converts to $\alpha - Al_2O_3$ relative to the rate observed for this transformation during the formation of mullite (Chapter 4 Section 4.3). It is surprising that there is no evidence of any other magnesium-containing phase, as the formation of spinel is incomplete and there are two other aluminium-containing phases present. The baseline of the pattern shows more fluctuation than observed in the x-ray powder diffraction pattern recorded from the dried sample and it is possible that the excess magnesium forms an amorphous phase.

The x-ray powder diffraction pattern recorded form the sample calcined at 500°C showed a spinel phase, which has broad peaks indicative of a poorly crystalline material, along with a very small quantity of corundum. This indicates that spinel conversion is more advanced than in the sample calcined at 400°C. The x-ray powder diffraction pattern recorded from

the sample calcined at 800°C showed peaks characteristic of spinel. These peaks are narrower and the baseline is flatter, indicating that the spinel phase is more crystalline than that observed in the pattern recorded from the sample calcined at 500°C. There are also peaks characteristic of corundum which are more pronounced than those observed in the pattern recorded from the sample calcined at 500°C. This is likely to be due to the flatter baseline rather than an increase in the intensity of the corundum phase present. The presence of the corundum however would suggest that the spinel-forming reaction has still not reached completion. The x-ray powder diffraction patterns recorded from the samples calcined at 1000°C and 1100°C showed only the spinel phase.

The x-ray powder diffraction patterns recorded from the samples prepared from hydrothermally co-processed acidified aluminium- and magnesium- acetates showed the same phases as hydrothermally co-processed aluminium- and magnesium- acetates at all temperatures (Figures 50(a)-(f)) except that periclase was present at all calcination temperatures up to but not including 1100°C.

6.4.2. Lattice parameters

The lattice parameters (calculated from the 10 most intense peaks) for the pseudoboehmite phase observed in the x-ray powder diffraction pattern recorded from hydrothermally co-processed aluminium- and magnesium- acetates dried under an infrared lamp (Figure 37(a)) are shown in Table 23. The lattice parameters were recorded using the method described in Section 3.5.2 (p.57).

The lattice parameters for pseudoboehmite from hydrothermally co-processed aluminium- and magnesium- acetates are significantly smaller than those recorded from the material formed from hydrothermally co-processed aluminium- and silicon- acetates, indicating that peak shifts larger than those previously observed have occurred. This difference in lattice parameters clearly shows that hydrothermally co-processing aluminium- and magnesium acetates has not produced a simple mixture. Comparing the hydrothermal formation of spinel and mullite it is noticeable through the lattice parameters that the pseudoboehmite phase is experiencing stronger interfacial interactions during the formation of spinel, which is the phase which forms at a lower calcination temperature.

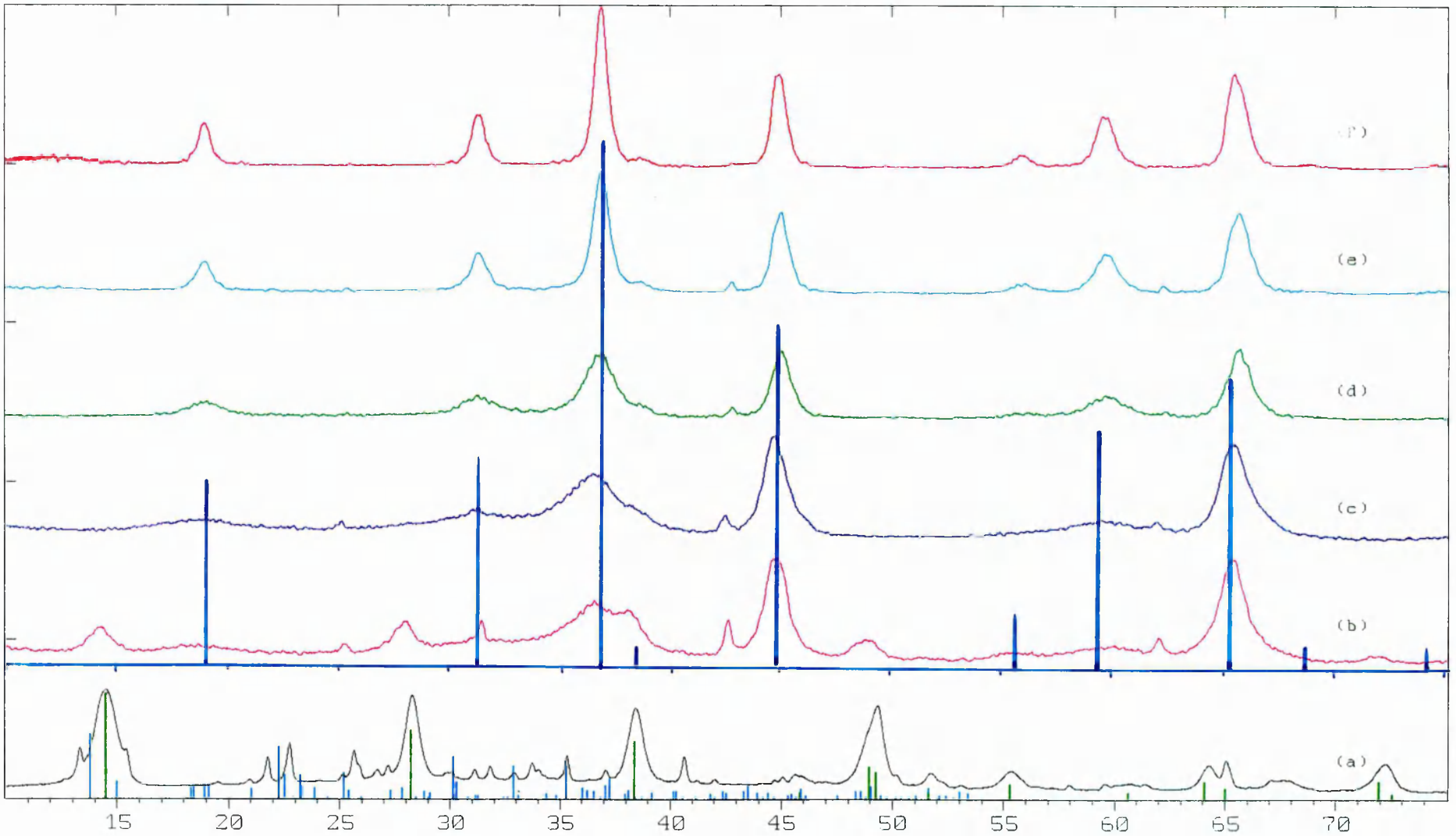

Figure 50. X-ray powder diffraction patterns recorded from hydrothermally co-processed acidified aluminium- and magnesium- acetates (a) dried under an infrared lamp (b) calcined at 400°C (c) calcined at 500°C (d) calcined at 800°C (e) calcined at 1000°C (f) calcined at 1100°C. The bar diagrams represent the patterns for: figure (a) boehmite and magnesium acetate, figure (b) $\gamma - Al_2O_3$, $\alpha - Al_2O_3$ and spinel

This result suggests that the lower the lattice parameters of the pseudoboehmite phase in aluminium-containing systems, the lower the calcination temperature required to form the final product. Other systems which could be used to test this hypothesis could include materials having the inverse spinel or perovskite structures.

Sample History	Lattice Parameters /Å		
	a±0.005	b±0.02	c±0.005
Pseudoboehmite prepared by drying hydrothermally co-processed aluminium- and magnesium- acetates	3.642	12.031	2.828
Pseudoboehmite prepared by drying hydrothermally co-processed aluminium- and silicon- acetates	3.679	12.132	2.852
Pseudoboehmite prepared by drying hydrothermally processed aluminium acetate	3.680	12.176	2.680
Literature values for boehmite [63]	3.700	12.227	2.868

Table 23. Lattice parameters for pseudoboehmite prepared by drying hydrothermally co-processed non-acidified aluminium- and magnesium-acetates under an infrared lamp

6.5 CONCLUSIONS

The lattice parameters for the pseudoboehmite present in the material formed in an autoclave and dried under an infrared lamp were smaller than those for hydrothermally processed aluminium acetate dried under an infrared lamp (Table 1) and smaller still than those observed for the hydrothermal co-processing of aluminium- and silicon- acetates dried under an infrared lamp or the hydrothermal co-processing of aluminium-, silicon- and iron(II) acetates dried under an infrared lamp. This would imply that the interfacial interaction is stronger in the Mg-Al-O system.

The formation temperature of spinel prepared by hydrothermal synthesis is 400°C which is much lower than that for mullite preparation. It is suggested that the low pseudoboehmite lattice parameters are linked to the low preparation temperature of spinel.

Hence the evidence for interactions between precursors, observed in the formation of mullite is endorsed by examination of other systems and indicates that hydrothermal synthesis might be a superior method of commercially important materials.

Appendix A

The theory discussed in Section 2.3 needed to be used on materials which possessed orthorhombic systems such as pseudoboehmite and mullite and so the theory was computerised using a spreadsheet package. This allowed the calculation of lattice parameters from observed peak positions quickly and accurately. Also as this method showed the effect of changing any one peak, experimentation on the best way to accurately determine the position of peaks could be performed. Hence, the cumbersome nature of the Equations was removed. This method was used for both hexagonal systems and orthorhombic systems (Figures 5 and 6).

For each diffraction pattern examined ten peaks were chosen on the basis of high resolution, strong intensity and large value of 2θ. In cases where the sample was highly crystalline i.e. mullite or corundum, there were many peaks to choose from. The importance of having a high value of 2θ was tested because generally the resolution of the ten strongest peaks was superior to the resolution of the high angle peaks. So, ten high angle peaks and ten of the strongest peaks were used for each system. The same ten peaks were used for each material. This enables trends within a system to be accurately observed, such as the changes in lattice parameters with calcination temperature for mullite.

Enter data here

h	k	l	d	2θ	Sin squared theta	α	γ	δ
3	0	6	1.2276	77.73	0.393736826	9	36	9.5
0	2	10	1.1632	82.94	0.438541814	4	100	9.8
2	2	6	1.1035	88.54	0.487276111	12	36	10
2	1	10	1.0557	93.72	0.532400865	7	100	10
4	0	4	1.0393	95.66	0.549335849	16	16	9.9
3	1	8	0.9892	102.29	0.606389371	13	64	9.5
3	2	4	0.9606	106.62	0.643035028	19	16	9.2
0	1	14	0.9581	107.03	0.646395189	1	196	9.1
4	1	0	0.9516	108.09	0.655255883	21	0	9
1	3	10	0.9081	116.04	0.719535862	13	100	8.1
					Totals:	115	664	94
					Sum of the Squares:	1687	75616	891

Σα2 = 1687
Σαγ = 4744
Σαδ = 1075.8
Σγ2 = 75616
Σγδ = 6199.8
Σδ2 = 891.11
Σα sin2 θ= 67.523
Σγ sin2 θ= 385.34
Σδ sin2 θ= 53.022

Normal Equations

1687 A+ 4744 C+ 1075.8 D= 67.523
4744 A+ 75616 C+ 6199.8 D= 385.34
1076 A+ 6199.8 C+ 891.11 D= 53.022

Solutions

A= 0.03121 C= 0.00314

Lattice Parameters

a= 5.035 c= 13.747

Reference Values

Haematite	a=5.05Å, c=13.75Å
Corundum	a=4.76Å, c=12.99Å

Solution of Simultaneous Equations

Eliminate C
Using Equations 1 & 2

823.191 A+ 13121.0 C+ 1075.8 D= 66.8660
1687 A+ 4744 C+ 1075.8 D= 67.5227 -
-863.80 A+ 8377.09 C+ 0 D= -0.6567 4

Using Equations 1 & 3

1298.76 A+ 7484.67 C+ 1075.8 D= 64.0110
1687 A+ 4744 C+ 1075.8 D= 67.5227 -
-388.23 A+ 2740.67 C+ 0 D= -3.5117 5

Eliminate A
Using Equations 4 & 5

-388.23 A+ 3765.08 C+ 0 D= -0.2951
-388.23 A+ 2740.67 C+ 0 D= -3.5117
0 A+ 1024.40 C+ 0 D= 3.21655

Figure 51 The lattice parameter determination of a hexagonal system, using standard values for corundum.

Enter data here

h	k	l	d	2θ	Sin squared theta	α	γ	δ	η
3	7	0	1.007	99.872	0.585722945	9	49	0	9.70606
2	5	2	1.013	98.962	0.577888045	4	25	4	9.75734
1	7	1	1.017	98.449	0.573465232	1	49	1	9.78411
4	2	2	1.098	89.092	0.492080338	16	4	4	9.99749
2	4	2	1.103	88.572	0.487541163	4	16	4	9.99379
2	6	1	1.119	87.004	0.473870445	4	36	1	9.97269
5	3	1	1.186	81.048	0.422198493	25	9	1	9.75788
2	3	2	1.192	80.483	0.417326402	4	9	4	9.7266
4	4	1	1.22	78.314	0.398723041	16	16	1	9.58972
1	3	2	1.24	76.838	0.386150553	1	9	4	9.48153
					Totals:	84	222	24	97.7672
					Sum of the Squares	1284	7494	84	956.108

Σα2 = 1284
Σαγ = 1388
Σαδ = 162
Σαη = 821.764
Σγ2 = 7494
Σγδ = 362
Σγη = 2171.99
Σδ2 = 84
Σδη = 234.931
Ση2 = 956.108
Σα sin2 θ= 38.8654
Σγ sin2 θ= 115.486
Σδ sin2 θ= 11.3122
Ση sin2 θ= 47.1161

Normal Equations

1284	A+	1388	B+	162	C+	821.764	D= 38.865
1388	A+	7494	B+	362	C+	2171.99	D= 115.49
162	A+	362	B+	84	C+	234.931	D= 11.312
821.8	A+	2172	B+	234.93	C+	956.108	D= 47.116

Solutions

A= 0.0104 B= 0.01004 C= 0.0714

Lattice Parameters

a= 7.542 b= 7.688 c= 2.883

Reference Values

Mullite a= 7.5456Å b= 7.6898Å c= 2.8842Å
Haematite a= 5.05Å c= 13.75Å

Solution of Simultaneous Equations

Eliminate D

Using Equations 1 & 2

525.144732	A+	2835.3275	B+	136.9614	C+	821.8	D=	43.69385	
1284	A+	1388	B+	162	C+	821.8	D=	38.86544	-
-758.85526	A+	1447.3275	B+	-25.0386	C+	0	D=	4.828409	5

Using Equations 1 & 3

566.658124	A+	1266.2361	B+	293.8227	C+	821.8	D=	39.56884	
1284	A+	1388	B+	162	C+	821.8	D=	38.86544	-
-717.341876	A+	-121.7639	B+	131.8227	C+	0	D=	0.703396	6

Using Equations 1 & 4

706.297502	A+	1866.8014	B+	201.921	C+	821.8	D=	40.49582	
1284	A+	1388	B+	162	C+	821.8	D=	38.86544	-
-577.702498	A+	478.80142	B+	39.92104	C+	0	D=	1.630381	7

Eliminate A

Using Equations 5&6

-758.855	A+	-128.811	B+	139.4515	C+	0	D=	0.7441	
-758.855	A+	1447.328	B+	-25.0386	C+	0	D=	4.8284	-
0	A+	1576.138	B+	-164.49	C+	0	D=	4.0843	8

Using Equations 5&7

-758.855	A+	628.9413	B+	52.43925	C+	0	D=	2.1416	
-758.855	A+	1447.328	B+	-25.0386	C+	0	D=	4.8284	-
0	A+	818.3862	B+	-77.4779	C+	0	D=	2.6868	9

Eliminate B Using Equations 8 & 9

1576.138	B+	-149.215	C=	5.174501
1576.138	B+	-164.49	C=	4.084307
0	B+	15.27468	C=	1.090193

Figure 52 The lattice parameter determination of an orthorhombic system, using standard values for mullite.